LBL-2200
c.1

COMPUTER SIMULATION OF FRANK LOOP CONTRAST IN FIELD ION IMAGES

RECEIVED
LAWRENCE
RADIATION LABORATORY
NOV 21 1973
LIBRARY AND
DOCUMENTS SECTION

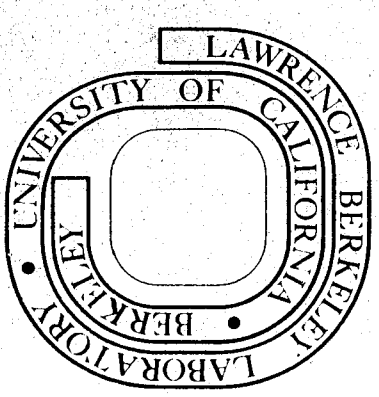
Kaj Gunnar Stolt
(Ph. D. Thesis)

September 1973

Prepared for the U. S. Atomic Energy Commission
under Contract W-7405-ENG-48

For Reference

Not to be taken from this room



LBL-2200
c.1

COMPUTER SIMULATION OF FRANK LOOP CONTRAST IN FIELD ION IMAGES

Table of Contents

ABSTRACT v

I. INTRODUCTION 1

II. REVIEW OF THEORY AND EXPERIMENTAL OBSERVATIONS 3

A. Geometrical Image Theory 3

B. Dislocation Contrast 4

1. Perfect Dislocations 4

2. Stacking Faults and Partial Dislocations 8

3. Instrinsic and Extrinsic Faults 12

C. Computer Simulation of Field Ion Images 18

1. General Description of Model 18

2. Simulation of Dislocation Contrast 22

D. Experimental Observations 29

E. Summary 32

III. SIMULATION OF FRANK LOOP CONTRAST 34

A. Model for Computation 34

1. Displacement Field of Dislocation Loops 34

2. Geometry of Frank Loops 35

3. Lattice Model 36

4. Surface Relaxation 37

5. Field Evaporation 41

B. Results 43

1. Check of Model 43

2. Effect of Mirror Loop 47

3. Contrast from Loops Wholly Beneath the Surface 51

4. Difference in Contrast Between Vacancy and Interstitial Loops 56

5. Size of Loops 58

IV. COMPARISON WITH EXPERIMENTAL OBSERVATIONS 62

A. Experimental Facilities and Methods 62

B. Examples of Possible Frank Loop Contrast 64

V. DISCUSSION 67

VI. SUMMARY AND CONCLUSIONS 74

ACKNOWLEDGMENTS 76

REFERENCES 77

FIGURE CAPTIONS 79

FIGURES 85

COMPUTER SIMULATION OF FRANK LOOP CONTRAST IN FIELD ION IMAGES

Kaj Gunnar Stolt

Inorganic Materials Research Division, Lawrence Berkeley Laboratory and Department of Materials Science and Engineering, College of Engineering; University of California, Berkeley, California

ABSTRACT

A computer model for simulation of the image contrast caused by Frank dislocation loops in field ion tips of fcc materials is presented. The model is based on the shell model for ion image simulation, whereas the displacement field of Frank loops is computed from the exact displacement equation for a closed dislocation loop in an isotropically elastic continuum. A method for taking surface effects into account by superposition of the displacement field of an image loop is introduced. The results indicate that Frank loops will cause image contrast while wholly beneath the surface of the tip, and that vacancy and interstitial loops will cause qualitatively different contrast. The effect of surface relaxation, while quantitatively substantial, does not qualitatively alter these results. Special emphasis is placed on small loops, with respect to which existing contrast theory is inadequate. Some micrographs of ion bombarded iridium tips are presented. These micrographs display contrast effects in excellent agreement with computer plots of interstitial loop contrast.

I. INTRODUCTION

This investigation was motivated by certain contrast effects discovered in ion micrographs of ion bombarded iridium tips. While some of these effects could clearly be attributed to dislocation loops, others could not be explained on the basis of existing image theory. Since both kinds of effects were observed in the same tips, the thought naturally arose that both were due to dislocation loops. There was further some reason to believe that small loops were responsible for the unexplainable effects. Review of the literature revealed that little had been published about dislocation loop contrast and nothing specifically about small loops. The decision to concentrate on Frank loops was based largely on the fact that electron microscopists have been struggling for years trying to specify the nature of Frank loops observed in radiation damaged metal specimens. It was felt that ion microscopy might have a contribution to make in this field, especially with respect to small loops (say < 30 Å in diameter).

The original intention was to analyze the observed contrast effects by computer simulation. During the course of this investigation some general features of Frank loop contrast became evident and the emphasis of the study shifted to exploring Frank loop contrast in general by computer simulation with specific emphasis on small loops.

A rather thorough review of theoretical and experimental work in the field is presented in Part II of this thesis as a background to the results obtained here. The review concerns itself both with image formation from faulted crystals, and with computer simulation of ion

images in general. In Part III the computer model that was developed for simulation of Frank loop contrast is discussed in detail, whereafter the main findings of this study are presented. Some of the experimental observations that initiated this study are presented in Part IV, and in Part V some aspects of the obtained results are generally discussed.

II. REVIEW OF THEORY AND EXPERIMENTAL OBSERVATIONS

A. Geometrical Image Theory

Although the imaging process in the field ion microscope involv rather complex electronic phenomena, a field ion image can be simulated with remarkable success on purely geometrical grounds. This was first demonstrated by Moore[1] in a computer simulation of images of perfect crystals based on two simple ideas. The first is that the surface of a field ion tip may be considered atomically smooth and approximately spherical, and the second, following an observation by Müller,[2] that imaging atoms are those which protrude most from the surface. Moore realized that the protrusion of atoms, situated on a lattice, from a spherical surface is difficult to visualize, and gave the following definition: if an infinite crystal is cut by a spherical surface the atoms inside the sphere may be said to constitute a spherical crystal, the surface of which may be termed an atomically smooth spherical surface. The radial distance of each atom of the crystal from this surface can be easily calculated and used as a measure of protrusion. The atoms closest to the surface protrude most, and hence contribute to the field ion image of the surface. The smooth surface of field ion tips comes about because field evaporation removes atoms protruding too much above an approximately spherical surface.

The image of the region surrounding a pole of a field ion tip can be understood if the region is thought to conform to a smoothly curved surface as illustrated in Fig. 1a. The diameter of the consecutive crystal planes building up this region is limited by the surface.

If only atoms at the plane edges are considered to protrude enough to image, the projected image of this region is clearly a series of concentric rings, as shown in Fig. 1b. Images of faulted crystals are analyzed by first considering the possible surface displacements caused by the fault, and thereafter imposing a smooth envelope on the faulted surface as above. Figure 1c shows the possible effect of a planar fault on a crystal, and Fig. 1d the resulting image. It should be clearly recognized that only displacements normal to the surface are significant in this model. Displacements in the surface cause only secondary effects.

The foregoing is the essence of the geometrical image theory. It is the basis both of the intuitive approach to the analysis of image contrast, and of computer simulation. In the following these two methods of image interpretation will be discussed in some detail, starting with the intuitive approach.

B. Dislocation Contrast

1. Perfect Dislocations

Dislocation contrast is derived from the fact, first pointed out by Cottrell,[3] that a perfect dislocation line intersecting a stack of lattice planes will convert this stack into a helical ramp (Fig. 2b). This property is generally recognized for a screw dislocation, but it is true for any dislocation as long as the Burgers vector of the dislocation has a component along the normal to the planes. The pitch of the helical ramp, i.e. the separation of consecutive planes in the ramp, is, by definition of a perfect

dislocation, an integral number of plane spacings. If this integer is greater than one, the stack of planes is actually converted into several interleaved ramps, each of the same pitch. The effect of a dislocation line emerging from a plane of a field ion tip is illustrated in Fig. 2.[4] Figure 2a is a sketch of the planes belonging to a pole when perfect. In Fig. 2b a dislocation line has converted the stack of planes into a helical ramp, and in Fig. 2c the effect of field evaporation on the ramp is indicated. The latter is realized by imposing a smooth surface upon the ramp. The projected image of this configuration is a continuous spiral as shown in Fig. 2d.

The pitch of the helical ramp can be determined analytically as follows [5,6]: the pitch is obviously the magnitude of the projection of the Burgers vector, $\vec{b}$, of the dislocation onto the plane normal. If the unit normal of the plane is $\vec{n}$ the pitch, p, is hence:

$$p = \vec{b} \cdot \vec{n} \quad . \tag{II-1}$$

The normal of any lattice plane (hkℓ) is the corresponding reciprocal lattice vector $\vec{g}_{hk\ell}$, the length of which is the reciprocal of the lattice spacing, i.e.

$$\vec{g}_{hk\ell} = \frac{\vec{n}}{d_{hk\ell}} \quad , \tag{II.2}$$

and consequently,

$$p = (\vec{g}_{hk\ell} \cdot \vec{b})\, d_{hk\ell} \quad . \tag{II.3}$$

The scalar product in Eq. (II.3) must be an integer for perfect dislocations. This is immediately obvious if the indexing of planes and

vectors is referred to the primitive translation vectors of the lattice. In this case the perfect Burgers vector would be a lattice vector by definition. The scalar product of two lattice vectors belonging to mutually reciprocal lattices is always an integer. Since this result is a property of the lattice, it must be true in any system of translation vectors.

The crystallography of the fcc structure is usually based on the conventional cubic unit cell, to take advantage of the symmetry of the structure. The lattice translations are the cell edges a[100], a[010], and a[001], where a is the lattice constant. In this system the Burgers vector of a perfect dislocation, $\frac{a}{2}[110]$, is not a lattice vector. The reciprocal lattice vectors are, in this case, of the form $\frac{1}{a}[hk\ell]$, with h, k and ℓ either all odd or all even. This requirement follows directly from a transformation of axis from the primitive cell to the conventional cubic cell.[7] Hence $\vec{g}_{hk\ell} \cdot \vec{b}$ is of the form $(h + k)/2$, with $h+k$ even, i.e., an integer.

It is convenient to drop $d_{kh\ell}$ from Eq. (II.3) and write

$$p = \vec{g}_{hk\ell} \cdot \vec{b} \quad , \qquad \text{(II.4)}$$

where p is understood to be expressed in units of the plane spacing. The value of p, i.e. an integral number, indicates the multiplicity of the image spiral caused by the dislocation. A case where $p = 3$ is schematically illustrated in Fig. 3.[4] It would correspond to e.g. $\vec{g} = \frac{1}{a}[331]$ and $\vec{b} = \frac{a}{2}[110]$.

If $p = 0$ the Burgers vector is in the plane under study, i.e. the displacements are parallel to the plane and no spiral structure

will develop. On some high index planes the core structure of the dislocation, or the "extra half plane", may be visible in this case.

Analysis of dislocations is usually aimed at finding the Burgers vector. The sign of the Burgers vector depends on the sense of the dislocation line, which is arbitrary. The following convention is usually chosen:[8] The sense of the dislocation line is defined by assigning a unit vector, $\vec{\ell}$, tangent to the line. The positive sense of the line is in the positive direction of $\vec{\ell}$. A clockwise circuit, looking down the positive sense of the line, is formed in a plane intersecting the dislocation. The circuit would close in a perfect reference crystal, but fails to close in the real crystal. The Burgers vector is the vector drawn from the starting point to the finishing point of this unclosed circuit. In field ion micrographs this definition leads to the following rule: if $\vec{\ell}$ is chosen to point out ($\vec{n}\cdot\vec{\ell} > 0$) of the crystal then a clockwise spiral, when looking down on a positive print, indicates that the Burgers vector has a positive component along the plane normal $\vec{n}$, i.e. p is positive. Another property of a dislocation line is that with this definition of $\vec{\ell}$, the vector $\vec{\ell} \times \vec{b}$ points towards the extra half plane connected with the dislocation. By the use of this property intrinsic dislocation loops can be distinguished from extrinsic loops.[9]

Generally the Burgers vector of a perfect dislocation cannot be deduced from a single micrograph. The information obtainable is the magnitude and sign of p from the multiplicity and sense of the image spiral. Usually several Burgers vectors satisfy the value of p. If the dislocation emerges in a region where two sets of image rings are resolvable a unique determination of $\vec{b}$ can probably be made from the

two p values. This is also the case, if during field evaporation the dislocation "moves" from one pole region to another. If the direction of the dislocation line is needed a field evaporation sequence is, of course, necessary.

Perfect dislocation loops and dipole pairs are treated simply by combining the effects of single dislocations. The two dislocations in a dipole pair have equal but opposite Burgers vectors. Hence they will cause spirals of opposite sense when emerging in the same pole, and the spiral started by one will end at the other. Plane rings enclosing both dislocations will be unbroken since the net Burgers vector is zero. Figure 4[10] illustrates two cases with $|p| = 1$. In Fig. 4a the two dislocations emerge on the same plane, in Fig. 4b on different plane ledges. Dislocation loops obviously behave in the same manner. If $p > 1$, a similar system of multiple spirals is expected. In the case of dislocation loops the line of intersection between the loop plane and the surface of the tip can be determined by direct measurement on the micrograph. The points of emergence of the dislocations are taken to be where the spiral starts and ends. From the line of intersection the plane of the loop can ususally be deduced.

2. Stacking Faults and Partial Dislocations

A planar fault in a crystal is characterized by a displacement vector $\vec{R}$, which is defined as the displacement of one side of the crystal relative to the other. Where the fault plane cuts the surface of the crystal a step will result. The height of the step, normal to the surface plane, is the projection of $\vec{R}$ on the plane normal. A parameter q, analogous to p of Eq. (II-4), can be defined for the fault:

$$q = \vec{g}_{hk\ell} \cdot \vec{R} \quad . \qquad \text{(II.5)}$$

The unit of q is again the lattice spacing $d_{hk\ell}$. Since $\vec{R}$ describes a fault it must not be a lattice vector of the primitive lattice and consequently q need not be an integer, although it may be. For stacking faults on the {111} planes in fcc crystals the value of q is always of the form n/3,where n is an integer (zero included).

The image contrast expected when a stacking fault intersects a pole in a field ion tip is a series of broken plane rings. The intuitive approach to this contrast is outlined in Fig. 5a and 5b, for an intrinsic and extrinsic stacking fault respectively.[11] An intrinsic stacking fault in fcc corresponds to the removal of one (111) plane, the extrinsic to the insertion of one extra (111) plane. This will introduce one fault in the regular stacking sequence (ABCA···), in the intrinsic case, and two consecutive faults in the extrinsic case. The broken ring contrast results because the surface of the sheared stack of planes must conform to an approximately hemispherical shape. The case illustrated in Fig. 5 yields $|q| = 4/3$ ($\vec{g} = \frac{1}{a}$ [220], $\vec{R} = \frac{a}{3}$ [111]). The top half-plane will be removed first by field evaporation. Thereafter the smallest ring will alternately appear on either side of the fault as field evaporation progresses. If $|q| > 1$ field evaporation is expected to remove an integral number of planes from one side of the fault. If q is nonintegral the integral residue q' of q is used to characterize the contrast in this case. For instance if q = 5/3,q' would be 2/3.

Partial dislocations bound stacking faults. The Burgers circuit used to define the Burgers vector of a partial dislocation must start and end on the associated stacking fault. Hence the Burgers vector of a partial dislocation will be the same as the displacement vector of the stacking fault, or differ from it by a lattice vector. Equation (II.5) is valid for partial dislocations with $\vec{R}$ replaced by $\vec{b}_p$.

In the fcc structure there are two kinds of partial dislocations, which are called Shockley and Frank partials. They are both associated with intrinsic or extrinsic stacking faults. Shockley partial dislocations are created by glide on the {111} planes. The possible Burgers vectors are of the form $\frac{a}{6}\langle 112\rangle$ of which there are three on each {111} plane. Shockley partials occur either as closed loops or as dissociated perfect dislocations. When a Shockley loop intersects the surface of the crystal, it will appear as two dislocations on either side of a stacking fault. The Burgers vectors of the two dislocations must in this case be equal but opposite, i.e. the net Burgers vector is zero. The appearance of a dissociated dislocation is the same, but the net Burgers vector is now that of the dissociated perfect dislocation. Frank dislocations occur only in loops. The loops are formed by the collection of point defects into disks on the {111} planes. A disk of vacancies, and the ensuing collapsing of the planes above and below the plane of the disk, creates an intrinsic loop. A disk of interstitials between two {111} planes constitutes an extrinsic loop. The dislocation bounding the Frank loop is of pure edge character, and its Burgers vector is of the form $\frac{a}{3}\langle 111\rangle$. When a Frank loop intersects the crystal surface it appears as two dislocations

connected by a stacking fault. The Burgersvectors of the two dislocations are equal but of opposite sign, so that the net Burgers vector is zero.

The image contrast from partial dislocations must clearly be a combination of "dislocation contrast" and "stacking fault contrast". The spiral contrast of a dislocation will develop, but, when q is nonintegral, the spiral will not be continuous but broken, or stepped. Alternatively one may start with the stacking fault contrast of Fig. 5 and imagine that the breaking of the rings stops at the partial. The simplest case, where one partial dislocation emerges in the center of the plane, and $|q| < 1$, is easy to visualize and is illustrated in Fig. 6.[4]

For a partial dislocation the value of q is significant even when $|q| > 1$, and not only the integral residue q'. This is so because several interleaved stepped spirals will develop in this case, as shown in Fig. 7.[4] The multiplicity of the spiral is the smallest integer larger than q.

When both partials of a dislocation loop emerge in the same pole, rings enclosing none or both of the partials will be unbroken. Rings enclosing only one partial will be stepped. This case is illustrated in Fig. 8.[4] A dissociated dislocation causes the same contrast, except that rings enclosing both partials will form a continuous spiral due to the enclosed perfect dislocation. Figure 9 is a sketch of this situation.[4]

When q is zero or integral no surface step is formed at a stacking fault after field evaporation, and the rings crossing the fault will be unstepped. There will, however, be small kinks in the rings where they cross the stacking fault, caused by the projection of $\vec{R}$ in the imaged plane. A measure of the magnitude of the kink is the normal displacement of atomic rows in the plane. If this displacement is zero or an integral number of row spacings, there will be no kink. This is in any case such a small effect that its detection in the image is doubtful. Some contrast effects in observed images have been attributed to kinks, however.[9] For a partial dislocation an integral value of q means that a continuous spiral develops in the image, with kinks where the spiral crosses the stacking fault.

3. Intrinsic and Extrinsic Faults

Distinguishing between intrinsic and extrinsic faults turns out to be a difficult matter. The geometrical image criterion makes it possible to tell by inspection which side of the crystal has been pushed into the tip at a fault. If the fault plane is also known, the nature of the fault can, in some cases, be deduced.

The clearest case turns out to be a Frank loop with both partials emerging in the same pole (Fig. 10a). The image in this case consists of two sets of half-rings divided by the stacking fault. It is always possible to tell on which side of the fault the half-rings are smaller. This is not quite so obvious as it seems since the smallest, i.e. the central, half-ring will alternate between the two sides of the fault as field evaporation removes the top half-plane. There will, however, be an unbroken ring enclosing the whole loop, and one can tell from the

largest broken ring on which side of the fault the half-rings are smaller.[11] Another way of saying this is to note that one can tell which pair of half-rings belong together in the unfaulted crystal. The side with the smaller half-rings has been pushed toward the surface of the tip. If in addition the plane of the loop is known, this fact allows a determination of the nature of the loop. Figure 10b illustrates this for the case of a loop on either of two {111} planes under (001). The image in Fig. 10a could result from either an intrinsic loop on (111) or an extrinsic loop on $(11\bar{1})$. The determination is unambiguous in the case of a Frank loop because it can be created by one displacement alone on any one plane. For example, an intrinsic loop on (111) in Fig. 10b can be created only by displacing the part of the crystal to the right of (111) into the crystal, i.e. in the $[\bar{1}\bar{1}\bar{1}]$ direction.

For Shockley loops the situation is more complicated. On each {111} plane there are three fault vectors leading to the intrinsic fault. On the (111) plane they are $\frac{a}{6}[\bar{2}11]$, $\frac{a}{6}[1\bar{2}1]$ and $\frac{a}{6}[11\bar{2}]$ (Fig. 11b). The opposites of these vectors lead to the extrinsic fault. Although the stacking fault is the same in all three cases, the bounding dislocations are not, and three physically distinct configurations exist. Specifically it is no longer possible to uniquely connect one type of fault with a displacement out of or into the tip. For instance if an intrinsic Shockley loop is created on (111) in Fig. 10b, one of the possible displacements ($\frac{a}{6}[11\bar{2}]$) will push the right side into the crystal whereas the other two will push it out.

Fortes[12] has analyzed this case within the framework of the geometrical image theory as follows: the fault plane is assigned a

unit normal $\vec{N}$. The side of the crystal to which $\vec{N}$ points is called +N, the other -N. The fault vector $\vec{R}$ is defined as that displacement of +N relative to -N which will create the fault in question. As noted above there are three possible vectors $\vec{R}$ for a particular fault. If vectors $+\vec{R}$ create intrinsic faults, vectors $-\vec{R}$ create extrinsic faults. The Burgers vector of the bounding dislocation is defined by a Burgers circuit that starts on the -N side of the fault. The Burgers vector is the closure failure of the circuit pointing towards the end of the circuit. This definition will make $\vec{b}_p$ coincide with $\vec{R}$. It is only necessary to determine the Burgers vector for one dislocation, specifically the one closer to the pole. This is called the leading partial.

The determination of the nature of the loop is based on the possibility to tell, by inspection of the image, the relative displacement of the +N and -N sides of the fault. If the Burgers vector of the leading partial dislocation is known unambiguously it is then possible to infer the nature of the loop. The Burgers vector is determined from the value of $|q|$, i.e. the spiral structure of the image. Knowledge of the fault plane restricts the number of possible Burgers vectors to three. If only one of these yields the observed value of $|q|$ an unambiguous determination of the nature of the fault can be made. The procedure and the problems involved are best illustrated with an example. Consider a fault on (111) under (001) (Fig. 11). The possible fault vectors are indicated below, together with their $|q|$-values:

	b_1	b_2	b_3
Burgers vector:	$\pm \frac{a}{6}[\bar{2}11]$	$\pm \frac{a}{6}[1\bar{2}1]$	$\pm \frac{a}{6}[11\bar{2}]$
$\|q\|$	1/3	1/3	2/3

The normal of the fault plane can be chosen as [111] . Hence the positive directions of $\vec{b}_1$, $\vec{b}_2$ and $\vec{b}_3$ are connected with an intrinsic fault, and their negative directions with an extrinsic fault. If the image indicates that the +N side has been displaced toward the outside of the tip, the possible fault vectors would be $+\vec{b}_1$, $+\vec{b}_2$ and $-\vec{b}_3$. The former two would yield an intrinsic fault, the latter an extrinsic fault. The $|q|$ value would be different for $\vec{b}_1$ and $\vec{b}_2$ on the one hand (1/3), and $\vec{b}_3$ on the other (2/3). In principle this difference would be visible in the image, but in practice it may be too small for unambiguous determination (see below). If this distinction between the possible Burgers vectors cannot be made with certainty, the nature of the loop cannot be inferred. This case, unfortunately, is the rule rather than the exception. Table I[12] is a list of $|q|$-values for some prominent poles in fcc crystals. The table is compiled for faults on the (111) plane. It indicates, for each possible Burgers vector, which side of the crystal will be displaced towards the surface of the tip for each kind of fault (intrinsic or extrinsic). The table shows that it is frequently necessary to distinguish between $|q| = 1/3$ and $|q| = 2/3$ in order to determine the nature of a loop. If for one case $|q| > 1$ and for the other $|q| < 1$ the distinction can be made, as is the case for the $(\bar{1}\bar{1}3)$ and $(1\bar{3}1)$ poles. If $q = 0$ this method is not applicable. It should also be pointed out that a distinction between Frank and Schockley loops is not possible based on this theiry alone. Usually, however, only one of these is expected, depending on the history of the tip.

Table I. Characterization of (111) faults in fcc metals *

Burgers vector of leading partial dislocation	$\pm \frac{a}{3}[111]$			$\pm \frac{a}{6}[\bar{2}11]$			$\pm \frac{a}{6}[1\bar{2}1]$			$\pm \frac{a}{6}[11\bar{2}]$		
Side of (111) plane displaced to the outside of the tip	+N		-N	+N		-N	+N		-N	+N		-N
Ring configuration	$\|q\|$			$\|q\|$			$\|q\|$			$\|q\|$		
Pole of emergence												
001	E	2/3	I	I	1/3	E	I	1/3	E	E	2/3	I
010	E	2/3	I	I	1/3	E	E	2/3	I	I	1/3	E
100	E	2/3	I	E	2/3	I	I	1/3	E	I	1/3	E
111	E	1/3	I	E	1/3	I	E	1/3	I	I	2/3	E
$1\bar{1}1$	E	1/3	I	E	1/3	I	I	2/3	E	E	1/3	I
110	E	4/3	I	E	1/3	I	E	1/3	I	I	2/3	E
$1\bar{1}0$	-	0	-	E	1	I	I	1	E	-	0	-
113	E	5/3	I	I	1/3	E	I	1/3	E	E	2/3	I
$\bar{1}13$	E	1	I	I	1	E	-	0	-	E	1	I
$1\bar{1}3$	E	1/3	I	I	2/3	E	I	2/3	E	E	4/3	I
$1\bar{3}1$	I	1/3	E	E	2/3	I	I	4/3	E	E	2/3	I
$0\bar{1}2$	E	2/3	I	I	1/3	E	I	4/3	E	E	5/3	I
$0\bar{2}1$	I	2/3	E	E	1.3	I	I	5/3	E	E	4/3	I

I: intrinsic fault; E: extrinsic fault; N: parallel to [111]

*Reference 12.

If the stacking fault runs all through the tip the method described above is not useful, since there are no bounding partial dislocation visible in the image. The following considerations can be applied to determine the nature of the stacking fault[12]: The step height at the fault in the (hkℓ) region is determined by a parameter q" obtained by adding an integer to q such that $0 < q'' < 1$. The step height is either $q''d_{hk\ell}$ or $(1-q'')d_{hk\ell}$ depending on which side of the fault is higher. During field evaporation these two values alternate. Considering again a fault on (111) intersecting (001), the cases sketched in Fig. 12 are possible.[12] For an intrinsic fault $q'' = 1/3$ (e.g. $\vec{R} = \frac{a}{3}[\bar{1}\bar{1}\bar{1}]$), which means that each (001) plane on the positive side of (111) is $\frac{1}{3}\, d_{002}$ above the next plane below, on the other side of the fault. For an extrinsic fault the corresponding value is $\frac{2}{3}\, d_{002}$. These differences in step height will affect the size of the half rings. Figures 12a and b show two stages of field evaporation through an intrinsic stacking fault on (111). In each case the size of the top plane, or smallest ring, is the same. As can be readily seen in the sketch, the size of the second half-ring is larger when this ring is on the positive side of (111). For the extrinsic fault in Fig. 12c and d the situation is reversed. Hence this effect can be used to determine the nature of the fault provided the effect is large enough to be measured. An estimation of the size of the effect can be made by considering the surface to be hemispherical. It turns out that the size of the second half-ring should change by about 10% when the half-ring moves from one side of the fault to the other. This is probably large enough to be observed

under favorable circumstances. It is highly probable, however, that image distortions will obscure this fine detail.

C. Computer Simulation of Field Ion Images

1. General Description of Model

A computer model for the simulation of field ion images can be constructed on purely geometrical grounds. A three-dimensional point lattice is defined with respect to some coordinate system. This lattice is intersected by two concentric hemispherical surfaces so that a thin hemispherical shell is enclosed. A computer is instructed to find those lattice points which lie within the shell, and to plot their coordinates in orthographic projection. The resulting patterns bear a striking resemblance to field ion images. An example of one such pattern from a fcc crystal is shown in Fig. 13.

This model is clearly a direct application of the geometrical image theory. It is known as the shell model for obvious reasons.

Sanwald and Hren[13] have constructed a different computer model, in which the coordination number of the atoms is used as imaging criterion. This model has yielded spot by spot correspondence with a micrograph of a platinum tip, over a limited region around (931). The model is difficult to apply, and has not been used for faulted crystals.

Perry and Brandon[14] have calculated the bond number of imaged atoms as defined by the shell model for the bcc crystal. The majority of imaged atoms are of type 4.3, which indicates four nearest and three second nearest neighbors (kink site). The rest are mainly edge site atoms (5.3 or 4.4), and only a small fraction have higher coordination than 5.3.

The critical parameter in the shell model is the shell thickness, P, which represents the maximum distance below the surface at which atoms will contribute to the image. P is selected empirically by comparing the density of image spots in a simulated and a real image. Typically P is of the order of one tenth of the lattice constant. The value of P decreases with increasing radius of the tip. This is to be expected intuitively, since a smaller radius of curvature will increase the number of steps on the surface, thus allowing atoms farther below the surface to contribute to the image. Moore and Brandon[15] have investigated the variation of shell thickness with tip radius in terms of the bond number of imaged atoms. This variation comes about because the thickness of shell containing atoms of a critical bond number depends on the radius. Table II[16] lists the shell thickness for various tip radii. The radius is measured in lattice constants (a) and the shell thickness in interatomic distances $(a/\sqrt{2})$ for fcc, and lattice constants for bcc.

The shell model is successful in the sense that it correctly reproduces both the number of discernible planes along any one zone, and the relative prominence of the planes.[16] The most spectacular difference between computed and real images is the inability of a purely geometrical model to reproduce the variations in brightness over the image. There is also a considerable difference in the distance between poles. Some improvement in the latter respect could probably be brought about by choosing a different projection. Brandon[17] has shown by direct measurement on micrographs of tungsten tips that a projection of the same family as the sterographic with

Table II. Shell thickness (P) for different sphere radius *

R/a	P
20	0.219
40	0.139
60	0.1007
80	0.0819
100	0.0736
150	0.060
200	0.0533
250	0.0464

*Reference 16

the projection point moved one radius outside the projection sphere, corresponds closely to the actual field ion projection. The problem is, however, that no one single projection can accurately reproduce the whole pattern from a tip, because the radius of curvature may vary by as much as a factor of two over the surface of a normal tip. Hence a different projection might be used for separate regions of the tip. Treated this way, it turns out that separate regions are individually close to stereographic projections.[18] Obviously each region will have a different center of projection.

The shell model has been applied mainly to two kinds of problems: images of solid solutions and of faulted crystals. The former is a nice illustration of the flexibility of the model. In the solid solution the solvent and solute atoms are given different field evaporation and imaging criteria. For instance, the solvent atoms may be imaging when within the distance P from the surface, whereas the solute may field evaporate when closer to the surface than Q', and image when between Q' and P'. In this case the solute would be preferentially removed by field evaporation. P' may, on the other hand, be greater than P, i.e. the solute atoms would image at greater depth than the solvent atoms. By varying the values of the parameters P, P' and Q', computed images that agree with images observed in the microscope may be obtained. Some success with this method has been reported by several authors.[16,19-22]

Simulation of images of faulted crystals is the subject of the next section.

2. Simulation of Dislocation Contrast

Images of faulted crystals are simulated by first introducing the fault into the lattice and then applying the shell criterion. For dislocations the procedure is to position the dislocation line in the crystal, compute the displacements of lattice atoms caused by the presence of the dislocation, and then apply the shell model to the strained crystal. In this case the interest is focussed on some limited region of the image, usually the area surrounding some particular pole. Hence the problem of varying projection does not arise. The shell model has been applied in this manner to single dislocation lines,[23-25] dislocation loops,[11,25-27] dissociated dislocations,[28] and stacking faults,[29] all in cubic crystal

Similar investigations for the hexagonal lattice have also been carried out. Perry and Brandon[30] have extended their models for the cubic lattice to dislocations, loops and dipoles, stacking faults and twinning in the hcp lattice. Ranganathan[31] has investigated the constrast from the various stacking faults in hcp. These results will not be discussed further here.

Ranganathan[29] has simulated the contrast of an intrinsic and an extrinsic stacking fault running through a fcc lattice. He finds that the extra layer in the extrinsic case will be resolved. Hence a distinction between intrinsic and extrinsic faults could be made by inspection. It is somewhat doubtful, however, whether this find detail would be resolvable in the microscope.

Sanwald, Ranganathan and H'ren[23] were the first to apply the technique to dislocations. They chose the highly idealized case of

a pure screw dislocation in fcc emerging in the center of three {420} planes, the (204), (402) and (420). With a Burgers vector of $\frac{a}{2}$[110] the $\vec{g} \cdot \vec{b}$ criterion predicts one, two, and three leaved spirals respectively in these cases, which was nicely demonstrated in the simulated patterns. In a later paper[25] more general cases were treated. The dislocation lines were made to intersect a set of plane edges rather than the center of a plane. In this case the spiral structure of the image was not as immediately obvious as in the previous case. It was shown that an edge dislocation and a screw dislocation with the same Burgers vector emerging in the same place will cause virtually identical contrast. This is a highly artificial situation, since it requires at least one of the dislocations to emerge at a rather shallow angle to the surface. The strong image forces in a field ion tip are expected to force dislocations to emerge normal to the surface. The result did, however, confirm the idea that only the normal component of the Burgers vector is important in determining the long range contrast effect. The model was finally used in matching simulated images to actual experimental images showing rather complex contrast effects that were thought to possibly arise from dislocations.[25] These contrast effects were successfully simulated as resulting from pairs of dislocations and dislocation dipoles. The latter case is identical to a dislocation loop intersecting the surface. It was not possible to uniquely determine the Burgers vectors of the dislocations, since several pairs of Burgers vectors would have given the same contrast. It was felt, however, that a field evaporation sequence would have resolved that problem.

Brandon and Perry have investigated a number of dislocation configurations in a series of papers.[24,26-28] In the first paper[24] they simulated the image of a bcc crystal containing a simple perfect dislocation. In their model the dislocation line emerges normal to the surface. It is, in fact, taken to pass through the center of the hemispherical crystal. The orientation of the dislocations is thus generally mixed. Plots of dislocations with Burgers vectors $\frac{a}{2}[\bar{1}11]$ and $\frac{a}{2}[1\bar{1}\bar{1}]$ respectively, emerging in the $(\bar{1}23)$ plane were shown. With the small tip radius used (80 lattice constants) the $(\bar{1}23)$ plane edges were not resolved, but the effect of changing the Burgers vector was clearly visible in the (011) plane rings (for (011) $\vec{g}\cdot\vec{b}$ equals +1 and -1 respectively for the two Burgers vectors). The "extra half (011) plane" appeared on opposite sides of the dislocation in the two cases. The effect of increasing the tip size was illustrated by doubling the tip radius. In this case the triple spiral on $(\bar{1}23)$ was resolvable ($\frac{a}{2}[\bar{1}11] \cdot \frac{1}{a}[\bar{1}23] = 3$). A case with $\vec{g}\cdot\vec{b} = 0$ ($\vec{b} = \frac{a}{2}[111]$) was also plotted. A comparison of this plot with a plot of a perfect crystal indicated some differences in image points far from the point of emergence of the dislocation, but no obvious contrast was visible. Hence the condition $\vec{g}\cdot\vec{b} = 0$ was demonstrated to be a true invisibility criterion.

This work was later extended to fcc and bcc crystals containing a single perfect dislocation loop or dipole.[27] Both the loop and the dipole were approximated by a pair of straight, parallel dislocations of opposite sign. The axis of symmetry of the dipole (i.e. the line

parallel with the dislocations halfway between them) was made to pass through the center of the hemispherical crystal, and the center of a lattice plane (hkℓ). It follows that the line of symmetry is normal to the (hkℓ) plane. The separation of the two dislocations was also varied. This corresponds to varying the diameter of a loop. Cases considered were dipoles with Burgers vectors $\frac{a}{2}[011]$, $\frac{a}{2}[11\bar{1}]$ and $\frac{a}{2}[\bar{1}10]$ in fcc centered on $(\bar{1}35)$, and a dipole with Burgers vector $\frac{a}{2}[\bar{1}11]$ centered on $(\bar{1}23)$ in bcc. The conclusions were that loops and dipoles can be identified as spirals of opposite sign as long as the two dislocations emerge in the same pole region (provided $\vec{g}\cdot\vec{b} \neq 0$ for that pole). If the dislocations emerge in different planes this identification need not be obvious, and is impossible if $\vec{g}\cdot\vec{b} = 0$ for one dislocation. If the spacing between the dislocations is small the effect may be a distortion of the image in the surrounding region rather than recognizable spirals. The dislocation spacings used were 10 and 20 lattice constants. One of the loops considered was artificial ($\frac{a}{2}[11\bar{1}]$ in fcc), since its Burgers vector is not a lattice vector. Hence the loop was faulted and it was noted that the fault was visible as a line of displacements of lattice planes where these cross the fault. These results were essentially verifications of the conclusions of the intuitive theory.

In a third paper[28] stacking fault ribbons in a fcc crystal were considered. Stacking fault ribbons arise from dissociation of perfect dislocations into two partial dislocations bounding a stacking fault. The partial dislocations were taken to be parallel to each other and to the line of the perfect dislocation. The line of symmetry emerged

at the center of a plane. In this case the dislocations were not forced to emerge normal to the surface. Cases considered were:

a) $\frac{a}{2}[011] \rightarrow \frac{a}{6}[121] + \frac{a}{6}[112]$ emerging on (011)

b) $\frac{a}{2}[011] \rightarrow \frac{a}{6}[\bar{1}12] + \frac{a}{6}[121]$ emerging on $(\bar{1}35)$

c) as b) emerging on $(\bar{1}11)$ plane edges (off center).

In a) $\vec{g}\cdot\vec{b} = 2$ and $\vec{g}\cdot\vec{b}_1 = \vec{g}\cdot\vec{b}_2 = 1$. This means that each partial should start a single spiral, whereas the combined effect should be a double spiral. Since $\vec{g}\cdot\vec{b}_p = 1$ there should be no trace of the stacking fault across the (011) plane edges. All these features were clearly displayed in the simulated image. The stacking fault width was 20 lattice constants. In b) $\vec{g}\cdot\vec{b} = 4$, $\vec{g}\cdot\vec{b}_1 = 7/3$, and $\vec{g}\cdot\vec{b}_2 = 5/3$. This is a very complicated configuration with a four-leaved spiral expected and observed for the undissociated dislocation. Even a small splitting with a stacking fault width of six lattice constants obscured the contrast considerably, and splitting the dislocation still more (20a) concealed the fourfold spiral completely. Actually the fault was hardly visible in the latter case. In c) $\vec{g}\cdot\vec{b} = 1$, $\vec{g}\cdot\vec{b}_1 = 2/3$ and $\vec{g}\cdot\vec{b}_2 = 1/3$. The expected splitting of the (111) plane edges was verified. It was concluded, however, that the $\vec{g}\cdot\vec{b}$ rule was of little help in determining the partial Burgers vectors. The complicated configuration (case b) treated in this paper pointed clearly to the limitations of the intuitive approach to analyzing images. There is little hope that the breaking up of the fourfold spiral by dissociation of the dislocation could be inferred from the image by inspection.

Brandon and Perry[26] finally applied their model for loops and dipoles[27] to the analysis of an actual image of an iridium tip

containing three defects intuitively identified as perfect dislocation loops. The diameters of the loops had also been determined by measurement on the micrograph. The procedure in simulating the images involved determining the local tip radius in the region of a defect from the micrograph, and also tentative values for the point of emergence of the center of the dipole as well as the width of the dipole. The width of the dipole was then adjusted until a best fit with the actual image was obtained.

Excellent agreement between actual and simulated images was obtained in this manner although an unambiguous determination of Burgers vectors could not be made since several alternatives gave the same contrast.

The intuitively predicted loop size turned out to be consistently overestimated by about 20%. The size of a loop is estimated by finding the point of emergence of the bounding dislocations. This cannot always be done accurately since a dislocation may emerge far away from image points, e.g. between two plane edges, in which case the point of emergence is not well defined in the image. Lattice strain surrounding the point of emergence may in addition cause image distortions.

In this paper and in the paper by Sanwald and Hren,[25] it was thus demonstrated convincingly that the shell model can be applied to dislocated crystals. Brandon and Perry[26] also outlined a general procedure for obtaining quantitative data from field ion micrographs, namely to vary the parameters of the model until a satisfactory agreement with the actual image to be simulated is obtained.

Son and Hren[11] have presented a model for the simulation of Frank loops in the fcc lattice. The elastic displacements of the loop are derived from a pair of edge dislocations with Burgers vector $\frac{a}{3}$ [111], using standard expressions from the dislocation theory. The positioning of the loop in the lattice is not clearly indicated. Figure 14a is a sketch of one of the plots from Son and Hren which shows the simulated contrast of a tip containing an intrinsic loop.

The image plane is (220) and the plane of the loop (111). It is pointed out that the smallest half-ring must be missing in the plot. This is clearly so, since the breaking of the second ring indicates that the top half will become the bigger half-ring. This is the expected contrast for an intrinsic stacking fault.[29] The configuration in Fig. 14 cannot, however, apply to the case of a loop on (111), with Burgers vector $\frac{a}{3}$ [111], intersecting (220). This case would yield $\vec{g}\cdot\vec{b}_p = 4/3$, which indicates that a double stepped spiral should develop according to the intuitive theory described above. Although it is likely that a clear double spiral would not develop in the case of a small loop that essentially intersects only one plane edge at a time, the configuration in Fig. 14a is not possible. The regions marked 1 and 2 on the plot are on the same plane on opposite sides of the fault. This means that region 2 must be 4/3 plane spacings above region 1. Region 3 is only one plane spacing above region 1, being the next plane on the same side of the fault. Hence region 3 must be below region 2. A possible image based on this reasoning is sketched in Fig. 14b. Son and Hren then use their model trying to match actual images of a tip of quenched and annealed platinium, which, due to

this treatment, is expected to contain vacancy clusters. A defect on the (011) plane edges is simulated as an intrinsic, and an extrinsic Frank loop, and a prismatic (perfect) loop respectively, the loop plane being (111) in all cases. The plots simulating Frank loop contrast do not display the features predicted by the geometrical theory, i.e. a stepping of (001) plane edges across the stacking fault. Rather the image rings break in irregular places and it is quite clear that the model of Son and Hren is in error and does not reproduce Frank loops.

D. Experimental Observations

So far the discussion has dealt exclusively with the development of a contrast theory for faulted crystals, and its subsequent confirmation by computer simulation. This section is included to indicate that the basic ideas of the theory are satisfactorily documented in experimental observations. Indeed, as is usually the case, the theory did not develop out of a vacuum, but rather in conjunction with observations of contrast effects suspected of being caused by dislocations. Some early observations were reported in the late 1950's, and early 1960's,[32] but systematic investigation of dislocation contrast did not start until Pashley,[6] and Ranganathan[5] proposed the formation of image spirals in 1966. The bulk of dislocation observations has been reported out of the University of Cambridge. A summary of the situation up to early 1970 is included in reference 9.

A one-leaved spiral on the (111) plane of an iridium specimen is reported by Smith and Bowkett.[9] This corresponds to the emergence of a perfect dislocation with Burgers vector of the type $\frac{a}{2}\langle 110\rangle$. Smith, Morgan, and Ralph[33] have observed a double spiral in the (110)

pole of an iron specimen. This is deduced to be due to a dislocation with the unusual Burgers vector a[110]. Page[34] has shown micrographs of iridium tips displaying a three leaved spiral on the (331) plane, which, again, corresponds to a perfect dislocation with Burgers vector $\frac{a}{2}[110]$. Thus the $\vec{g}\cdot\vec{b}$ criterion seems to be working excellently for perfect dislocations.

Images with perfect dislocation loop contrast have been published by Fortes,[18] who observed these in iridium. Similar micrographs were published by Brandon and Perry[26] in their computer study of loops in iridium.

The reported observations on faulted loops and stacking faults are few. Fortes and Ralph[35,36] claim to have identified dislocation loops of Shockley type in iridium specimens that had fractured in the microscope during imaging. The observed contrast was of the stepped spiral type as predicted by the theory. As mentioned above, the theory cannot distinguish between Frank loops and Shockley loops. In this case Frank loops were counted out since they were considered to form only as a result of point defect condensation and the density of the loops was so high that for them to be of Frank type would have required unreasonable point defect concentrations. Shockley loops have never been observed in other situations than in the field ion microscope. They are thought to have nucleated in a fracture process at the theoretical strength of iridium. Images of possible Frank loops in platinum are shown by Son and Hren[11] in their computer simulation of Frank loop contrast.

Dissociated perfect dislocations have been observed in iridium. Smith, Page and Ralph[37] have published micrographs of a field evaporation sequence showing the following: in the first micrograph a continuous spiral starts at the innermost image ring, indicating that the ring encloses a perfect dislocation. After some field evaporation the second ring breaks into a step at one point, i.e. the image configuration becomes the stepped spiral of a dissociated dislocation. After further field evaporation the innermost ring closes, indicating that it no longer encloses the dislocation, whereas a continuous spiral starts with the second ring. This sequence indicates that the width of the dissociated dislocation is small enough for the stacking fault ribbon to fit within the first ledge of the pole in question. Each time a plane edge sweeps over the stacking fault ribbon, the corresponding image ring breaks into a step. This work has been followed up by further observations in iridium and iridium based dilute alloys.[38] Cases corresponding to various combinations of p- and q-values (Eqs. II-4 and II-5) have been observed. In some instances, the kink that should form in a plane edge, when it crosses a stacking fault for which q = 1 (or any integer), was resolved. These investigations provide a method for measuring stacking fault energies by estimating the width of the stacking fault ribbon. The latter can be done by fair accuracy by determining the local topography of the surface, especially the ledge width. A fine scale field evaporation sequence will reveal the width of the stacking fault in relation to the ledge width. The ratio of stacking fault energy to shear modulus is related to the width of the stacking fault.

E. Summary

Although actual observations of dislocation contrast in the field ion microscope are not abundant, most of the features predicted by the theory have been documented, and it thus appears safe to say that the theory rests on sound ideas.

All examples used to illustrate the theory are obviously over-simplified in that dislocations are taken to emerge at, or close to, the center of poles, and stacking faults to straddle poles. This is done merely for clarity, and does not limit the applicability of the principles involved to those areas alone. It turns out, however, that most observations are made close to low-index poles as well. The reason for this is simply that the ledge width of the lattice planes gets smaller away from the pole, i.e. the ring structure gets denser. This means that the breaking, and especially the stepping, of the rings is hard to distinguish from artefacts in high index regions.

For faulted loops the situation is not very satisfactory. The report on observation of Shockley loops by Fortes and Ralph[35] is not entirely convincing. If the loops are homogeneously nucleated by shear stresses in the tip, one would expect them to continue to grow under the action of the stresses until they are essentially stacking faults running through the tip. The interpretation of the contrast also seems vague. Figure 3 of reference 35, for instance, shows a clear case of a stepped spiral with $|q| < 1$, and yet it is interpreted as a kinked spiral with $|q| = 1$. Son and Hren[11] have presented some micrographs of quenched platinum claiming that these display image contrast of intrinsic Frank loops. Although this may be the case,

this interpretaion is not convincingly backed up, even disregarding the fact that their computer model is in error. The images in question show no systematic features that could be used to characterize other images. More systematic observations would be badly needed in this area.

Most previous computer simulations have not really brought out anything new, but rather verified intuitively derived results. The exception would be some of the work of Brandon and Perry; to wit, their treatment of a complex case clearly outside the capability of intuition,[28] and their pointing to a way of extracting quantitative data from ion micrographs with the aid of the computer.[26]

The case of very small dislocation loops has not been discussed specifically in the literature. This is surprising since the observation of small lattice defects would appear to be an application where the unique capability of the ion microscope would most strongly come to its own.

III. SIMULATION OF FRANK LOOP CONTRAST

A. Model for Computation

1. Displacement Field of Dislocation Loops

The displacements caused by a closed dislocation loop in an isotropic elastic continuum were first derived by Burgers. The result, in vector form, is given by Hirth and Lothe[8] in the following notation:

$$\vec{u}(\vec{r}) = \int_A \frac{\vec{R}\cdot d\vec{A}}{R^3} - \frac{1}{4\pi}\oint_C \frac{\vec{b}\times d\vec{\ell}'}{R} + \frac{1}{8\pi(1-\nu)}\,\mathrm{grad}\oint_C \frac{(\vec{b}\times\vec{R})\cdot d\vec{\ell}'}{R} \quad . \qquad \text{(III.1)}$$

The coordinate system is illustrated in Fig. 15. Here $\vec{u}(\vec{r})$ is the displacement of point $\vec{r}$ caused by the dislocation loop C. The dislocation loop is created by cutting over the surface A and displacing the negative side of the cut by $\vec{b}$ relative to the positive side. In this process material, in the amount $\delta V = \vec{b}\cdot d\vec{A}$, will have to be inserted or removed. In Eq. (III.1) $\vec{b}$ is the Burgers vector, and $d\vec{\ell}'$ is the differential line element at point $\vec{r}'$. The vector $\vec{R}$ is defined as $\vec{r}'-\vec{r}$. A sense has to be ascribed to the dislocation line in order to define the positive sense of $d\vec{A}$ and of $\vec{b}$. The positive sense of $d\vec{A}$, which is the positive normal to the surface element dA, is defined by the requirement that if C were to shrink continuously in A until it just bounded dA, it would encircle $d\vec{A}$ in the positive sense. The Burgers vector $\vec{b}$ is defined by a Burgers circuit as follows: Looking along the positive sense of the dislocation line a clockwise Burgers circuit, enclosing the dislocation line, is formed in the crystal. The same circuit is then formed in a perfect reference crystal. The latter circuit will fail to close, and the vector drawn from finish (F)

to start (S) of this open circuit is the Burgers vector. Since the sense of the Burgers circuit is that of a right-handed screw, this rule is known as the FS/RH convention. If the dislocation loop is faulted the Burgers circuit must begin and end on the stacking fault.

With the use of the general expression in Eq. (III.1) the displacements produced by an arbitrary dislocation loop can be obtained by integration over the loop. This means that the primed coordinates are integrated out and the displacement vector $\vec{u}$ remains a function of $\vec{r}$ as required.

2. Geometry of Frank Loops

In this work the shape of the loops is taken to be a regular hexagon in all cases. This choice is based mainly on computational convenience. It is a physically plausible choice, however, since Frank loops must be bounded by ⟨110⟩ directions, of which there are three on each {111} plane, 120° apart. The coordinate system used for displacement calculations is illustrated in Fig. 16a. The origin is at the center of the loop, and the z-axis is [111], the x-axis $[1\bar{1}0]$, and the y-axis $[11\bar{2}]$. The parameters used to describe the loop are shown in Fig. 16b. For the regular hexagon x_1, x_2, and y_2 are related so that $x_1 = 2x_2$ and $y_2 = \sqrt{3}\, x_2$. The size of the loop will be reported as the number of atoms contained along its diagonal. The loop illustrated in Fig. 16b is a "five atom loop".

For the configuration of Fig. 16 the line integrals in Eq. (III.1) can be solved analytically using elementary functions (square root and logarithm). The surface integral can be integrated only once in closed form, however, over either x' or y'. For the second integration

numerical methods have to be employed. The integrand is a well behaved function, so no serious problems were to be expected. It turned out, furthermore, that quite rapid convergence was obtained using the Romberg algorithim.[39] In fact, only a few iterations are necessary to achieve an accuracy of one part in 1000, which is quite satisfactory in this case. Hence the necessity to resort to numerical methods for one of the integrals is of little significance for the computer program. The expression for the displacement of a lattice point, can thus be written as a function of the coordinates of the point (x, y, z) and the size of the loop (x_2). The only information about the loop that needs to be fed into the computer is the position of its center (x_o, y_o, z_o) in lattice coordinates, and its size.

3. Lattice Model

For computer simulation a fcc point lattice is built up by stacking (111) planes in proper sequence. This choice of basis for the lattice model greatly facilitates the introduction of Frank loops. The lattice coordinate system is orineted as the coordinate system used for the loop displacements (Fig. 16a), i.e. the [111] is the z-axis, $[1\bar{1}0]$ the x-axis and $[11\bar{2}]$ the y-axis. Typically the region surrounding some low index pole is of interest. The simulation procedure begins by selecting the radius of the tip and then determining the approximate coordinates of the center of the pole. This is taken as the center of the plot, and usually an area around the center with a radius of about 20 lattice constants is plotted. The computer scans lattice points in one (111) plane at a time, following the trace of the surface in that plane. For each point the displacement due to the

dislocation loop is determined first, and then the distance of the displaced lattice point from the origin is computed. This distance is compared with the shell radii. If it falls between them the point is stored as an image point, otherwise the point is ignored. On the average somewhat less than ten lattice points have to be scanned for every image point. For a vacancy loop the lattice points corresponding to the vacancies have to be skipped. This is especially easy to program in the used geometry, since these lattice points are all in one plane. The interstitials in the interstitial loop have to be bodily introduced into the lattice. Since they in no way affect the calculation, they can be introduced at the end of the program. It turns out that the interstitials themselves seldom are seen as image points. What is important then, is the displacement field and not the disc of interstitials.

4. Surface Relaxation

The effect of the surface on the displacement field has always been ignored in previous simulation studies. This has, undoubtedly, been due largely to the complexity of the problem. It is well recognized in the theory of dislocations that the treatment of the surface image force is a complicated problem. The simplest case is a screw dislocation lying parallel to the surface, in which case the boundary condition of a stress free surface is satisfied merely by superposing the strain field of a screw dislocation of opposite sense lying in the mirror position outside the surface. The solution for an edge dislocation in the same position already requires lengthy mathematics, since the simple image construction alone is not enough. The case of a straight dislocation inclined to the surface has been treated but is exceedingly complicated,

and the solution for a curved dislocation is intractable. The recommended procedure, in view of these difficulties, is to use the simple image construction as a first approximation in all cases.[8]

In the case of Frank loops it is rather obvious that surface relaxations will play a significant role in determining the displacements, especially for a loop inclined to the surface at a small angle. An attempt was therefore made to take this effect into account by the simple procedure of superposing the displacement field of a mirror loop of the opposite kind to the actual loop. This configuration is illustrated in Fig. 17 for a vacancy loop with an image loop of interstitial type. The mathematics involved is straightforward. The coordinates of the point at which the displacement is being evaluated need only be redefined with respect to a new coordinate system centered at the image loop. Once this is done, the original expressions apply unchanged for the displacement due to the image loop. The procedure is as follows: the displacement $\vec{u}_1$ of point (x, y, z) due to the real loop is computed first using expressions derived from Eq. (III.1). Then the position of the point relative to the coordinate system centered at the image loop is determined from the equations

$$\begin{aligned} x' &= -x \\ y' &= y\cos 2\phi - z\sin 2\phi + 2D\sin^2\phi \\ z' &= D\sin 2\phi - y\sin 2\phi - z\cos 2\phi \quad , \end{aligned} \tag{III.2}$$

and the displacement $\vec{u}_2$ due to the image loop is computed using these coordinates in the same expressions. Finally $\vec{u}_2$ is tranformed back to the original coordinate system, and added to $\vec{u}_1$ to yield the total

displacement $\vec{u}$. D is the distance of the center of the loop from the surface, and ϕ the angle between the plane of the loop and the surface (Fig. 17).

The displacement field surrounding a Frank loop is largely confined to a cylinder placed through the loop with its axis along the normal to the loop plane. Within this cylinder the displacements are essentially in the z-direction, although there are lateral components, especially close to the partial dislocation. It is to be expected therefore that the effect of the surface on the displacement field will depend greatly on the angle between the plane of the loop and the surface plane (ϕ in Fig. 17). If ϕ is small the displacement field will evidently reach the surface while the loop is still some distance below the surface, whereas this is not the case if ϕ is about 90°. Inspection of Fig. 17 also reveals that if ϕ is larger than 45° the displacements of the image loop would counteract those of the real loop for atoms on the surface. The component of displacement normal to the surface would, however, still enhance that of the real loop, so the simple image construction would probably be useful even in this case. It is also apparent from Fig. 17 that the part of the surface below the loop will not be much affected by the presence of the loop, and hence it must not be much affected by the mirror loop, which is clearly the case when ϕ is small.

When the loop breaks through the surface the mirror loop will be reflected into the crystal as illustrated in Fig. 18. Although no analytical difficulties will arise from this situation, it does not appear satisfactory, mainly because it will result in strong

displacements of surface atoms below the loop. The natural way around this problem would be to truncate the loop, and hence also the mirror loop, at the surface, simply because there can be no loop outside the surface. There is, however, a problem corrected with this procedure as well. Figure 19 is a view of a $(\bar{1}10)$ plane cutting through a vacancy loop on (111) under (110). A hexagonal loop will emerge on (110) with one of its legs parallel to the surface. When this leg is still beneath the surface it constitutes a partial edge dislocation parallel to the surface. If the loop is cut off at the surface, this dislocation will remain in the surface and thus prevent the surface atoms below the loop from relaxing upward. When the surface sweeps past atom A in Fig. 19 the lower part of the crystal, close to the surface, would probably relax upward a little to make the lattice planes straight, since there no longer is an extra half plane to bend them down. This would probably happen even before the surface gets past A. Leaving the dislocation in the surface will, however, simulate the situation as it existed before the surface swept into the loop. The simplest way to ensure proper relaxation of the lower part of the lattice is to move the parallel leg of the loop some distance outside the surface as soon as the loop begins to break through. Simulating Frank loops by a dipole pair of straight dislocation corresponds to moving the closing leg of the loop to infinity. In a case where the surface has cut well into the loop this problem will be taken care of automatically if the displacements are derived by integrating over the full loop even if part of it is outside the crystal. This is a fortunate situation since it requires no special action whatever to be taken in the computation.

A similar situation is at hand with respect to the mirror loop. It can be treated in a similar fashion by letting the mirror loop extend into the crystal. To avoid the strange displacements of the lower part of the surface caused by this procedure (see Fig. 18), the displacements of the mirror loop should be applied only to the part of the crystal above the loop.

The discussion of the emergence of the loop at the surface is probably academic in that the details of the breaking through to the surface would hardly be observable in the microscope. The surface relaxation on the other hand is certainly significant, especially where it will cause displacements normal to the surface, which it in most cases will. The merit of the simple approaches to the problem suggested above can only be tested against experimental observations which are lacking at present. A comparison of the different simulation models will be made in the next section.

5. Field Evaporation

Many of the plots in the next section will be presented as simulated field evaporation sequences. In the microscope, field evaporation results an increase of the radius of the tip, and in order for the surface of the tip to move into the tip in this case, the center of curvature of the surface must be moving down along the tip axis. The simplest way to simulate field evaporation in computer plots would be to reduce the radius of the tip between plots, keeping the center of the spherical shell fixed. If the amount of field evaporation is small, say a few percent of the radius, the increase in curvature would hardly be noticeable. With a tip radius of 100 lattice constants the

removal of three (110) planes would result in a one percent reduction of the radius.

A more realistic field evaporation sequence may be produced by increasing the radius by ΔR and moving the center of the shell down along the tip axis by an amount Δz which is larger than ΔR. If the tip is assumed to be a spherical cap sitting on top of a truncated cone of half angle α (Fig. 20a)[9] it is easily shown that

$$\Delta z = \frac{\Delta R}{\sin\alpha} \quad . \tag{III.2}$$

The angle α is typically about 25° which means that Δz should be about 2.5 ΔR. For a region at an angle θ from the axis (Fig. 20b) one must obviously have

$$\Delta z > \frac{\Delta R}{\cos\theta} \quad , \tag{III.3}$$

otherwise the surface in this region would actually move outward when R is increased by ΔR. As long as θ is smaller than the complement of α, Eqs. (III.2) and (III.3) are clearly consistent, and in the conical model (Fig. 20a) the largest possible value of θ is, of course, $90°-\alpha$. If the exact simulation of the field evaporation of a particular tip is significant one should measure $\Delta z/\Delta R$ by controlled field evaporation.

The difference between this procedure and simply shrinking the surface concentrically cannot be detected in the plots of a small evaporation sequence. For long sequences, especially in regions far from the axis, the difference will clearly be significant however, and the more realistic procedure of increasing the radius has usually been used. When this procedure has been used, a simulated field evaporation sequence strictly corresponds to a [111] oriented tip.

B. Results

1. Check of Model

In this section some simple defect configurations will be simulated with the model described above, in order to demonstrate that the model produces results in agreement with the image theory. Computer simulation using the shell model should clearly lead to similar results as the intuitive approach. They are after all only different ways of applying the same theory. Comparing the two can therefore only verify that the theory has been applied correctly in both cases, and in no way does it verify the theory itself. The only test of the theory would, of course, be comparison with experimental observations. This section is hence offered as proof that the computer program is correctly written, to the extent that it does reproduce some generally agreed upon results, to wit, the case of a stacking fault running through the crystal, and the case of a stacking fault with one partial emerging in the center of a pole. The former can be simulated, with the present model, by making the Frank loop large enough, and positioning it so that it is cut by the surface. If only a limited region of the surface is plotted it is enough to make the loop so large that both partials emerge outside the plot. The latter case is produced by positioning a loop so that one partial emerges in the center of a pole and the other again outside the plot. The predicted contrast in these cases was discussed in connection with Figs. 5, 6, 7 and 12.

Figure 21 shows four plots of the region around the $[\bar{1}\bar{1}1]$ pole. In Fig. 21 (a) and (b) a Frank loop intersects the surface from one side of the pole to the other, and in Fig. 21 (c) and (d) one Frank

partial emerges in the center of the pole with the loop to the left of the pole. The faults are all on (111), and the plots are oriented so that the [111] pole is up, i.e. the (111) plane is slanted down into the paper, away from the viewer. All plots will be thusly oriented. The faults in Fig. 21 (a) and (c) are intrinsic, those in Fig. 21 (b) and (d) are extrinsic.

The rules of the geometrical theory are clearly displayed in these plots. In this case q ($=\vec{g}\cdot\vec{b}$) is 1/3, which in Fig. 21a means that the upper part of the crystal should be 1/3 plane spacing below, or 2/3 above, the lower part. Figure 21a looks somewhat strange in that the top ring is closed below the stacking fault. This is a perfectly possible situation, however. The fault is just crossing somewhat above the center of the pole. In the computer plot it is clearly possible to distinguish between a step size of 1/3 and 2/3. Thus in Fig. 21a the top half-rings are either 1/3 larger or 2/3 smaller than the lower half-rings, whereas in Fig. 21b the top half-rings are either 2/3 larger or 1/3 smaller than the lower half-rings. The two cases are hence opposite, and it would be possible to deduce the nature of the fault merely by inspection. This, however, is based on the possibility to distinguish between a step size of 1/3 and 2/3 of the ledge width in these well resolved computer plots which need not be the case in an actual image. In Fig. 21 (c) and (d) the opposite sense of the spirals should be noted. These plots also verify that the computer program actually reproduces the correct lattice structure. The atomic configuration of the top planes is clearly that of a {111} plane.

Figure 22 shows four corresponding plots for the (001) plane. In this case the value of q is 2/3, and the expected differences with respect to Fig. 21 are clearly displayed. For instance for the intrinsic fault in Fig. 22a the top half-rings are either 1/3 smaller or 2/3 larger than the lower half-rings, i.e. precisely opposite to the case in Fig. 21a. The atomic configuration on the top plane is seen to be the correct {001} configuration, and the senses of the spirals in Fig. 22(c) and (d) are opposite as they should be.

In Fig. 23 four similar plots for the (113) plane are displayed. This is a case with q = 5/3, which means that the integral residue of q, q', is 2/3. Hence the stacking fault in this case should behave as that in Fig. 22. Comparison of Figs. 22a and 23a, for example, shows that this is indeed the case. Since q is greater than one a new element is introduced into the cases where one partial emerges within the plot. It can be seen that the spirals are stepped by more than one ledge width, i.e. the stack of (113) planes has essentially become two interleaved stepped spirals. Again the atomic configuration is correct and the spirals in Fig. 23 (a) and (d) have opposite senses.

If q is between two and three, the step size should be between two and three ledge widths, and three interleaved, stepped spirals result. Such a case is illustrated in Fig. 24 for a Frank loop intersecting the [112] pole, in which case q = 8/3. Again q' is 2/3 and the stacking fault shows the same contrast as in Fig. 22, although the smallest half-rings are on opposite sides of the fault, which, as discussed previously, is purely incidental. The spiral structures in Fig. 24 (c) and (d) are as expected, and the senses are opposite in the two cases.

The tip radius in all cases was 100a except for the (112) plane, where it was doubled in order to better resolve the (112) plane edges. In the latter case the shell thickness (P) was also somewhat greater than the ideal value for the same reason. The loop size was 201 atoms for the stacking fault simulation, with the loop centered on the pole, and the surface cutting the loop somewhat outside its centerline. This positioned the partial dislocations well outside the plots in all cases. One can indeed follow the stacking fault all through the plot, although it is virtually invisible outside the fourth or fifth ring on the (112) plane. For the cases where one partial emerges in the center a 81 atom loop was used, centered 40 atoms to the left of the pole. This again positioned the left partial outside the plot.

Based on these plots it seems safe to say that the computer program is correct, and hence will produce true results in terms of the geometrical image theory. All plots in this section were computed without use of a mirror loop for the displacement calculations, i.e. surface relaxation was not taken into account. This was done, of course, in order to enable direct comparison with the intuitively derived results.

2. Effect of Mirror Loop

The effect of surface relaxation on the image contrast will be examined by comparing plots of the same configuration, made without and with the mirror loop in the different ways described in the preceeding section. The first example is a 31 atom vacancy loop on (111) under (110) in a tip with a radius of 375 lattice constants. Figures 25-28 show four versions of a simulated field evaporation sequence during which somewhat less than one (110) plane is removed from this tip. The sequence is simulated using four different models in Figs. 25, 26, 27 and 28 respectively. In Fig. 25 the displacement field of the vacancy loop alone is used with the loop extending outside the surface. In Fig. 26 mirror loop displacements were superposed to the upper part of the crystal, and in Fig. 27 to the whole crystal. In both cases the mirror loop extended into the crystal. In Fig. 28 both the real loop and the image loop were truncated at the surface. The positions of the partial dislocations are marked by crosses.

On the label above each plot the distance of the loop from the surface is given as D/y_2, where D is the distance of the center of the loop from the surface as indicated in Fig. 17, and y_2 is the "height" of the loop as defined in Fig. 16. Hence the distance is "one" when the leading edge of the hexagon is in the surface, zero when the center of the loop is in the surface, and negative when more than half of the loop is outside the surface. The last line on the label gives the coordinates of the center of the loop. K_o, L_o and M_o correspond to x_o,y_o and z_o respectively. K_o measures the distance of the center of the loop from the center of the plotted pole in units

of half the interatomic distance along ⟨110⟩ . The unit of L_o is that of K_o divided by $\sqrt{3}$, and M_o is the ordinal number of the (111) plane containing the loop counted from the bottom of the hemispherical crystal (M = 0 is the bottom plane). Since an interstitial loop must lie between two ordinary lattice planes, the corresponding number for the interstitial loop is a half integer designated HM. P is the shell thickness in units of the interatomic distance along ⟨110⟩ , i.e. $a/\sqrt{2}$. The rest of the label is self-explanatory.

The difference between the models used in Figs. 25 and 26 is that the surface region above the vacancy loop is pushed further into the tip by the image loop in the latter case. The effect of this is most clearly evident in Figs. 25d and 26d, where the top half plane below the fault has just been removed. In Fig. 26d an extra half plane is retained above the fault. This is not unreasonable since, in this case, q = 4/3 which means that the smallest half plane below the fault in Figs. 25c and 26c is actually higher than the smallest half plane above the fault, and hence should be removed first. Obviously this applies only to that part of the plane immediately below the fault, since the plane is spiralling around the partial dislocation to the other side of the fault. One would therefore expect the edge of this plane to circle around the edge of the loop when the top half plane above the loop disappears. This is essentially what happens in Figs. 25c and 25d. It would not, however, take much extra depression of the surface above the loop for the situation in Fig. 26d to arise, and hence it is far from obvious that this situation is unrealistic. In Figs. 25 and 26 the parts of the plots that are below the fault should, of course, be identical, as they are.

If the image loop displacements are applied to the lower part of the crystal as well, this part will be pushed toward the surface. The result of this is evident in Fig. 27 where the top half plane below the loop is seen to shrink away much faster than in Fig. 26. The edge of the following plane is also beginning to show already in Fig. 27c just below the fault. This behavior, as well as the model itself, seems rather unreasonable and the model will not be further used.

The most dramatic change in the image is brought about by truncating the loop, and its image loop, at the surface. The plots in Fig. 28 bear hardly any resemblance to those in Figs. 25, 26 and 27. In this model the surface region below the loop will be little displaced from the undisturbed position. This is evident from Fig. 19. The part of the crystal to the right of atom A is hardly displaced at all, and this will be the prevailing situation if the dislocation is locked at the surface. This model will also be discarded, both on the basis of Fig. 28, and due to intuitive objection to the surface configuration it creates.

The configuration discussed above was chosen to correspond to that of Son and Hren,[11] i.e. a Frank loop of about 50 Å diameter in a platinum tip of 1500 Å ($\simeq$ 375a) radius. Actually a 31 atom loop has a diameter of 21a which is about 80 Å in platinum. It turns out that a 50 Å loop (19 atoms) tends to break only one ring at a time, and measurement on the plot of Son and Hren[11] (Fig. 14) reveals that their loop is also close to 80 Å. Hence Fig. 25b should be a reproduction of Fig. 14a which clearly is not the case. The contrast in the plot of Son and Hren (Fig. 14a) corresponds to $q < 1$, whereas q in this case is 4/3 $[\frac{a}{3}(111)\cdot\frac{1}{a}(220)]$.

The effect of the mirror loop when the angle between loop plane and surface is large is illustrated in Fig. 29. The image contrast arising from a 31 atom interstitial loop on (111) under $(11\bar{1})$ is simulated using two models: displacements from the interstitial loop alone are used in Figs. 29a and b, and in Figs. 29c and d displacements from a mirror loop of vacancy type are superposed to the upper part of the crystal. The real loop is extending outside the crystal and the mirror loop is reflected into the crystal as described above. These are the same models as those used in Figs. 25 and 26 respectively. Two stages of field evaporation are shown. In Fig. 29c the smallest top half plane evident in Fig. 29a has disappeared due to the added displacements of the mirror loop, whereas the lower parts of the two plots are identical as they should be. After some simulated field evaporation the smallest top half plane of Fig. 29a disappears as well, and the plot of Figs. 29b results. Figure 29d shows the corresponding case using the image loop. The only difference between these two plots is the larger step size of the broken spiral in Fig. 29d. This is easily understandable in terms of the added displacements along the surface normal caused by the image loop, whereas the added displacements along the surface are too small to show. The spiral in Figs. 29c and d might be characterized by an "effective" q-value greater than 1/3 which is the value of $\vec{g}\cdot\vec{b}$ in this case.

The conclusion of this section, then, is that superposition of the mirror loop displacements to the part of the crystal above the loop plane, leads to reasonable and easily understandable contrast effects, which, in a qualitative sense, do not significantly differ from those

arrived at by using the loop displacements alone. In the following, therefore, the simplest model, that without a mirror loop, will be mainly used, although some plots will be replotted with the mirror loop included to ensure that the results remain valid when surface relaxation is taken into account.

3. Contrast from Loops Wholly Beneath the Surface

If a dislocation loop is completely inside the tip there will be no dislocations intersecting the surface, and hence this is a situation outside the realm of the existing contrast theory. In the case of Frank loops, however, their strong transverse strain field would be expected to cause significant surface displacements before the surface actually reaches the loop. Since these displacements, in most cases, will have appreciable components normal to the surface, image contrast would be expected based on the same geometrical reasoning as in the intuitive theory of dislocation contrast. Computer simulation shows this to be the case very clearly. Only two cases will be considered here: loops on (111) under (113) and $(11\bar{1})$ respectively. In the former case the angle between the plane of the loop is small (29.5°) and in the latter large (70.5°). For the purpose of the next section plots of both vacancy and interstitial loops will be presented.

It may be helpful to clarify the geometry of the plots in this section before presenting them. Figure 30 is a sketch of a loop on (111) under (113). The distance D is measured from the center of the loop to the surface along (111), in units of the radius of the loop, as mentioned above, and h is obviously equal to $D \tan \phi$. If ρ is the number given on the plot labels as "distance from surface" and N the

number of atoms contained along the loop diagonal, then

$$D \simeq 0.6(N-1)\rho\, d_{111} \quad . \tag{III.4}$$

In this case $\tan\phi \simeq 0.57$ and hence

$$h \simeq 0.34(N-1)\rho\, d_{111} \quad . \tag{III.5}$$

For a nine atom loop with $\rho = 2$, h is about 5.5 d_{111}, which means that the point H in Fig. 30 would be in the fifth (111) plane above the plane of the loop. Five planes above the loop displacements are still quite large (see Fig. 19) and image contrast would be expected. This contrast would then be visible some distance above the trace of the loop plane in the surface (L in Fig. 30). As the surface moves toward the loop during field evaporation, point H moves toward point L, i.e. the main contrast effect will be visible closer to the trace of the loop plane. The main effect on the surface would, of course, occur somewhere between H and L, but probably quite close to H. If the angle ϕ is large, however, h would be large, and the effect on the surface, if any, would be much closer to L than to H.

In Fig. 31 some stages of a simulated field evaporation sequence are shown. The configuration is a nine atom interstitial loop under (113). The trace of the plane of the loop in the surface is indicated by an L, and the plane containing the point H of Fig. 30 by an H. The position of the center of the loop is indicated by a vertical line. The presence of the loop first becomes noticeable when its distance from the surface is about five loop radii. In Fig. 31a the central ring

is slightly asymmetric, and in Fig. 31b the asymmetry is quite obvious, although still very small. As field evaporation progresses the asymmetry and displacement off center of the central ring becomes larger (Fig. 31c, d and e), and eventually the ring displays a clear kink as in Fig. 31f. Figures 31c and d are replotted in Figs. 31g and h respectively using the mirror loop model. The effect of superposing the mirror loop displacements is clearly an enhancement of the contrast, i.e. in this case of the asymmetry of the central ring.

Figure 32 shows the contrast of a vacancy loop in the same position as the interstitial loop in Fig. 31. As in the previous case the contrast becomes faintly visible when the distance from the surface is between four and five loop radii (Fig. 32a), and gets stronger as the surface approaches the loop (Fig. 32b, c and d). The effect is again a distortion of the central ring but now in the opposite direction to that in Fig. 31. In Figs. 32e and f the effect of the mirror loop is demonstrated to be an enhancement of the contrast. The configurations are exactly the same as in Fig. 32a and b respectively. The discrepancy in the distance from the surface comes about because it is computed differently in the two programs.

Under $(11\bar{1})$ the loop has to be much closer to the surface to cause visible contrast, as expected ($\phi \simeq 70°$). Once the contrast becomes visible, however, it is qualitatively similar to that discussed above. This is illustrated for a vacancy loop in Fig. 33. In Fig. 33a and b the central ring is somewhat elongated and slightly off center, although this would hardly be discovered by a casual observer. Superposing mirror loop displacements has little effect in this case as is evident

in Figs. 33c and d which represent the same situation as Fig. 33b. The mirror loop displacements should in this case be applied to the whole crystal and not only to the part above the loop. The latter procedure will create an unnatural discontinuity of displacement at the plane of the loop which shows up as a step of the central ring in Fig. 33c. In Fig. 33d the mirror loop displacements are superposed to the whole crystal and the step in the ring is gone. On the (113) plane this makes no difference since the mirror loop, when the loop is all inside the surface, is too far from the lower part of the crystal to affect it anyway (see Fig. 17).

A corresponding sequence of plots for an interstitial loop under $(11\bar{1})$ is shown in Fig. 34. As was the case under (113), the contrast is again different from that of the vacancy loop. The effect of the mirror loop displacements seems to be a little stronger in this case. Figure 34f is the same as Fig. 34c and Fig. 34e the same as Fig. 34b, only with the mirror loop added. In Fig. 34d the mirror loop displacements are added only to the upper part of the crystal and the resulting step in the central ring is evident.

The position of point H of Fig. 30 is not marked on the $(11\bar{1})$ plane. In Fig. 33a for instance, H would be 34 (111) planes above the loop. Hence, besides being outside the plot, its position would be of no interest.

The contrast effect discussed here is, of course, not limited to the central ring of a pole. It, as well as most other contrast effects, is simply easiest to observe there. Figure 35 shows the resulting contrast when a loop is positioned somewhat farther away from the pole.

In Fig. 35a and b the interstitial loop is bending the third and fourth (113) rings inward, whereas a vacancy loop in the same position causes bulging of the second and third rings in Fig. 35c and of the second, third and fourth rings in Fig. 35d. Hence the effect is the same as on the central ring in the previous plots. Figures 35a and b are different stages of a simulated field evaporation sequence, as are Figs. 35c and d.

The contrast effects in many of the plots in this section are admittedly too weak to be of practical importance, notably the plots in Figs. 31a, 32a, 33a-d and 34a and b. The object of this section was to indicate the existence of contrast from loops wholly inside the tip. Since it would be of interest to know at what distance between loop and surface the contrast begins to show, cases were deliberately chosen where the loop was at approximately this critical distance from the surface. When the loop approaches the surfaces the effect becomes clearly noticeable, as is evident for loops under (113) in Figs. 31 and 32. For the $(11\bar{1})$ plane some plots will be shown later (Fig. 43) where the loop is closer to the surface, and the effect stronger.

This effect is, of course, not restricted to the (113) and $(11\bar{1})$ planes. These were chosen because one makes a small and the other a large angle with (111). The effect of the angle is not of qualitative significance as far as the contrast is concerned. The anticipated result that the contrast shows up when the loop is at a greater depth beneath the surface if the angle is small, is clearly arrived at. This is somewhat misleading, however, since it depends on how the distance from

the surface is defined. Considering, instead of D, the distance of the center of the loop from the surface along the surface normal (D sin ϕ), would give a somewhat different picture, although the result would still stand.

4. Difference in Contrast between Vacancy and Interstitial Loops

To investigate the possibility of distinguishing between vacancy and interstitial loops by inspection of ion micrographs, both kinds of loops were placed in the same position in a tip and the contrast simulated. Again only configurations under the (113) and (11$\bar{1}$) planes will be presented for the same reason as before, i.e. to have one case where the angle between loop plane and surface is small and one where it is large.

Figures 36, 37 and 38 show the contrast from loops beneath the lower side of (113), i.e. the side further away from the (111) pole. The contrast is first seen to be essentially the same whether the loop is all inside the tip (Fig. 36), or is cut by the surface (Figs. 37 and 38). The difference between vacancy and interstitial loops is clear. The vacancy loop tends to elongate the central ring towards the loop, whereas the effect of the interstitial loop is a shrinking of the central ring away from the loop. As pointed out in the preceding section, this difference is present as soon as the loop is close enough to the surface to show contrast at all.

In a few stages of field evaporation the contrast may be characterized as a stepped spiral as is evident in Figs. 37c and d, 38a and possibly 38b. In these cases the sense of the spiral is as it should be, i.e. anti-clockwise for the vacancy loop and clockwise for the interstitial

loop. It is not possible, however, to infer the value of q from the stepped spiral, since the loop intersects only one plane edge at a time. Hence this is a case where the $\vec{g}\cdot\vec{b}$ criterion would be useless.

Figures 39 and 40 show that the qualitative features of the contrast remain the same when the loops are moved to the upper part of the pole. Especially the difference between vacancy and interstitial loops is still evident. In Fig. 39 the loops are wholly inside the tip, and in Fig. 40 they are intersected by the surface. The strong bending of the second ring in Figs. 40a and b can be understood if one remembers that q is 5/3 in this case.

The significance of the fact that the contrast is the same for loops on either side of the pole is most easily realized by considering loops under a plane, say (110), where there are two {111} planes in equivalent positions, i.e. (111) and $(11\bar{1})$ (see Fig. 41). The other two are perpendicular to (110). Because of the symmetry of this configuration a loop on (111) on one side of the pole is equivalent to a loop of the same kind on $(11\bar{1})$ on the other side of the pole. According to the preceding paragraph, however, a loop on (111) would cause the same type of contrast on either side of the pole. Hence the nature of the loop can be inferred unambiguously from the type of contrast observed regardless of the plane of the loop. It will be remembered that the intuitive theory predicts the same contrast from a vacancy loop on (111) and an interstitial loop on (111) under (110), i.e. a determination of the plane of the loop must be made before the nature of the loop can be deduced.

Figures 42 and 43 indicate that these results are equally valid on the $(11\bar{1})$ pole, i.e. in a case where the angle between loop plane and surface is large. Figure 41 shows two simulated field evaporation sequences, one through a vacancy loop (a, c and e) and the other through an interstitial loop (b, d and f), with the loops above the pole. In Fig. 42 the loops are below the pole and all inside the tip. The different contrast for the vacancy and interstitial loop respectively is again evident. Hence this result is quite general and does not depend, qualitatively at least, on the angle between loop plane and surface.

In Fig. 44 two stages of field evaporation each for an interstitial loop (a and b) and a vacancy loop (c and d) are shown. Here the contrast is rather similar in the two cases and an obvious determination of the nature of the loops would not be possible. This is no reason for concern, however. These plots are included here simply to make the point that conclusions about the nature of defects should not be based on single micrographs, but rather on finely stepped field evaporation sequences.

5. Size of Loops

Determination of the size of dislocation loops is little discussed in the literature. The general procedure seems to be to consider the starting and finishing points of the image spiral the points of emergence of the boundary dislocations. The distance between these points is then taken as an estimate of the diameter of the loop. By computer simulating the contrast of three previously intuitively analyzed loops Brandon and Perry[26] indicated that the intuitive method

tends to overestimate the loop size by about 20%. The method of Brandon and Perry consisted of varying the parameters of the computer model, especially the loop radius, until satisfactory agreement between simulated and actual contrast was obtained. As long as this method is based on a single micrograph of each defect it is not quite satisfactory. One should, on the other hand, be able to do rather well using only micrographs, if a fine enough evaporation sequence is obtained. This will be illustrated below with the aid of computer plots.

Figure 45 shows four close stages of a simulated field evaporation sequence of a tip containing an interstitial loop under (110). The plots display the correct spiral structure according to the $\vec{g}\cdot\vec{b}$ criterion ($q = 4/3$ in this case), especially Fig. 45a. It is obvious that the central ring is sweeping across the right edge of the loop during this sequence. It is clearly open, or spiralling, in Fig. 45a and completely closed in Fig. 45d. The position of the right side partial is determined from a comparison of Figs. 45b and c and marked with an A. A similar consideration reveals the left edge of the loop. There is a weak indication of a break in the third ring in Fig. 45b, and in Figs. 45c and d this break becomes apparent. Based on Figs. 45a and d the position of the left partial is determined to be as marked with a B. The positions A and B have been transferred to Fig. 45a by superposing the plots, and marked as A' and B'. This can, in this case, be done exactly since the evaporation stages are so close that many image points are common to the plots. The actual position of the loop was afterwards marked onto Fig. 45b. In this case the determination is almost exact as a comparison of markings of Fig. 45a and b indicates.

It should be pointed out here that if Fig. 45d alone is chosen for analysis and the starting point of the spiral, i.e. the upper end of the second ring, is taken as the position of the right partial dislocation, the diameter of the loop would be underestimated by about 40%. If, on the other hand, field evaporation is continued beyond the stage of Fig. 45d so that the central plane disappears, there would be no way of telling the position of the right partial. Actually this situation is approximately at hand in Fig. 45a. The only thing obvious in Fig. 45a is that there is a stacking fault running from approximately B' towards the center of the pole. It could not go beyond B' to the left since the third ring is not stepped as the inner two are. There is no clue in Fig. 45a, however, that the stacking fault ends at A'. Rather it would appear to pass under the starting point of the spiral, and could run almost over to the right side of the innermost ring. Hence the loop diameter would be uncertain to about 50%.

An otherwise identical case with a smaller loop is illustrated in Fig. 46. This loop is too small to cross more than one plane edge at a time (in this position). During the evaporation sequence of Fig. 46 one plane edge, the second ring in Fig. 46a, sweeps over the loop. There is a kink in the innermost ring in Fig. 46a, marked with an arrow and the letter A, and there appears to be a kink in the second ring across the ledge from A. In Figs. 46b and c the second ring is breaking and the left edge of the loop is marked with a B based on this. Figure 46d is included only to make the sequence easier to follow indicating how the central ring is shrinking. There is also a gap in the second ring

in this plot. In Fig. 46e the central ring has disappeared, whereas the gap in what is now the first ring remains. In Fig. 46f the first ring is closed and taking this to indicate that this ring has passed the right edge of the loop, the position marked C in Fig. 46e results for the right partial. The point C is indicated in Fig. 46b as C' and B of the latter figure is indicated in Fig. 46e as B'. The actual loop position is marked in Fig. 46f, and it is obvious that the estimation in this case is about 20% too large. It should be pointed out here that the procedure outlined above with respect to Fig. 46 relies strongly upon the knowledge that the loop is there. The contrast in Fig. 46 due to the loop is probably too small to be discovered in practice. If, however, the breaking of a ring as it sweeps over a loop is observable, this, of course, is a possible method of measuring the loop size.

It should also be noticed that the distance of the loop from the surface is 0.539 in Fig. 46a and 0.064 in Fig. 46f. This means that the width of the loop at its intersection with the surface has increased from 4 atoms to 5 atoms during the simulated field evaporation sequence. Although this is quite meaningless for such a small loop, it is important in principle and is clearly an aspect automatically neglected when loops are simulated as dipoles.

IV. COMPARISON WITH EXPERIMENTAL OBSERVATIONS

A. Experimental Facilities and Methods

The ion microscopy was performed in an atom probe field ion microscope,[40,41] although the atom probe capability was not used in this study. The microscope utilizes a 80 ℓ/S ion pump and a titanium getter as its main vacuum system. A liquid nitrogen trapped oil diffusion pump was used to remove the imaging gas. A background vacuum of one to five nTorr was usually obtained with this pumping system.

The specimen holder is sketched in Fig. 47. A hollow copper cylinder acts as a cold finger. An alumina rod is precision fitted into the cylinder to act as an electrical insulator. The tip is spot welded to a tungsten hairpin which is mounted in a small copper block cold pressed into the alumina rod. The copper cylinder was cooled by passing cold helium gas, boiled off a liquid helium dewar, through it. The temperature of the cylinder was monitored during experiments with an Au + 0.7% Fe versus chromel thermocouple. The specimen holder is mounted on a tilt stage which allows it to be rotated around two mutually perpendicular axes passing through the tip. The helium transfer line ends in a stainless steel bellows for the necessary flexibility.

Field ion tips of iridium were prepared by electropolishing in an aqueous solution of $CaCl_2$. The starting material had a nominal purity of 99.5% with a resistivity ratio ($R_{273°}/R_{4.2°}$) of 2.6. After annealing the wires for 15 hours at 1500°C in a vacuum of 10 nTorr the resistivity ratio increased to 26 which still indicates an 0.2 atomic percent impurity level, using the results of Schultz[42] as a rough guide.

The iridium tips were bombarded in situ with 30 kV argon ions from an ion gun assembled specifically for this purpose. The direction of bombardment was along the axis of the tip, made possible by the rotatable specimen holder. The ion beam enters the microscope through a one meter long tube with orifices of 2 mm at both ends. The latter act both as a beam collimator and as crude differential vacuum barriers. Between experiments the tube is sealed off from both the microscope and the ion gun with valves and evacuated by a 8 ℓ/S ion pump. Ion bombardments were performed with the imaging voltage switched off. Typical bombardment times were about five seconds, during which time the pressure in the microscope chamber rose to about 15 nTorr. Hence contamination of the tip should have been minimal. The temperature of the specimen holder (copper cylinder) was maintained at 10-12°K during bombardment. The tip temperature has not been measured but is expected to be a few degrees higher, due mainly to possible bad thermal contact between the alumina rod and the copper block supporting the tip (Fig. 47).

After bombardment the tips were examined at about 15°K (copper block temperature) by pulsed field evaporation; i.e. field evaporation was effected by superposing a high voltage pulse on the image voltage. Evaporation sequences were recorded by taking a picture between each pulse using a 35 mm Nikon F2 camera with motor drive and a 250 exposure film casette. A channel plate image intensifier was used to permit high speed photography. The film was processed at facilities within the laboratory which were developed to process spark chamber film.

For the latter purpose the processing was designed to enhance the contrast of the film as much as possible, which is rather contrary to the needs of ion micrographs. The quality of the micrographs suffered from this but great savings in time and especially cost were achieved.

B. Examples of Possible Frank Loop Contrast

In this section some micrographs, obtained in the manner described in the preceding section, will be presented as examples of the type of contrast predicted by the computer simulations. Figures 48 and 49 show a few frames of a rather long evaporation sequence displaying a fault under (113). This is one of the clear cases of dislocation loop contrast referred to in the introduction. The micrographs in Fig. 48 show the appearance of the fault just after it became visible. The off-center position of the central ring in Fig. 48a, as well as the kink in the central ring in Fig. 48b, c and d are all clearly similar to the features obtained for interstitial loop contrast by computer simulation. Figure 49 shows a later stage of this evaporation sequence during which the contrast in one frame (49g) is a complete spiral. During removal of each of the following three planes after the stage in Fig. 49h a complete spiral recurs. The contrast in Fig. 49g indicates that $\vec{g}\cdot\vec{b} = 1$ for this loop. If the loop is a Frank loop it would then be either $\frac{a}{3}(\bar{1}11)$ or $\frac{a}{3}(1\bar{1}1)$. The trace of $(1\bar{1}1)$ on (113) is $[12\bar{1}]$ and that of $(1\bar{1}1)$ is $[21\bar{1}]$. These are marked with arrows in Fig. 49c. Determining the trace of the loop is not quite so simple as one might think. If the spiral of the central ring is taken to begin on the stacking fault in Fig. 49c and f, however, the trace of the

fault must be $[12\bar{1}]$ rather than $[21\bar{1}]$. This conclusion is further supported by Figs. 49b and e in which the second ring is beginning to bend to the left of the pole (at the arrows). The loop plane is hence $(\bar{1}11)$ which is slanted down to the left in the micrographs. The rules of the intuitive theory can now be applied to determine the nature of the loop. It is clearly an interstitial loop since the spiral structure indicates that the part to the left of the fault has been pushed out of the crystal. It should be noticed that this conclusion depends entirely on a correct determination of the loop plane which appears somewhat uncertain, especially if a fine enough evaporation sequence is not available. If the loop plane were $(1\bar{1}1)$ the loop would be intrinsic. Based on the computer plots of part III, on the other hand, the nature of the loop is obvious already in Fig. 48.

The size of the loop can be estimated in Fig. 49 by the method discussed in section III.5 (Fig. 45). In Fig. 49f the second ring is about to break, and this ring should then be passing just outside the loop. In Fig. 49g the second ring has broken away and joined the first to form a continuous spiral indicating that the second ring of Fig. 49f has swept over the bounding partial dislocation going from Fig. 49f to g. Thus the upper edge of the loop can be pinned down rather accurately. The lower edge is not quite clearly defined in this sequence, however. The splitting up of the spiral in Fig. 49h is somewhat surprising. It may indicate that the central ring is about to close below the loop, in which case the loop would be approximately as marked in Fig. 49h. The width of the first ring in Fig. 49e is roughly 14a (tip radius $\simeq$ 90a) and the

loop, as marked is about half of that, or 7a. In iridium this would be about 28 Å. It should be noticed that the end of the spiral in Fig. 49g is quite far from the partial, and also that any one of these micrographs taken alone would be quite useless. In fact an even finer evaporation sequence would be desirable. The loop was visible over 11 (113) planes which gives an upper limit to its size in the direction into the tip, along $(\bar{1}11)$, of about 7a also.

Figure 50 shows an evaporation sequence of a (113) pole which displays the typical contrast of a small interstitial loop (see Figs. 38 and 39). Between Figs. 50a and r eight (113) planes have been removed. Eight (113) planes correspond to about 10 Å. To deduce the size of the loop from this information one must know the plane of the loop. If it is (111) then the size of the loop is, at most, $10\ Å/\sin 29.5° \cong 20$ Å. The bending of the first or second ring, as well as the off center position of the first ring, occur consistently on each plane. This loop is too small to intersect more than one ring at a time which limits its size to less than 20 Å.

A similar case on a (110) plane is shown in Fig. 51. Here seven (110) planes ($\simeq 7$ Å, or 12 Å along (111)) have been removed during the evaporation sequence. The contrast is again consistent on each plane and clearly that of an interstitial loop.

V. DISCUSSION

There should be little doubt about the results of the computer simulation in this investigation. Taking the plots at face value all conclusions drawn from them follow clearly and unambiguously. The issue is hence not the interpretation of the plots but rather the reliability of the model, or models, producing the plots.

The shell model has proven capable of correctly predicting the qualitative features of the images of faulted crystals. As mentioned in Part II there are enough experimental observations of single dislocation contrast to make this claim undisputed. The qualitative features of the dislocation contrast depend on the long range strain field of dislocations rather than on the atomic configuration at the dislocation core. The main conclusions drawn here, namely that Frank loops cause contrast while completely inside the tip and that vacancy and interstitial loops display qualitatively different contrast, also depend on the long range strain field and in this respect the results seem to be on solid ground. Some problems with the shell model are apparent in the computer plots, however. In some cases involving a vacancy loop wholly beneath the surface the central ring displays a gap as it stretches around the depression in the surface (see e.g. Figs. 36b and 39d). This does not appear intuitively reasonable. One would rather expect the ring to be closed, although possibly imaging at a lower intensity where the simulated ring is open. Another problem is the frequent occurrence of spurious image spots in the plots, especially close to the point of emergence of dislocations (see e.g. Figs. 38c

and [42c]). Both problems have the same origin, i.e. the rigidity of the shell. Lattice points are either within the shell or not, and the environment or coordination of the corresponding atoms is not considered. Especially some of the spurious image spots might be eliminated by using atomic coordination as an additional imaging criterion. Besides the principal difficulty of defining coordination in a heavily strained part of a crystal, this addition would increase the computational labor significantly. In any event it does not appear fruitful to add sophistication to the model at present. Rather the effort should be on experimental observations and only if these show the simple model to be lacking should improvements be contemplated.

The displacement field of Frank loops according to Eq. (III.1) is based on linear isotropic elasticity theory. Sanwald and Hren[25] claim to have made some computer simulations of dislocation contrast using anisotropic elasticity noticing no difference from results based on isotropic elasticity. If this is the case it is fortunate indeed since the anisotropic displacement equations are exceedingly complicated. Equation (III.1) is strictly not valid closer to the dislocation line than about five atomic diameters. Again it should be noticed that the main conclusions of this investigation are not based on displacements close to the dislocations, and hence they should be valid. Some other aspects of the simulated contrast may however be questionable because of this. The discussion of loop size in connection with Fig. for instance relies heavily upon the breaking of image rings close to the dislocations. Although the theory is not strictly valid in this region the displacements given by Eq. (III.1) may still be rather

good approximations. Since no arguments have been based on actual atomic configurations in the plots the restricted validity of Eq. (III.1) should not be of great significance in this context.

Taking surface relaxation into account by superposition of mirror loop displacements is, as was pointed out previously, by no means analytically rigorous. This procedure is believed to be realistic, however, at least in the sense that its effect is in the right direction, i.e. it enhances the depression and bulging of the surface caused by vacancy and interstitial loops respectively. The results of this investigation are not dependent on surface relaxation, i.e. they are valid whether relaxation is taken into account or not. It is especially reassuring, however, that, for instance, the contrast from loops totally inside the tip could be demonstrated without the use of the mirror loop since the effect of the mirror loop was intuitively expected to enhance this contrast.

The model then appears to be sound as far as qualitative geometrical features of the image contrast are concerned. The model is furthermore simple and flexible enough to permit refinements when the need arises in the form of more and better observations.

Although the computer simulation predicts a clear qualitative difference between the contrast from vacancy and interstitial loops the situation is not nearly so favorable as this fact implies. The first point to be made in this context is quite obvious but it appears necessary to state it explicitly nevertheless: Examining a computer plot for the contrast due to a precisely known defect configuration is

a matter entirely different from trying to deduce the defect configuration responsible for an observed contrast effect. In the former case there is a clear one to one relationship; changing the defect configuration will change the simulated contrast and the change in contrast can always be related to the change in configuration since the latter is precisely known. Examining a micrograph, however, one is faced with numerous possibilities. For instance, before a distinction between a vacancy and an interstitial loop becomes meaningful one needs to know whether a particular contrast effect is caused by a Frank loop at all.

The contrast effects peculiar to Frank loops are clearly due to the strong transverse strain field of these loops. It appears quite obvious, however, that all prismatic loops will cause similar contrast. Hence a distinction between perfect prismatic loops and Frank loops can only be made based on the $\vec{g}\cdot\vec{b}$ criterion which is of limited usefulness for small loops, and not always unambiguous. The contrast of Fig. 49 is a case in point. It was discussed in terms of an $\frac{a}{3}[\bar{1}11]$ Frank loop. Since $\vec{g}\cdot\vec{b}$ was found to be equal to one, i.e. integral, in this case, the contrast could be caused by a perfect loop on $(\bar{1}11)$ with Burgers vector $\frac{a}{2}[\bar{1}01]$. All glissile loops, in the case that they are not swept out of the tip, by the field induced stress would be expected to cause rather different contrast from psismatic loops.

Considering small Frank loops especially, the fact that their strain field causes the contrast leads to some further consideration. In the limit of very small loops the strain field would be essentially radial, especially at some distance from the loop. Hence one would expect the same type of contrast from any defect clusters with strong

strain field, say a cluster of interstitials not in the shape of a disc, or a cluster of impurity atoms. While such a cluster is beneath the surface of a field ion tip it would cause the same type of contrast as a loop beneath the surface. The difference would, however, be expected to become apparent when the surface gets close to the cluster, or intersects it, in which case the cluster itself would appear as a number of bright spots or possibly one very large bright spot.

There is an interesting difference between vacancies and interstitials in this respect. A small disc of vacancies, say the vacancies of a 5 atom loop as defined here, need not necessarily cause the surrounding crystal to collapse thus forming a dislocation loop. If the crystal does not collapse there will be no, or a very weak, strain field, and the configuration would be virtually invisible in the ion microscope. This possibility is at hand more strongly for spherical vacancy clusters. Interstitials, on the other hand, will cause strain in any configuration. This difference, in fact, exists already for single interstitials and vacancies. This feature may explain the fact that only interstitial type contrast has been observed so far in the ion bombarded tips referred to in Part IV. There may in fact be small vacancy clusters as well, but uncollapsed, so that no strain field is created.

The strain field will obviously also affect the estimation of the size of loops. Since the strain field will cause contrast before the loop intersects the surface it is not correct to simply count the number of planes on which the contrast is visible and take the thickness of the removed material as the projection of the width of the loop on

the image plane normal. The actual breakthrough of the loop to the surface appears, unfortunately, not to be a spectacular event, i.e. the contrast looks much the same before and after the surface cuts into the loop. In Figs. 50 and 51 for instance the contrast does not change much during the evaporation sequence. It is doubtful if the computer model can help much with this problem. The breaking through of the loop to the surface was discussed to some length in Part III in describing the model (see Fig. 19). It appears that this is a situation where distinctions need to be based on actual atomic configurations close to a dislocation which is outside the capability of the computer model at present.

The stress field in the tip due to the electrical field has so far not been mentioned at all. At best imaging voltage this stress is about $G/10^{35}$ where G is the shear modulus. This is close to the theoretical shear stress. The hydrostatic component of the stress corresponds to a 3% expansion of the lattice. The stress distribution in the tip has not been determined, but it is clear that rather strong shear stresses must be present in regions of the tip. Shear stresses would, of course, distort the strain field of a dislocation loop and hence its image. The fact that dislocation images in excellent agreement with geometrically predicted ones have been observed seems to indicate, on the other hand, that the stress field in some regions of the tip is essentially hydrostatic. A hydrostatic stress field would merely expand the lattice radially and not distort dislocation configurations. The stress field is probably closest to hydrostatic in the central regions of the tip which would be a good reason to confine observations to these regions.

The need for experimental work based on finely stepped evaporation sequences should be emphasized again. Ideally one would want to be able to introduce specific defect configurations in well defined positions into field ion tips, as one can in the computer model. The best system available for study would probably be annealed and quenched specimens, which would be known to contain defects of vacancy type. The micrographs presented in Figs. 48-51 were obtained from tips bombarded and examined at a low temperature (< 20°K). Since the formation of dislocation loops of either kind under these conditions is somewhat surprising these micrographs are presented here merely to indicate the plausibility of the simulated contrast effects. The similarity between the contrast of the micrographs and that of the computer plots cannot be denied.

VI. SUMMARY AND CONCLUSIONS

The contrast due to small Frank dislocation loops in field ion tips was analyzed by computer simulation. The simulation of the image was based on the shell model and the displacement field of the dislocation loops was computed using the exact displacement equation for a closed dislocation loop in an isotropically elastic continuum (Burgers' formula). A simple method for taking the effect of surface relaxation on the displacement field into account was introduced. The method consists of superposing the displacement field of an image loop located in the mirror position of the real loop relative to the surface. Simulated field evaporation sequences were produced by either increasing the radius of the simulated tip while moving its center of curvature into the tip along its axis, or by simply shrinking the simulated surface concentrically. The following conclusions were drawn from this investigation:

1. Frank loops will cause image contrast not only when they intersect the tip surface but when they are wholly inside the tip as well.
2. Frank loops of vacancy and interstitial type cause qualitative different contrast, recognizable on inspection, and rather independent of loop plane and position.
3. Taking surface relaxation into account only enhances all analyzed contrast effects but does not alter them qualitatively.
4. Analysis of lattice defects by ion microscopy should be based on extensive and finely stepped evaporation sequences and absolutely not on single micrographs. This applies both to the characterization of the nature of a defect and to the determination of its size.

5. Determining the size of a Frank loop from its image contrast is very difficult, even using an evaporation sequence, since the contrast is caused by the strain field of the loop which is larger than the loop.
6. Comparison with experimental observations indicated the plausibility of the simulated contrast.

ACKNOWLEDGEMENTS

I want to thank my wife for loving care over the years, and for her help in preparing the thesis.

I am grateful to Professor Washburn for his patient support and his understanding of my problems. I have also, no doubt, benefitted greatly from his critical attitude.

I am indebted to Professor Parker for his positive outlook and encouragement during some of my darker moments.

While thanking the whole support staff of IMRD for creating a pleasant working atmosphere, I want especially to mention Walter Toutolmin, who built most of the equipment, Jim Severns for his efforts in keeping the electronics in working condition, and Glen Baum for help with all those small (and some large) things that really count.

The ion gun was provided by Ken Ehlers together with sound advice on its use.

Shirley Ashley typed and edited the manuscript with great competence and and efficiency. I am grateful for her efforst and for her cheerfulness in spite of the pressure from an approaching dead-line.

The art work was done by Gloria Pelatowski whom I thank for yer interest and cooperation.

This work was done under the auspices of the U. S. Atomic Energy Commission.

REFERENCES

1. A. J. W. Moore, J. Phys. Chem. Solids 23, 907 (1962).
2. E. W. Müller, Z. Physik 156, 399 (1959).
3. A. H. Cottrell, Theory of Crystal Dislocations, (Blackie, London, 1964).
4. D. A. Smith, M. A. Fortes, A. Kelly and B. Ralph, Phil. Mag. 17, 1065 (1968).
5. S. Ranganathan, J. Appl. Phys. 37, 4346 (1966).
6. D. W. Pashley, Rep. Prog. Phys. 28, 291 (1965).
7. M. J. Buerger, Contemporary Crystallography, (McGraw-Hill, 1970).
8. J. P. Hirth and J. Lothe, Theory of Dislocations, (McGraw-Hill, 1968).
9. K. M. Bowkett and D. A. Smith, Field-Ion Microscopy,(North-Holland Publishing Company, 1970).
10. M. A. Fortes, D. A. Smith and B. Ralph, Phil. Mag. 17, 169 (1968).
11. V. T. Son and J. J. Hren, Phil. Mag. 22, 675 (1970).
12. M. A. Fortes, Phil. Mag. 22, 317 (1970).
13. R. C. Sanwald and J. J. Hren, 13th Annual Field Emission Symp. Cornell University (1966).
14. A. J. Perry and D. G. Brandon, Phil. Mag. 16, 119 (1967).
15. A. J. W. Moore and D. G. Brandon, Phil. Mag. 18, 679 (1968).
16. A. J. W. Moore and S. Ranganathan, Phil. Mag. 16, 723 (1967).
17. D. G. Brandon, J. Sci. Instr. 41, 373 (1964).
18. M. A. Fortes, Ph.D. Thesis, Cambridge University (1968).
19. B. Ralph and D. G. Brandon, Phil. Mag. 8, 919 (1963).
20. E. K. Caspary and E. Krautz, Z. Naturforsch. 19a, 593 (1965).
21. A. J. W. Moore, Phil. Mag. 16, 723 (1967).

22. N. V. Raghavan, Ph.D. Thesis, University of California (1967).

23. R. C. Sanwald, S. Ranganathan and J. J. Hren, Appl. Phys. Letters 9, 393 (1966).

24. D. G. Brandon and A. J. Perry, Phil. Mag. 16, 131 (1967).

25. R. C. Sanwald and J. J. Hren, Surface Sci. 9, 257 (1968).

26. D. G. Brandon and A. J. Perry, Surface Sci. 12, 461 (1968).

27. A. J. Perry and D. G. Brandon, Phil. Mag. 17, 255 (1968).

28. A. J. Perry and D. G. Brandon, Phil. Mag. 18, 353 (1968).

29. S. Ranganathan, Phil. Mag. 19, 415 (1969).

30. A. J. Perry and D. G. Brandon, Surf. Sci. 14, 423 (1969).

31. S. Ranganathan, Surf. Sci. 20, 429 (1970).

32. E. W. Müller and T. T. Tsong, Field Ion Microscopy. Principles and Applications. American Elsevier Publishing Company, Inc. New York 1969.

33. D. A. Smith, R. Morgan and B. Ralph, Phil. Mag. 18, 869 (1968).

34. T. F. Page, Ph.D. Thesis, Cambridge University (1970).

35. M. A. Fortes and B. Ralph, Phil. Mag. 18, 787 (1968).

36. M. A. Fortes, Phys. Stat. Sol. (b) 43, 387 (1971).

37. D. A. Smith, T. F. Page and B. Ralph, Phil. Mag. 19, 231 (1969).

38. T. F. Page and B. Ralph, Phil. Mag. 26, 601 (1972).

39. A. Ralston, A First Course in Numerical Analysis, McGraw Hill, N.Y. (1965).

40. K. Stolt, Masters Thesis, UC-Berkeley, UCRL-20303, 1970.

41. K. Stolt, IMRD Annual Report, LBL-425, 1971, p. 86.

42. H. Schultz, Acat Met. 12, 649 (1964).

FIGURE CAPTIONS

Fig. 1. Geometrical image formation of

a) and b) perfect tip

c) and d) tip containing planar fault .

Fig. 2. Geometrical image formation of pole intersected by a dislocation line. (After Ref. 4).

a) perfect stack of planes

b) stack of planes intersected by dislocation

c) effect of field evaporation

d) resulting spiral in ion image .

Fig. 3. Geometrical image formation of pole intersected by dislocation line when $\vec{g}\cdot\vec{b} = 3$. (After Ref. 4).

a) stack of planes intersected by dislocation

b) effect of field evaporation

c) resulting triple spiral in ion image.

Fig. 4. Effect of perfect dislocation loop on stack of planes. (After Ref. 10).

a) both dislocations emerging on same ledge

b) dislocations emerging on different ledges.

Fig. 5. Geometrical image formation of pole cut by stacking fault. (After Ref. 11).

a) intrinsic fault

b) extrinsic fault.

Fig. 6. Geometrical image formation of pole intersected by partial dislocation ($|q| < 1$). (After Ref. 4).

Fig. 6 (cont.) a) stack of planes cut by dislocation

b) resulting image.

Fig. 7. Geometrical image formation of pole intersected by partial dislocation ($1 < |q| < 2$). (After Ref. 4).

a) stack of planes cut by dislocation

b) resulting image.

Fig. 8. Geometrical image formation of faulted dislocation loop emerging in one pole ($|q| < 1$) (After Ref. 4).

a) stack of planes intersected by loop

b) resulting image.

Fig. 9. Geometrical image formation of dissociated perfect dislocation emerging in one pole. (After Ref. 4).

a) stack of planes cut by dissociated dislocation

b) resulting image.

Fig. 10 a) Image of (001) pole intersected by a Frank dislocation loop. The loop is either a vacancy loop on (111) or an interstitial loop on $(11\bar{1})$.

b) Geometry of the situation described in a).

Fig. 11 a) Sketch of the (111) plane crossing the (001) plane with possible Burgers vectors of Shockley type indicated.

b) Relationship between Shockley Burgers vectors and atomic positions on the (111) plane.

Fig. 12. Illustration of how intrinsic and extrinsic stacking faults can be distinguished by measuring the size of half rings (see Text). (After Ref. 12). a) intrinsic fault

b) extrinsic fault.

Fig. 13. Computer simulated ion image showing stereographic triangle of (001) oriented fcc crystal.

Fig. 14 a) Sketch of Fig. 4a from Ref. 11 showing simulated contrast of a tip containing a Frank loop of vacancy type under (022).

b) Corrected version of a).

Fig. 15. Illustration of closed dislocation loop and coordinate system used to derive the displacement field of the loop.

Fig. 16 a) Coordinate system used to calculate displacement field of hexagonal loop.

b) Illustration of "five atom loop".

Fig. 17. Sketch of image loop in mirror position of real loop relative to tip surface, and coordinate system used for mirror loop displacements.

Fig. 18. Sketch of situation when the real loop intersects the surface; mirror loop will be reflected into the tip.

Fig. 19. View of a $(1\bar{1}0)$ plane cutting through a vacancy loop on (111) under (110).

Fig. 20 a) Relationship between change in tip radius (ΔR) and amount of material removed along tip axis (ΔZ). (Ref. 9).

b) Same as a) for region far from tip axis.

Fig. 21. Computer simulated images of stacking faults crossing the $(11\bar{1})$ pole.

a) Intrinsic fault running through crystal

b) Extrinsic fault running through crystal

c) Intrinsic fault ending in center of the pole

d) Extrinsic fault ending in center of the pole.

Fig. 22. As Fig. 21 for (002) pole.

Fig. 23. As Fig. 21 for (113) pole.

Fig. 24. As Fig. 21 for (224) pole.

Fig. 25. Simulated evaporation sequence of a tip containing a vacancy loop under the (110) pole. Only real loop displacements used.

Fig. 26. As Fig. 25 with mirror loop displacements applied to upper part of crystal.

Fig. 27. As Fig. 25 with mirror loop displacements applied to the whole crystal.

Fig. 28. As Fig. 25 with real and mirror loop truncated at surface.

Fig. 29. Short simulated evaporation sequence of a tip containing an interstitial loop under the $(11\bar{1})$ pole using two models.

a) and b) only real loop displacements

c) and d) mirror loop displacements superposed to upper part of crystal.

Fig. 30. Definition of parameters used to localize loops wholly beneath the surface.

Fig. 31. Simulated evaporation sequence of tip containing an interstitial loop under the (113) pole. Loop wholly beneath the surface.

a) - f) only real loop displacements

f) as c) with mirror loop superposed

h) as d) with mirror loop superposed.

Fig. 32. As Fig. 31 with vacancy loop.

a) - d) only real loop displacement

e) as a) with mirror loop superposed

f) as b) with mirror loop superposed.

Fig. 33. Two simulated images of tip containing a vacancy loop under the $(11\bar{1})$ pole. Loop wholly beneath the surface.

a) and b) only real loop displacements

c) as b) with mirror loop displacements superposed to upper part of crystal

d) as b) with mirror loop displacements superposed to whole crystal.

Fig. 34. As Fig. 33 with interstitial loop.

a), b) and c) only real loop displacements

d) as b) with mirror loop displacements superposed to upper part of crystal

e) as b) with mirror loop displacements applied to whole crystal.

f) as c) with mirror loop displacements applied to whole crystal.

Fig. 35. Simulation of Frank loop contrast when the loop is somewhat removed from a pole. Loop wholly beneath the surface.

a) and b) Interstitial loop near (113) pole

c) and d) Vacancy loop near (113) pole.

Fig. 36. a) and b) Simulated contrast of a vacancy loop wholly beneath the surface below the (113) pole.

c) and d) as a) and b) for interstitial loop.

Fig. 37. Simulated evaporation sequence of a tip containing a vacancy loop intersecting the surface below the (113) pole.

Fig. 38. As Fig. 37 for interstitial loop.

Fig. 39. a) and b) Simulated contrast of an interstitial loop wholly beneath the surface above the (113) pole.

Fig. 40. As Fig. 39 with the loops intersecting the surface.

Fig. 41. Sketch of two {111} planes in equivalent position under (110).

Fig. 42. a), c) and e) Simulated evaporation sequence of a tip containing a vacancy loop intersecting the surface above the $(11\bar{1})$ pole
b), d) and f) As a), c) and e) for interstitial loop.

Fig. 43. a) Simulated contrast of a vacancy loop wholly beneath the surface below the $(11\bar{1})$ pole.
b) As a) for an interstitial loop.

Fig. 44. a) and b) Simulated contrast of interstitial loop intersecting the surface above the (113) pole.
c) and d) As a) and b) for vacancy loop.

Fig. 45. Simulated evaporation sequence of a tip containing a thirteen atom interstitial loop intersecting the (110) pole. The sequence illustrates the determination of the size of the loop.

Fig. 46. As Fig. 45 for a five atom loop.

Fig. 47. Sketch of field ion tip holder.

Fig. 48. Evaporation sequence of (113) region of an iridium tip showing possible Frank loop contrast.

Fig. 49. Continuation of Fig. 48 illustrating the determination of loop plane and size.

Fig. 50. Evaporation sequence of (113) region of an iridium tip showing possible Frank loop contrast.

Fig. 51. As Fig. 50 for (110) region.

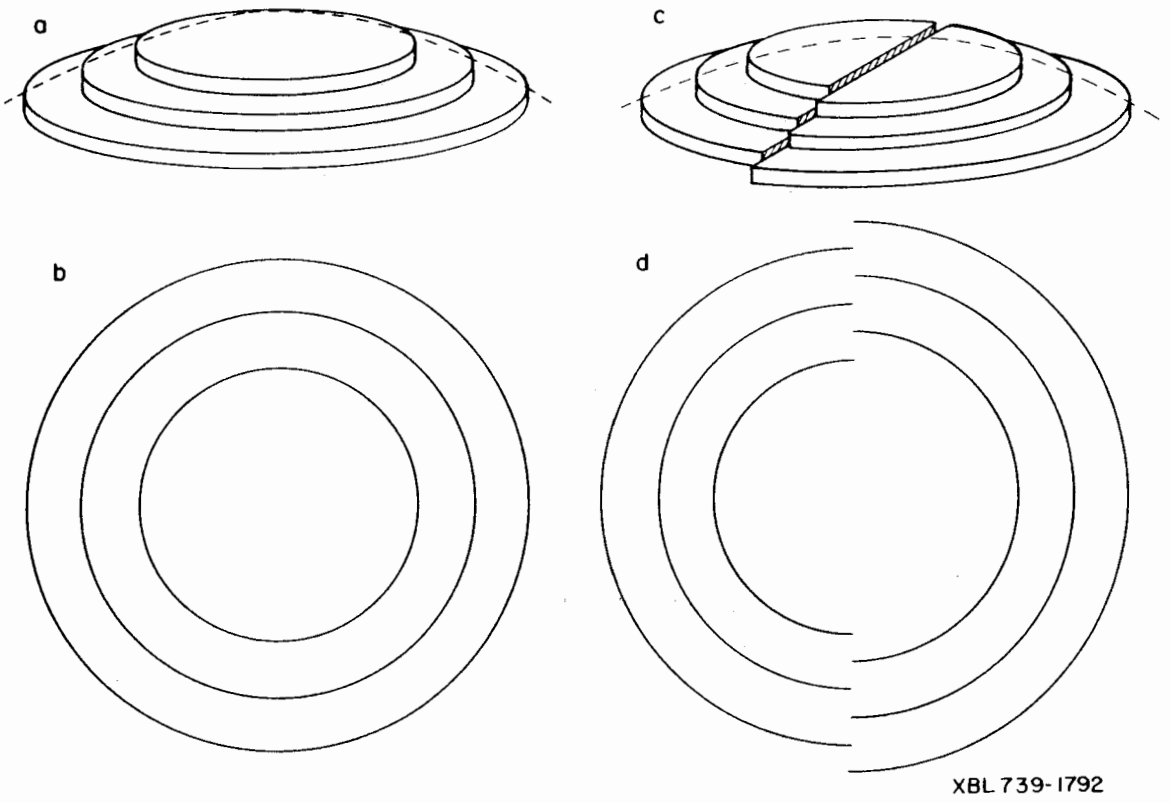


Fig. 1

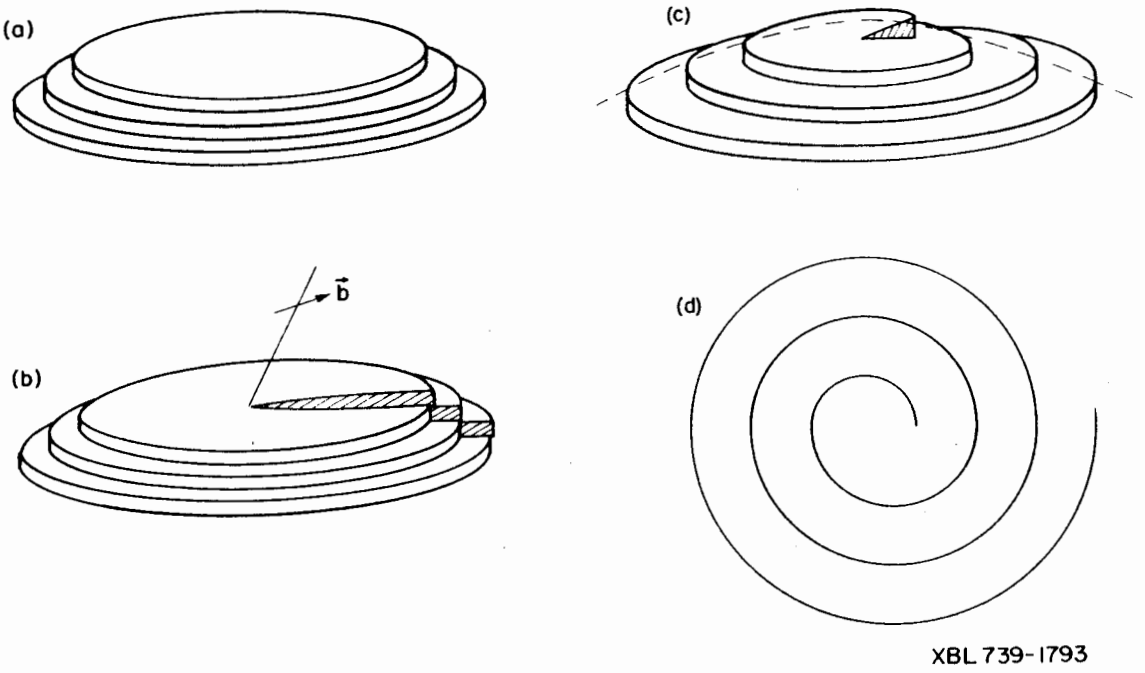


Fig. 2

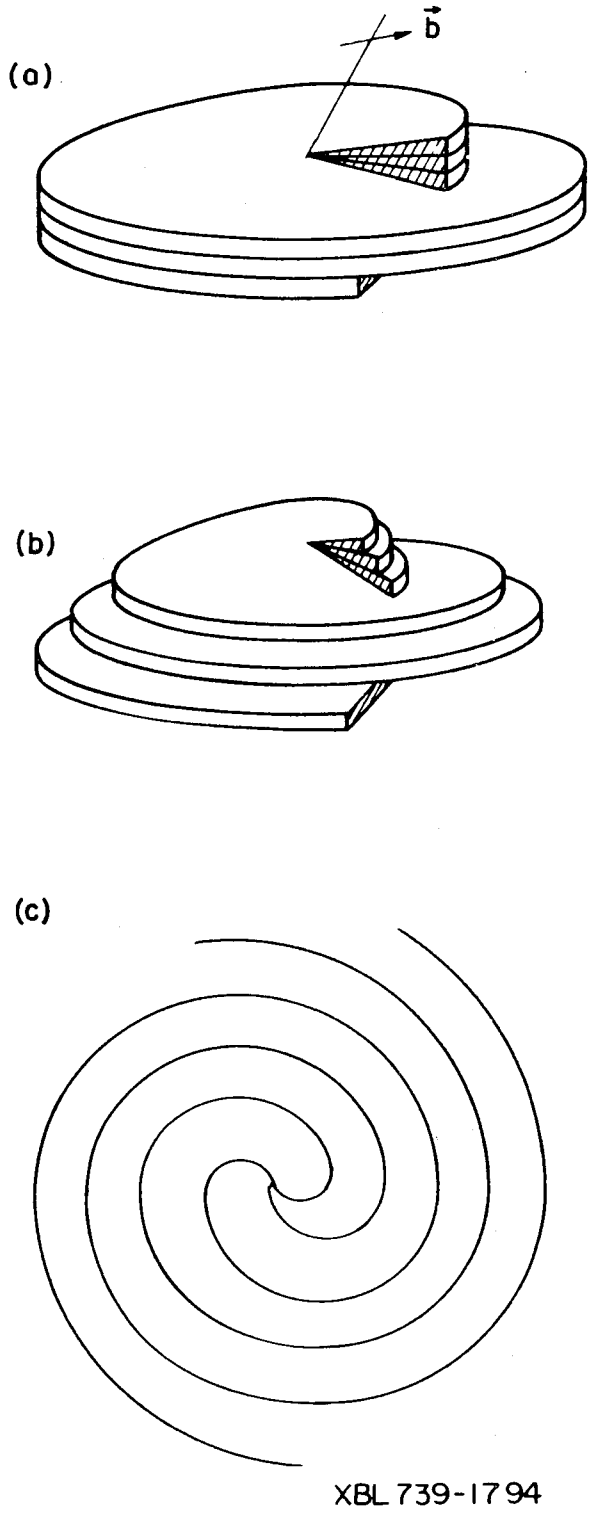


Fig. 3

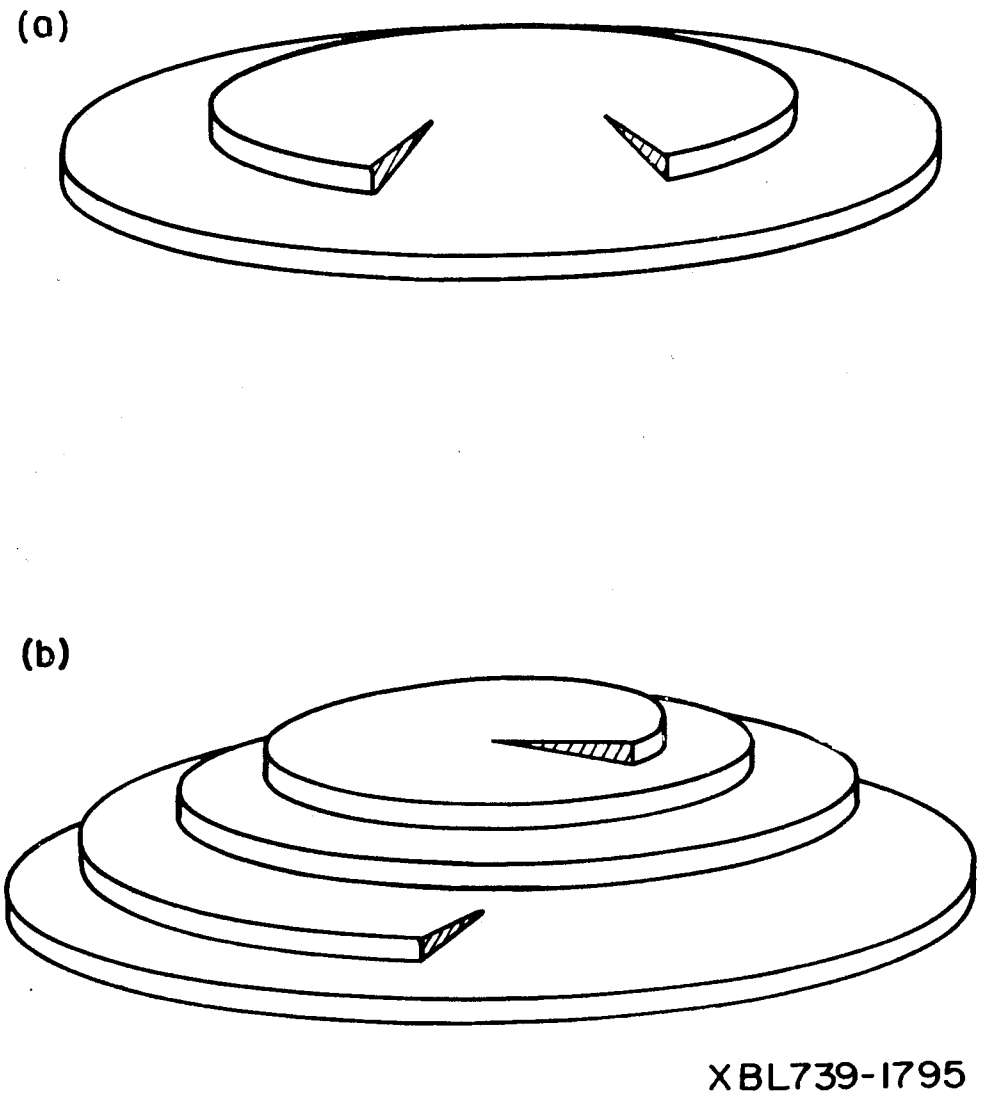


Fig. 4

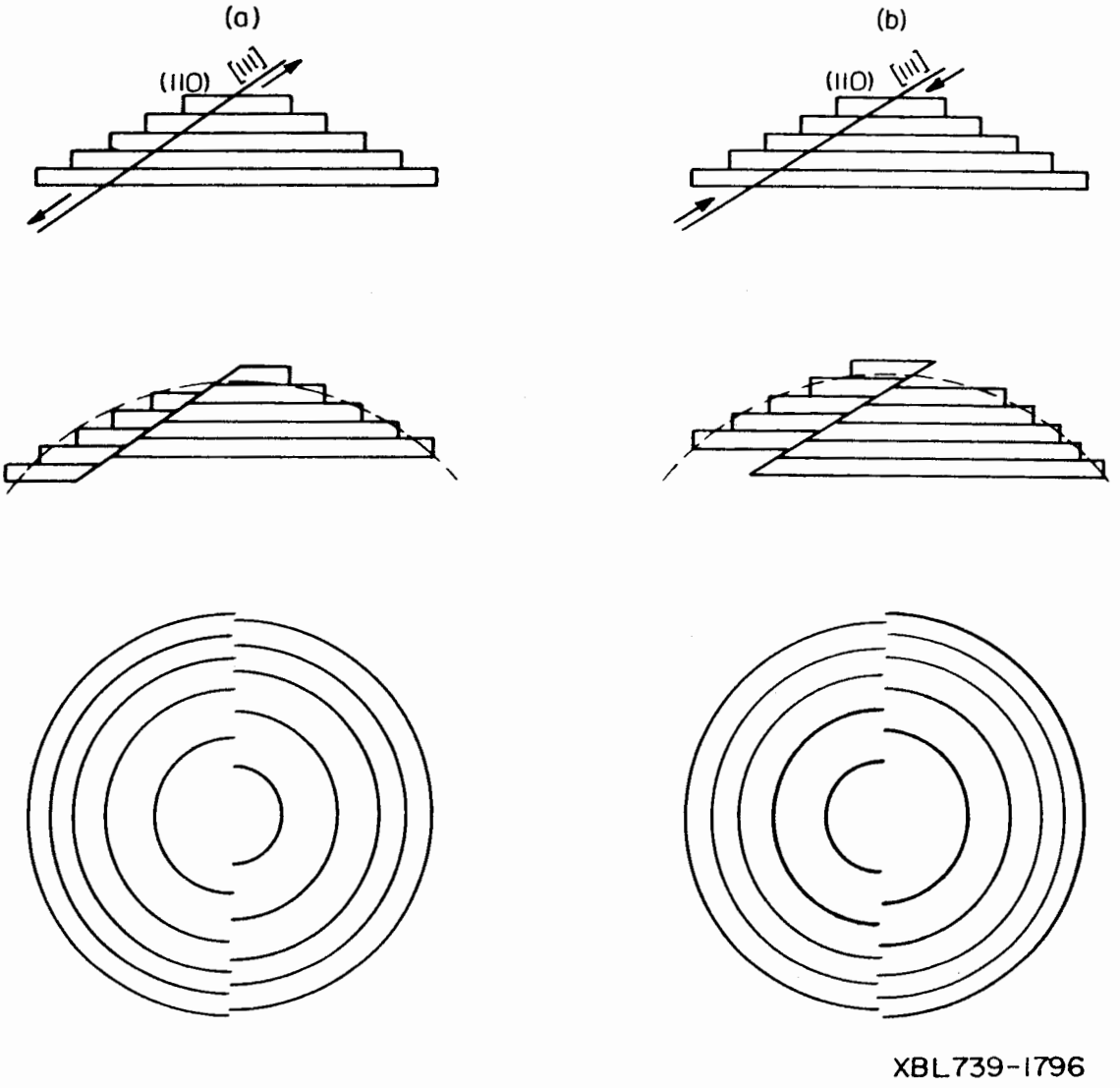


Fig. 5

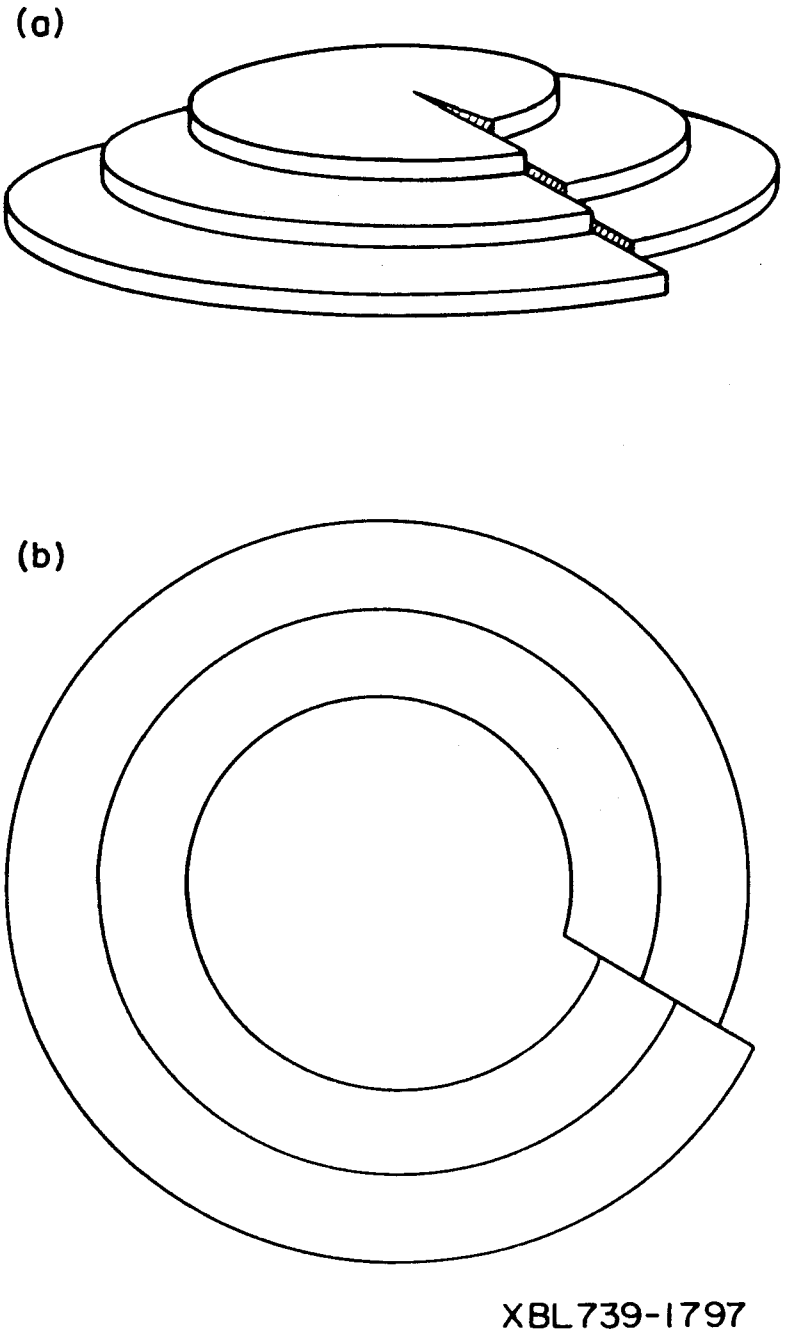


Fig. 6

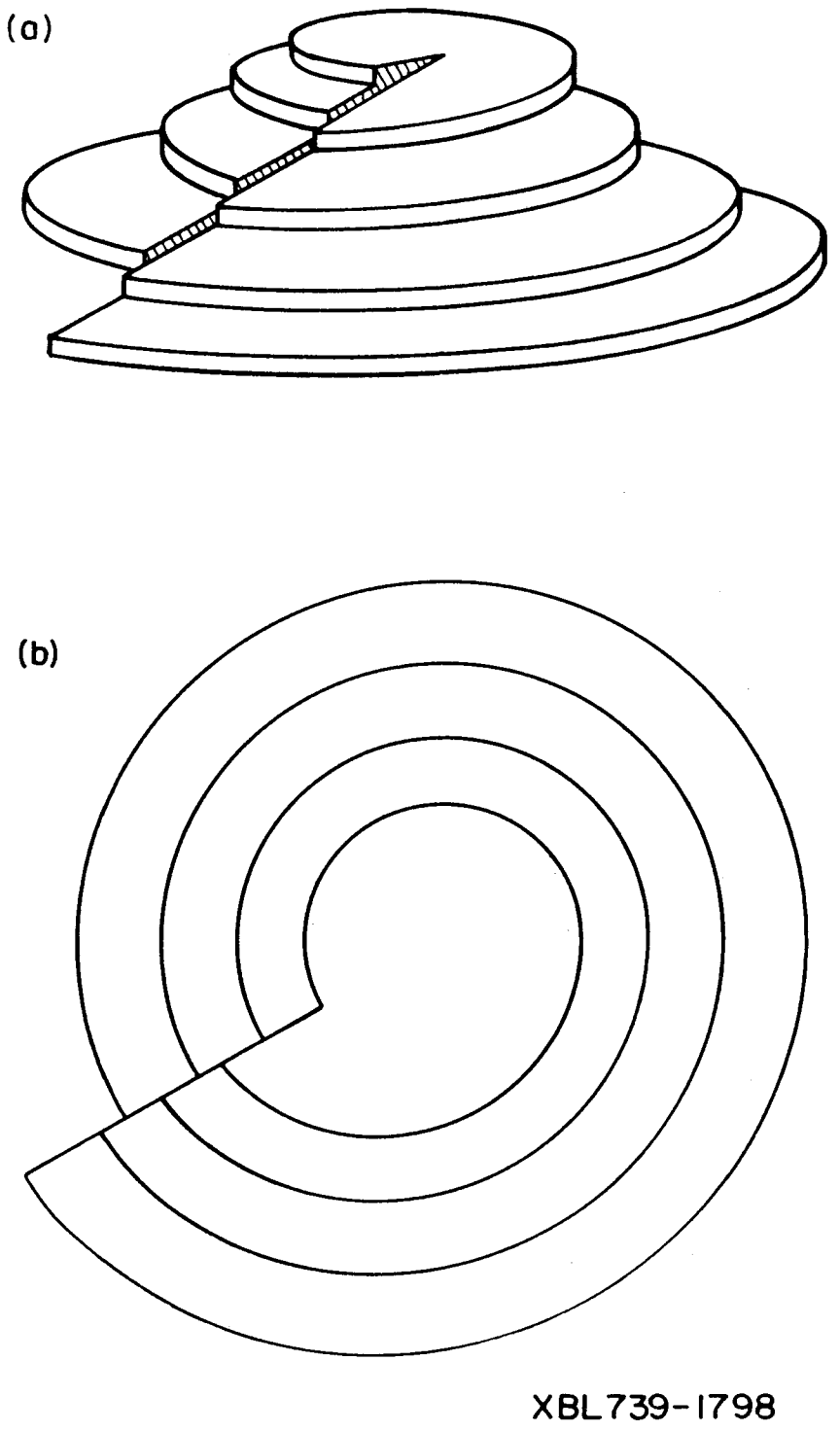


Fig. 7

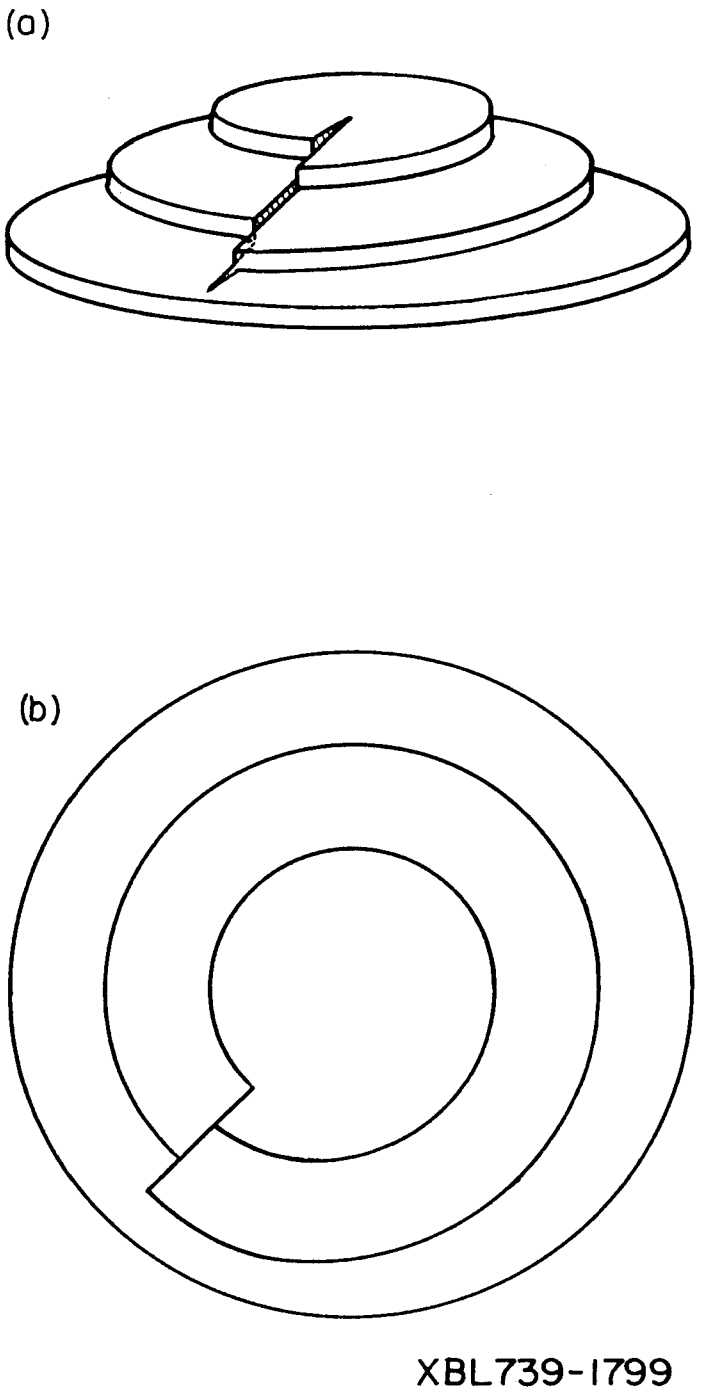


Fig. 8

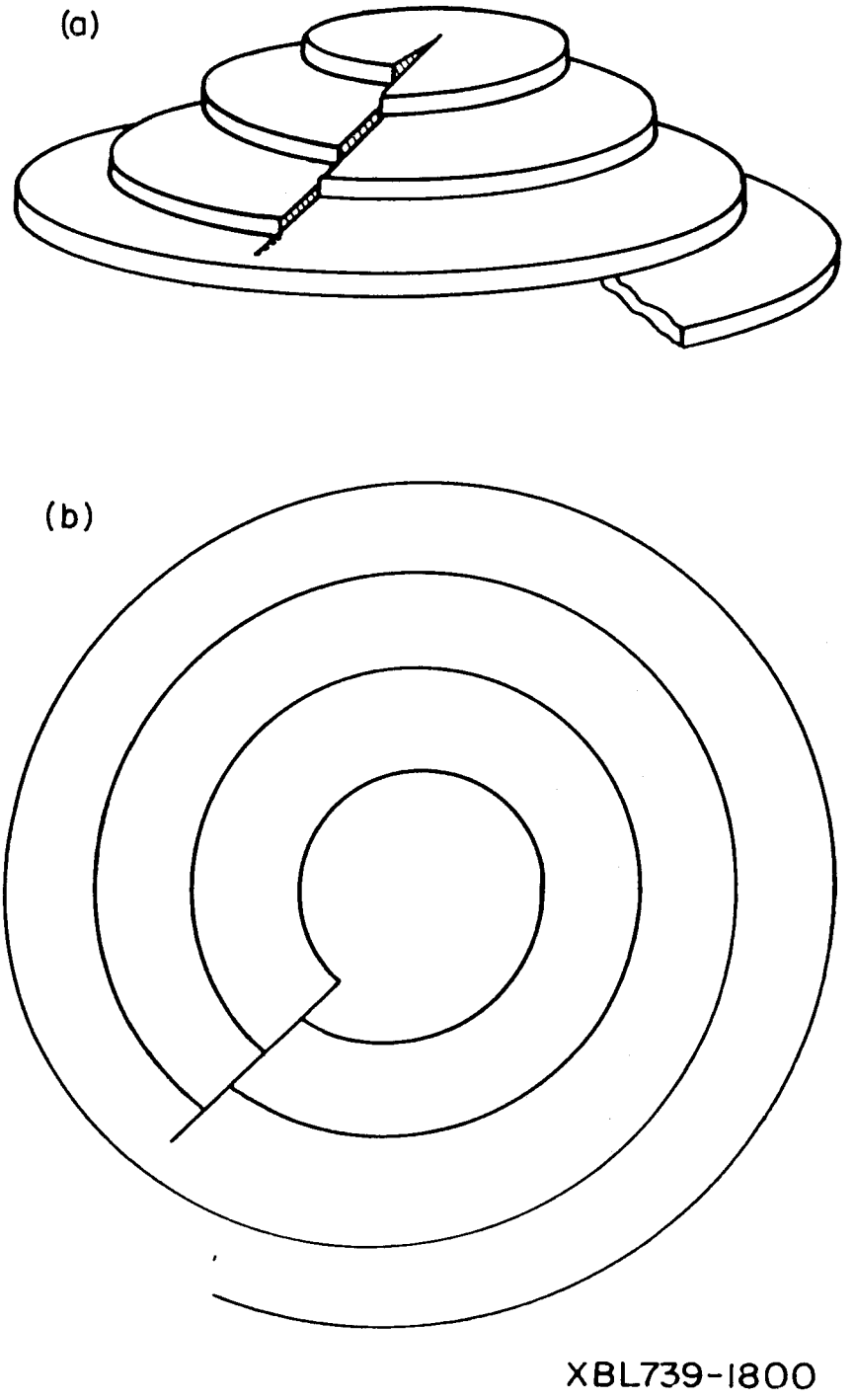


Fig. 9

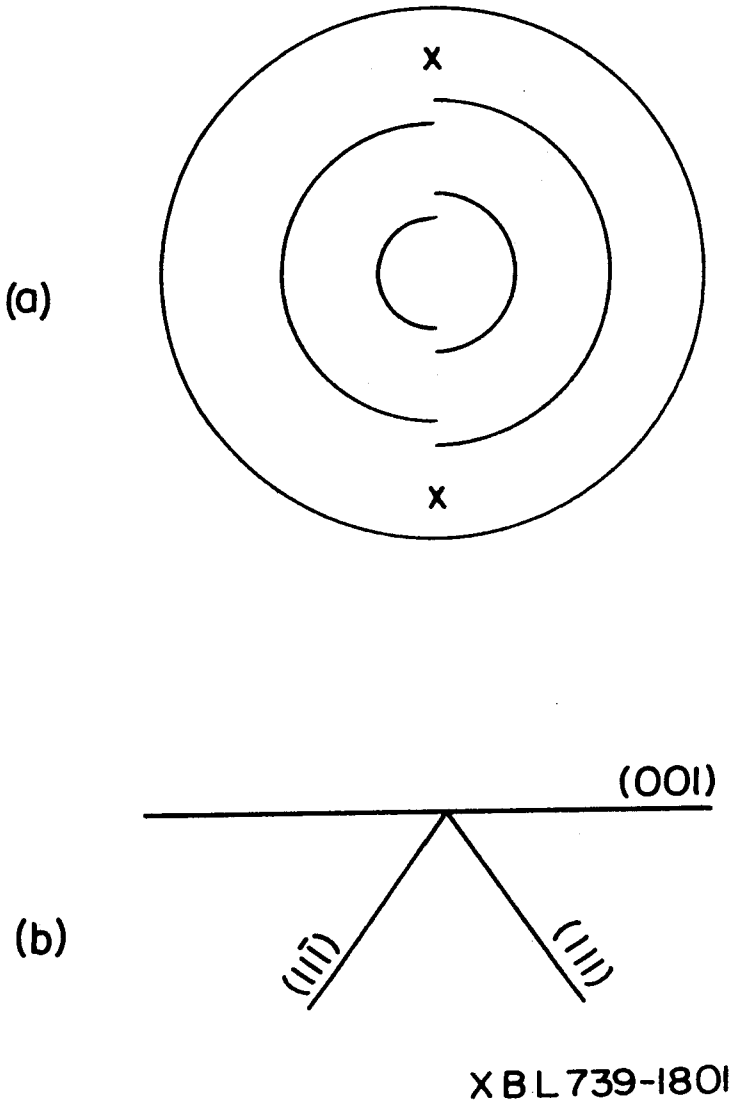
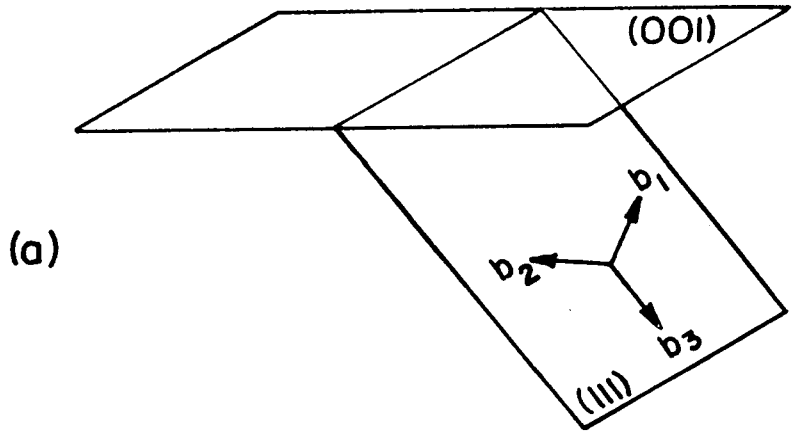


Fig. 10



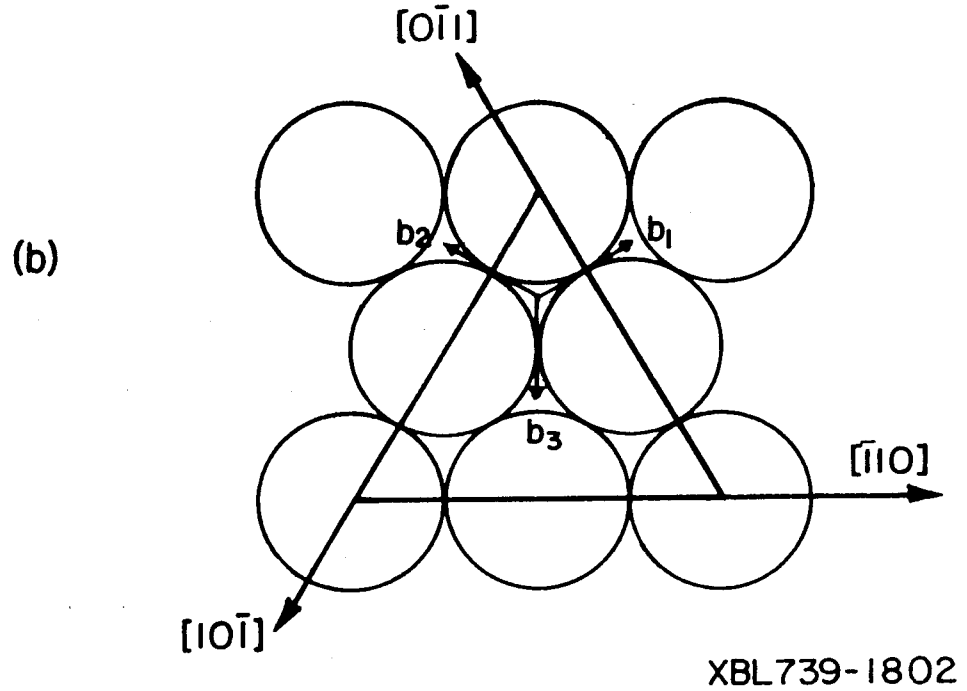


Fig. 11

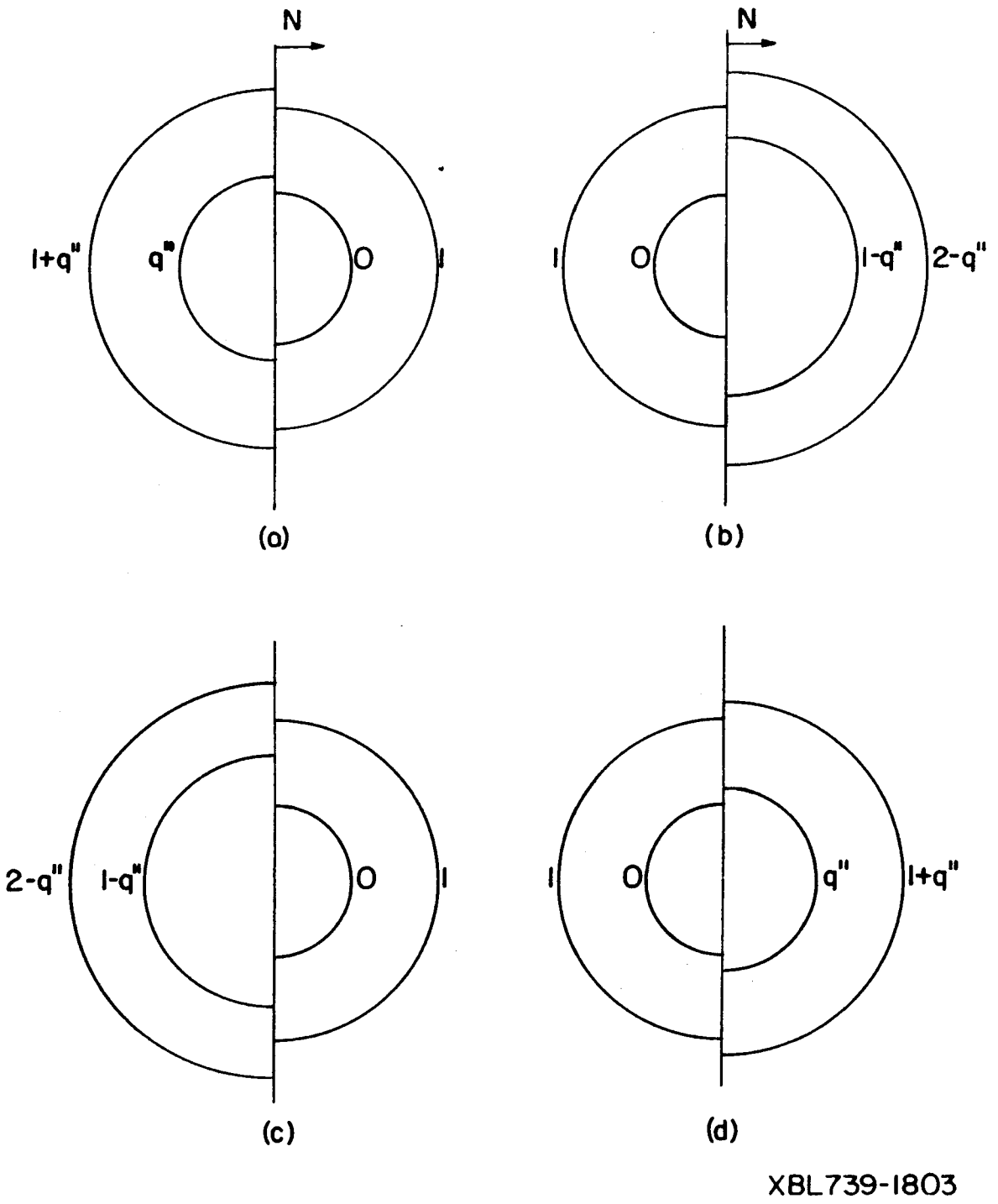
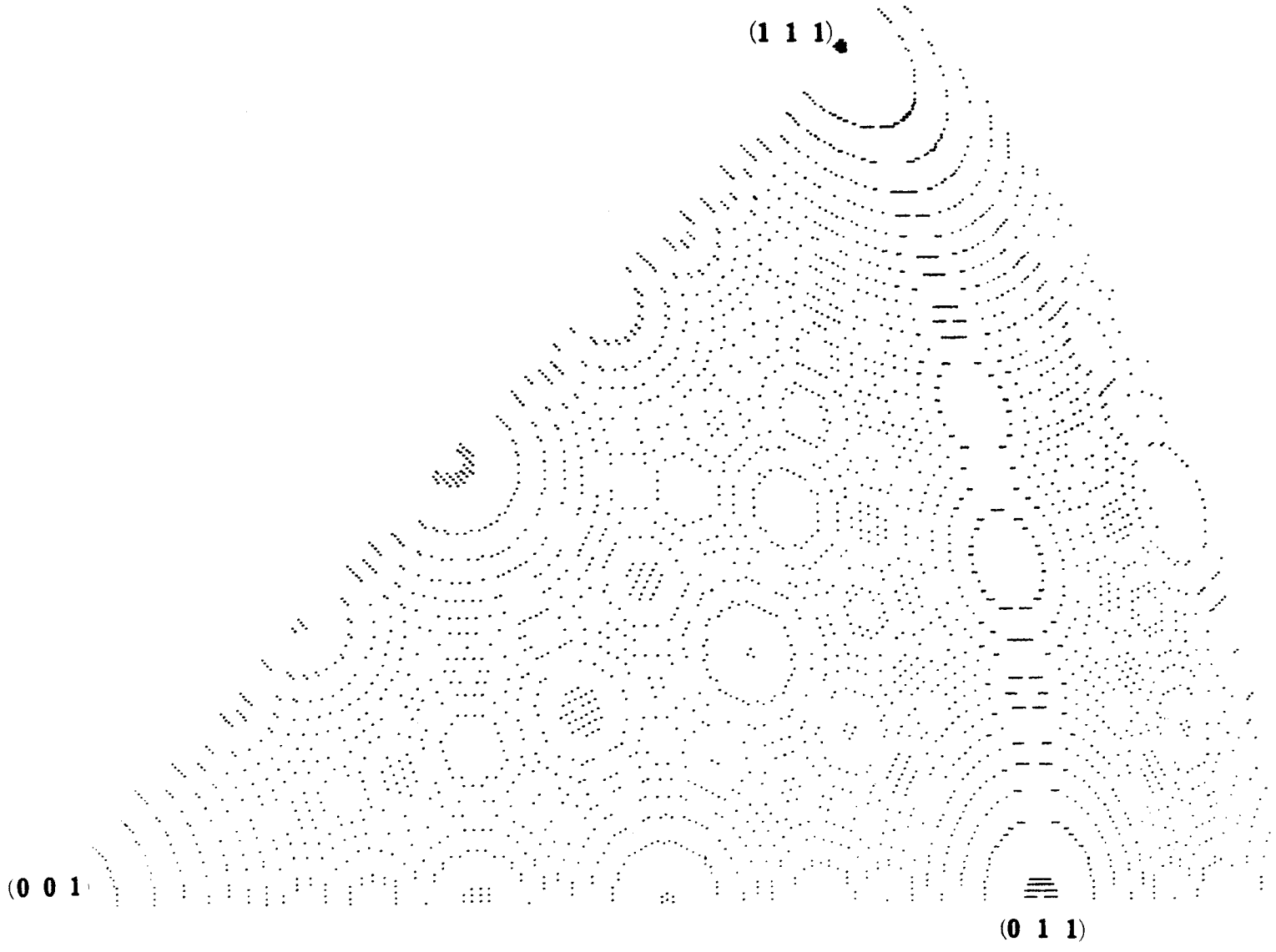
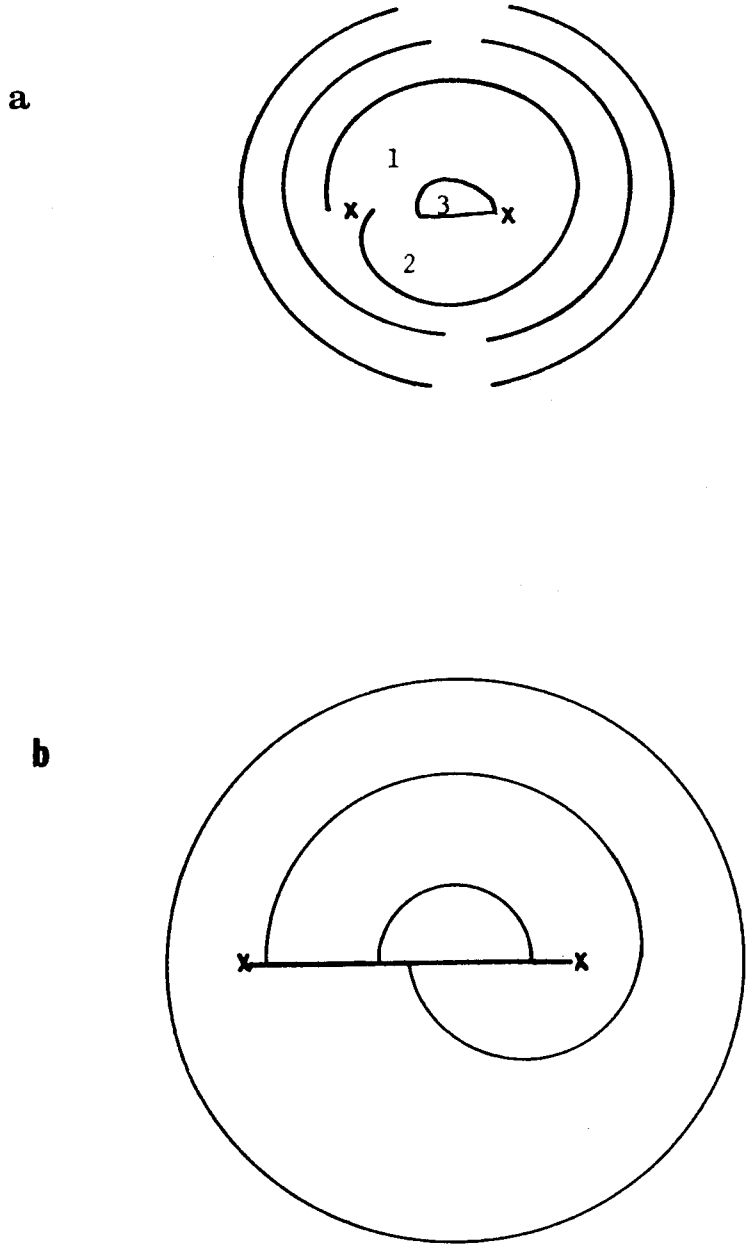


Fig. 12



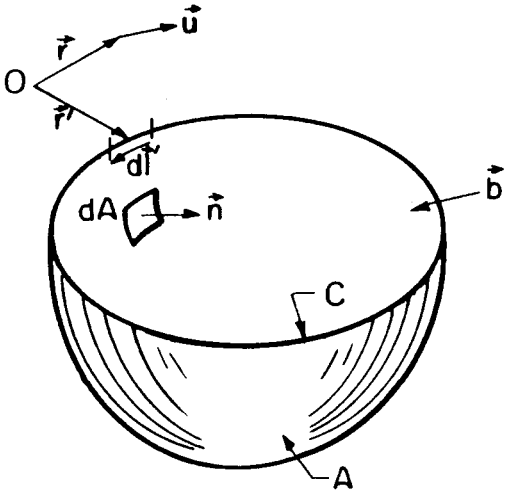
XBL 738-1111A

Fig. 13



XBL739-1826A

Fig. 14



XBL739-1804

Fig. 15

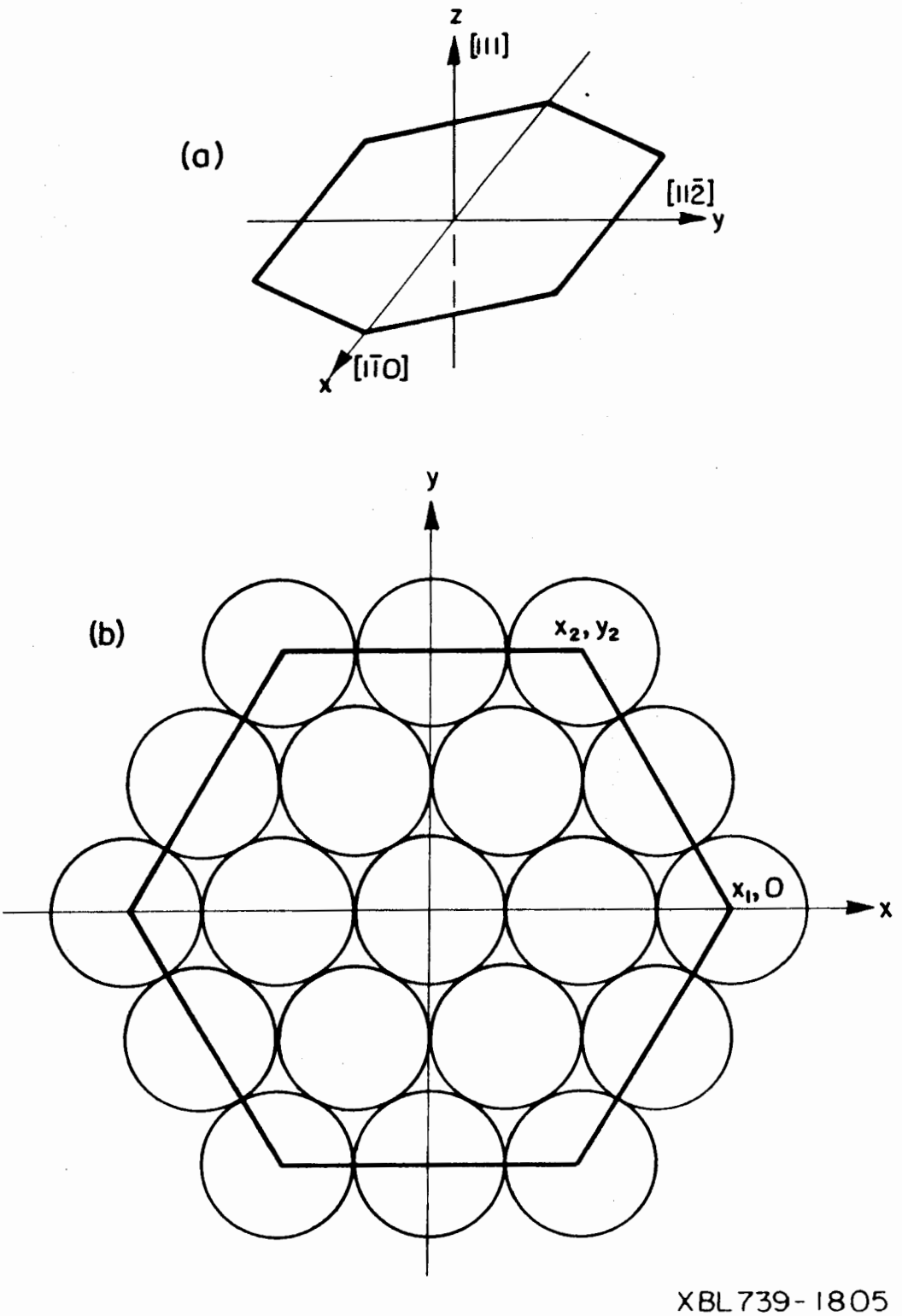
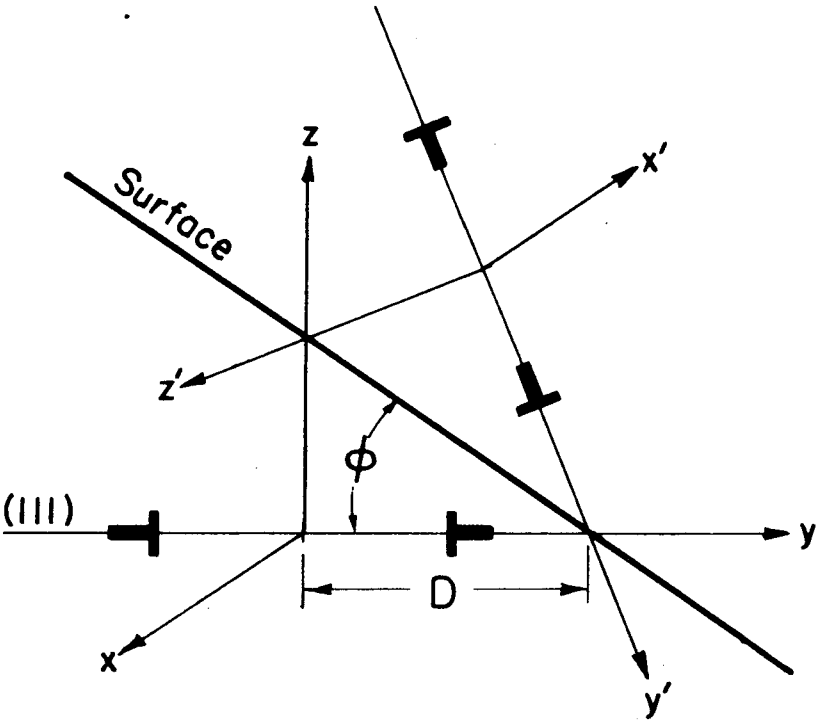


Fig. 16



XBL739-1806

Fig. 17

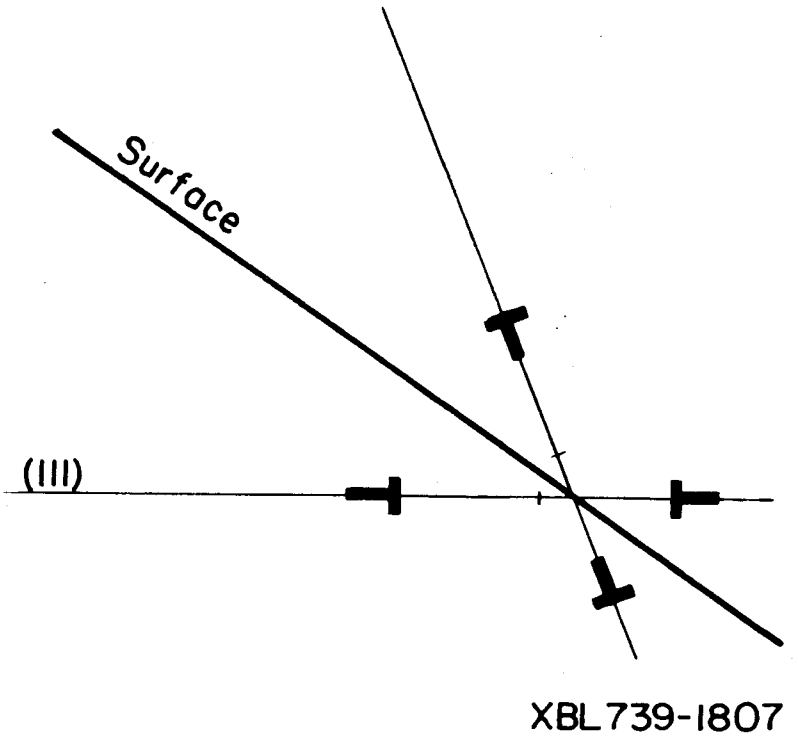


Fig. 18

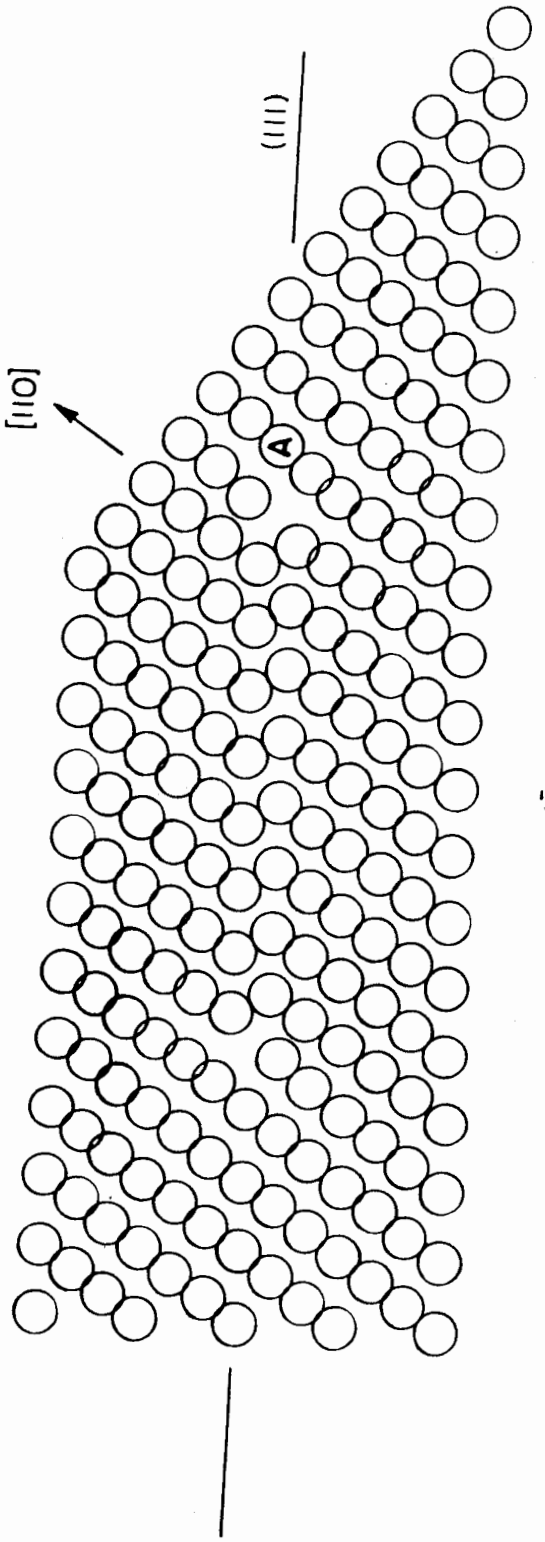


Fig. 19

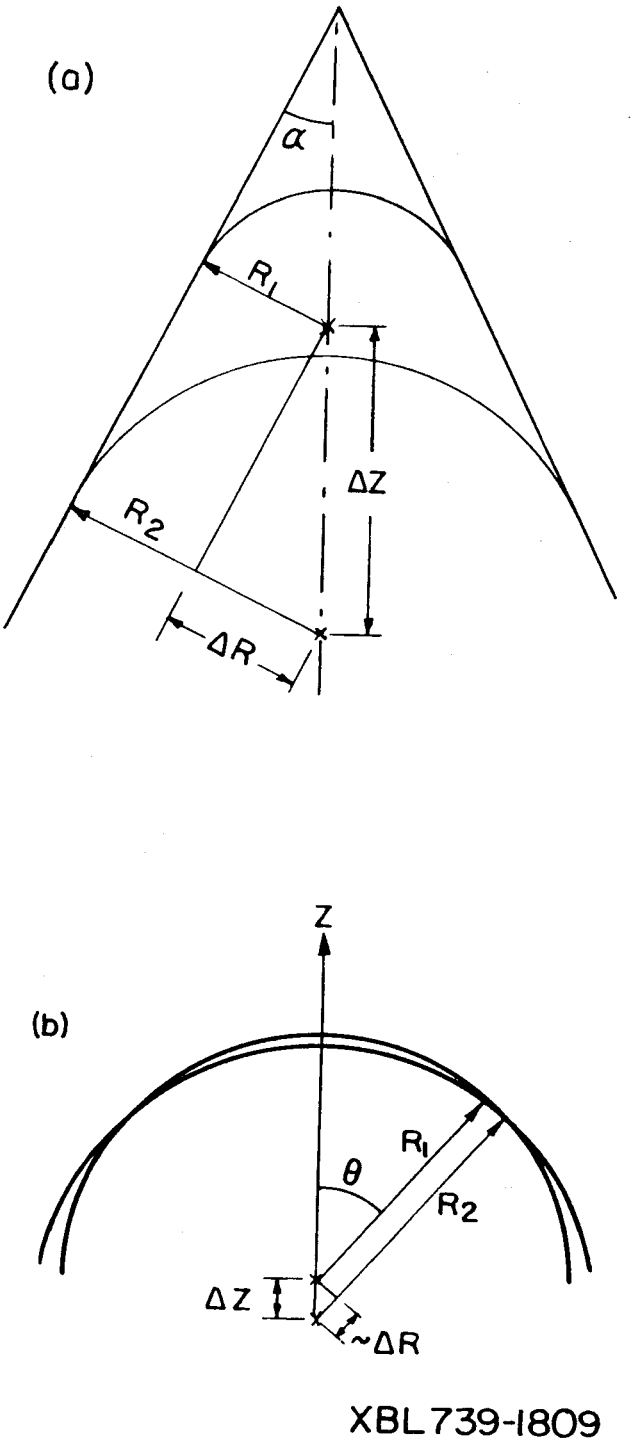


Fig. 20

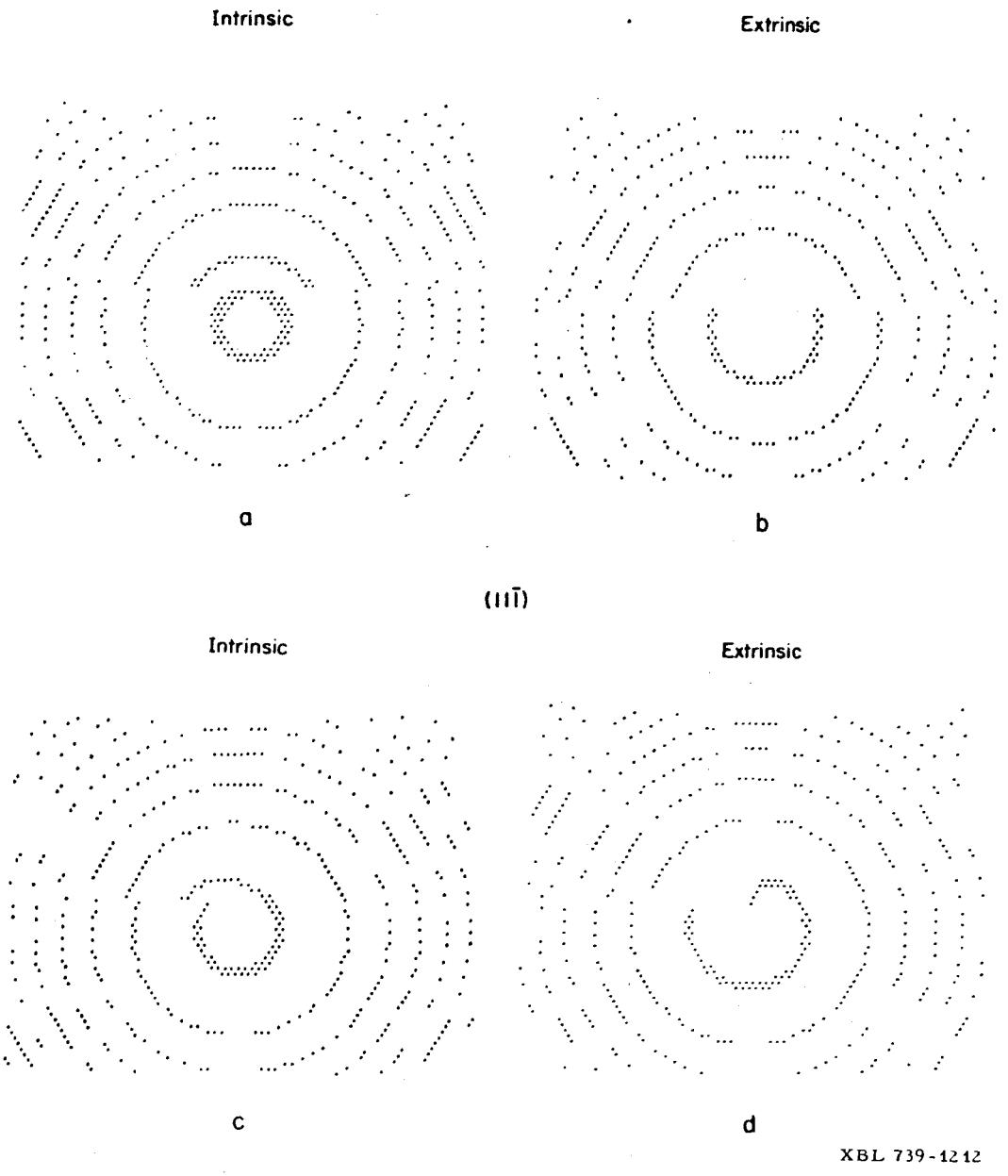

Intrinsic
Extrinsic
a
b
(111)
Intrinsic
Extrinsic
c
d
XBL 739-1212

Fig. 21

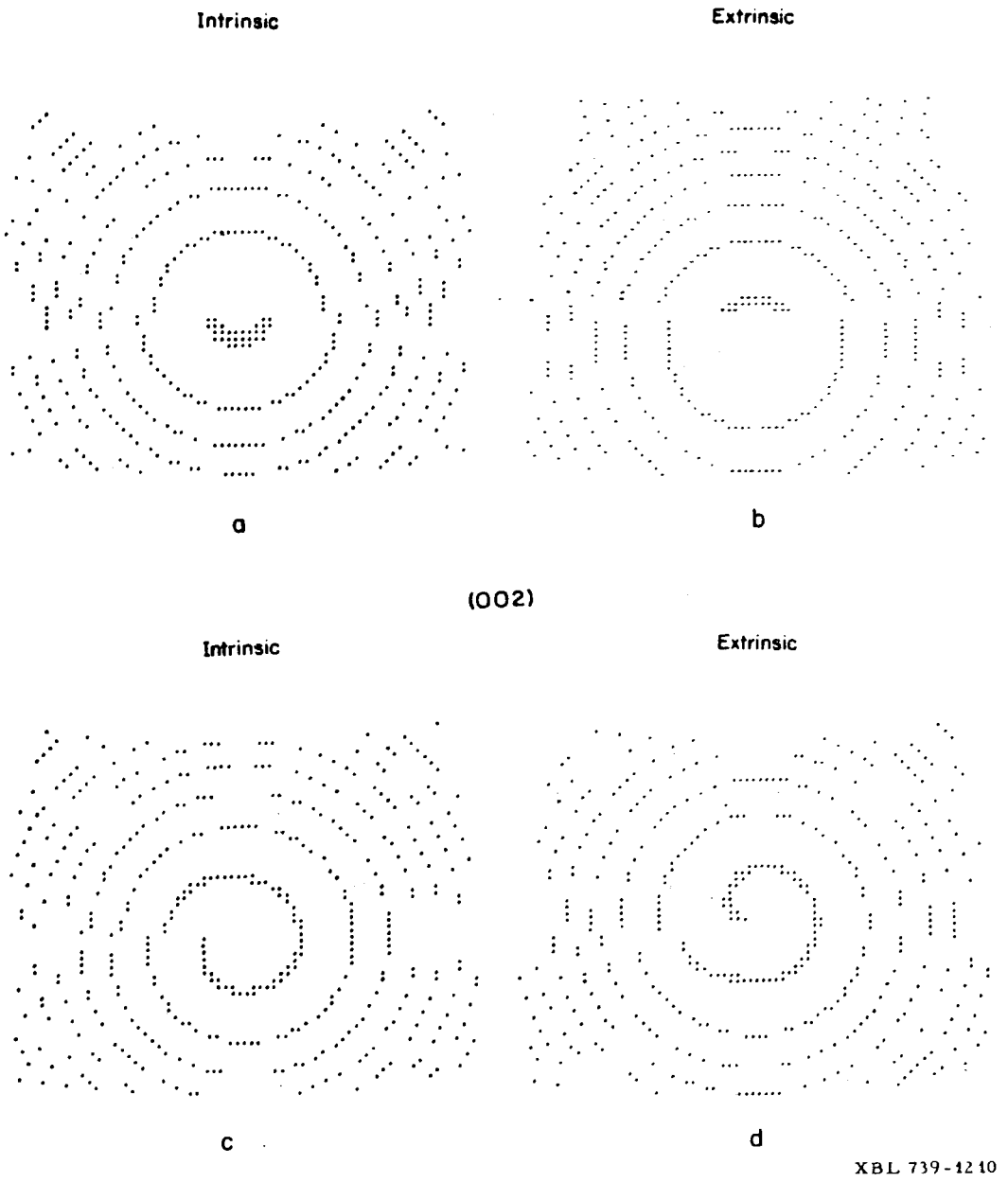
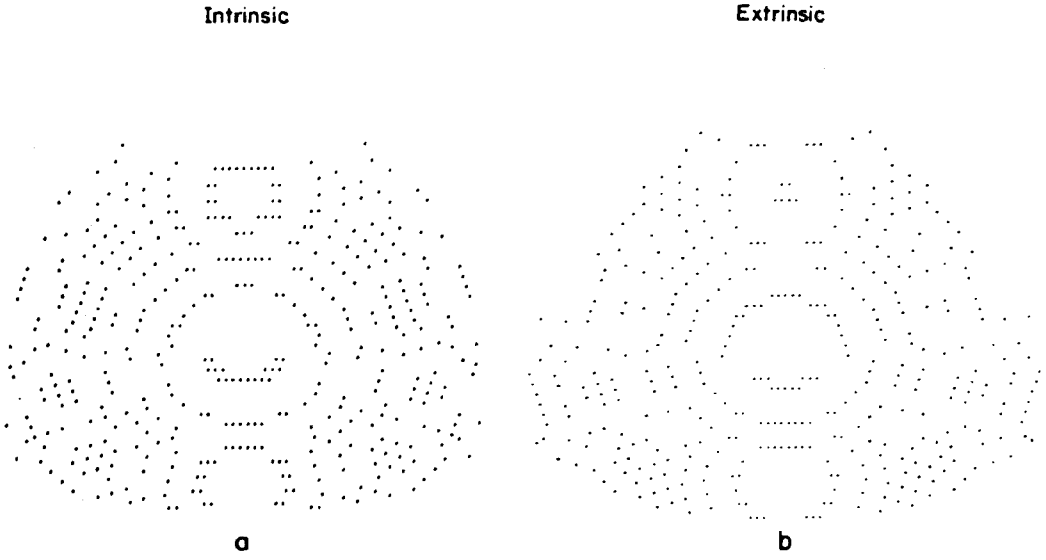
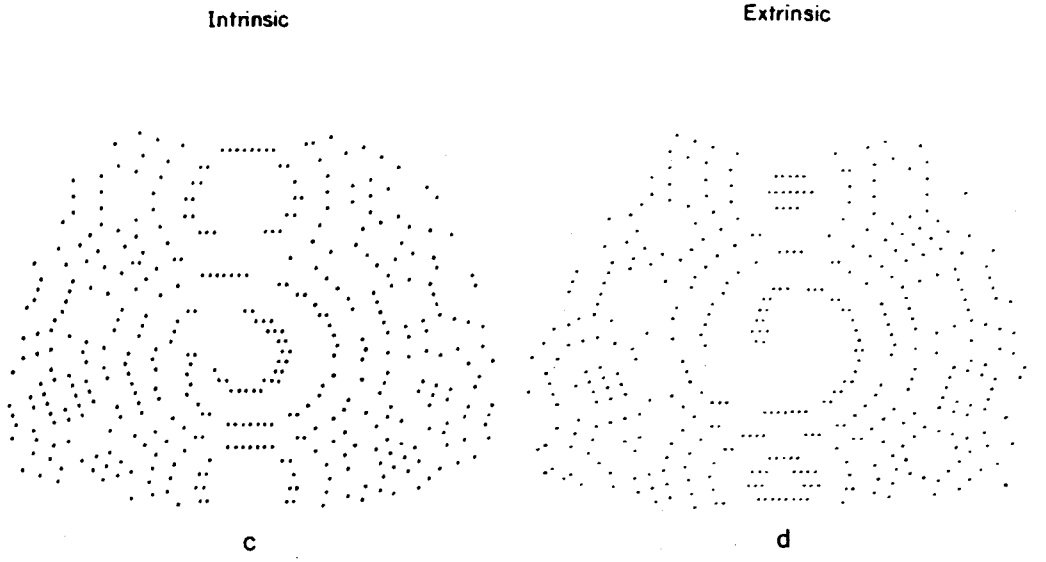

Intrinsic
Extrinsic
a
b
(002)
Intrinsic
Extrinsic
c
d
XBL 739-1210

Fig. 22



(113)



XBL 739-1203

Fig. 23

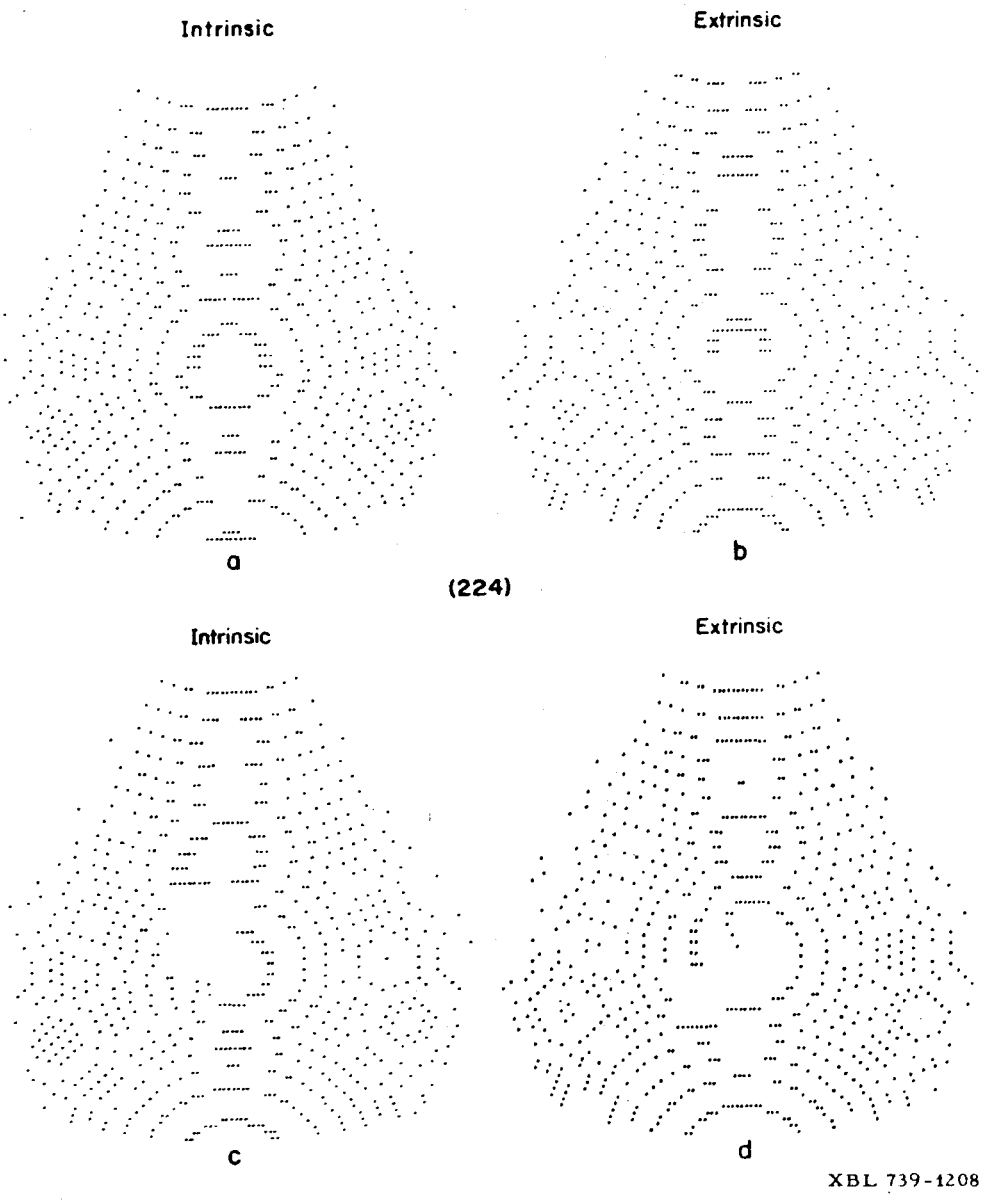

Intrinsic
Extrinsic
a
b
(224)
Intrinsic
Extrinsic
c
d
XBL 739-1208

Fig. 24

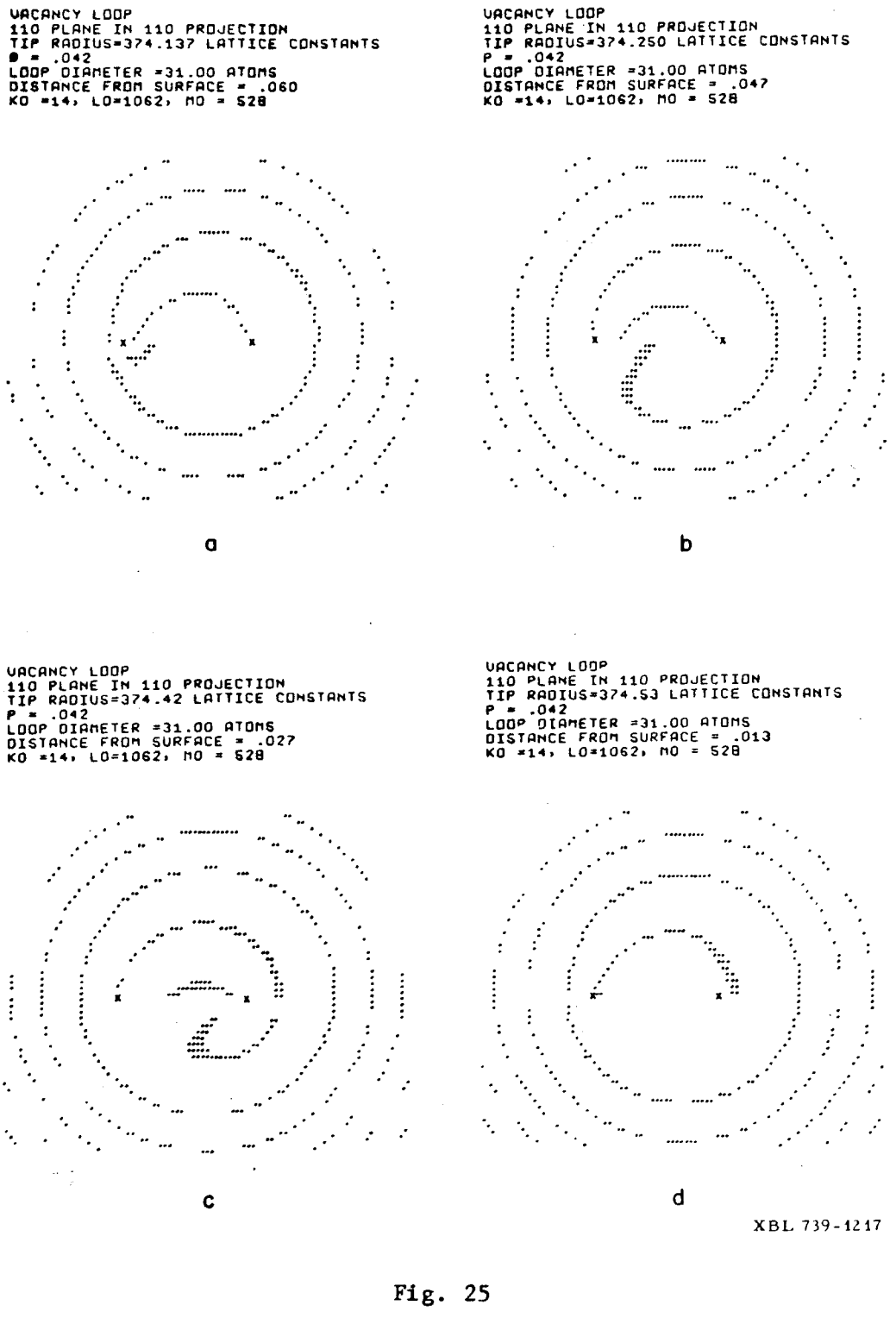

VACANCY LOOP
110 PLANE IN 110 PROJECTION
TIP RADIUS=374.137 LATTICE CONSTANTS
P = .042
LOOP DIAMETER =31.00 ATOMS
DISTANCE FROM SURFACE = .060
KO =14, LO=1062, MO = 528
VACANCY LOOP
110 PLANE IN 110 PROJECTION
TIP RADIUS=374.250 LATTICE CONSTANTS
P = .042
LOOP DIAMETER =31.00 ATOMS
DISTANCE FROM SURFACE = .047
KO =14, LO=1062, MO = 528
a
b
VACANCY LOOP
110 PLANE IN 110 PROJECTION
TIP RADIUS=374.42 LATTICE CONSTANTS
P = .042
LOOP DIAMETER =31.00 ATOMS
DISTANCE FROM SURFACE = .027
KO =14, LO=1062, MO = 528
VACANCY LOOP
110 PLANE IN 110 PROJECTION
TIP RADIUS=374.53 LATTICE CONSTANTS
P = .042
LOOP DIAMETER =31.00 ATOMS
DISTANCE FROM SURFACE = .013
KO =14, LO=1062, MO = 528
c
d
XBL 739-1217

Fig. 25

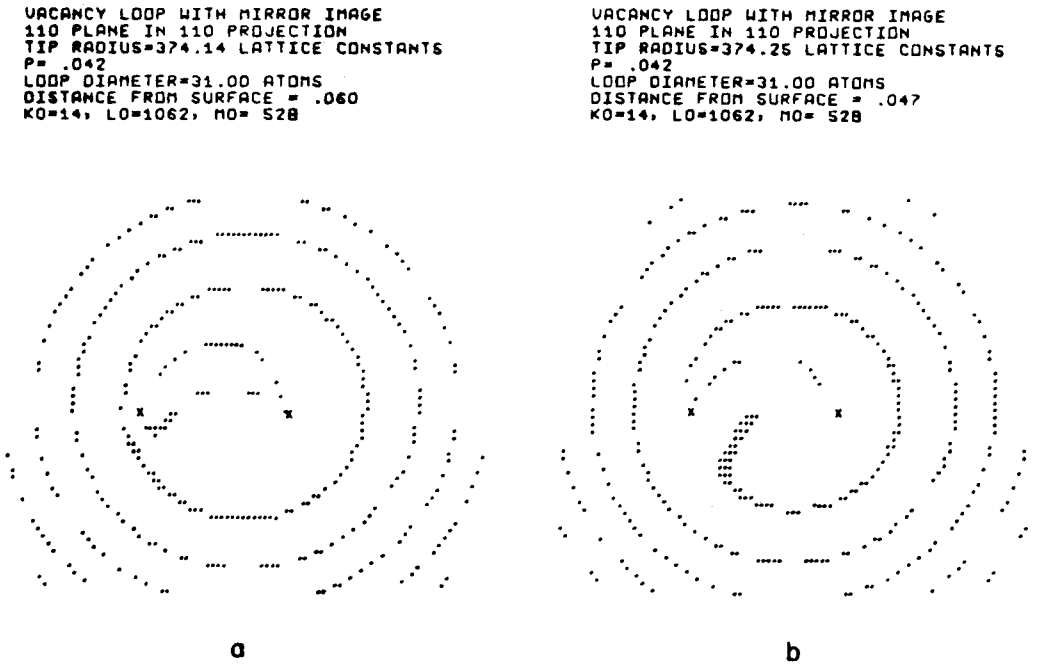

VACANCY LOOP WITH MIRROR IMAGE
110 PLANE IN 110 PROJECTION
TIP RADIUS=374.14 LATTICE CONSTANTS
P= .042
LOOP DIAMETER=31.00 ATOMS
DISTANCE FROM SURFACE = .060
KO=14, LO=1062, MO= 528
VACANCY LOOP WITH MIRROR IMAGE
110 PLANE IN 110 PROJECTION
TIP RADIUS=374.25 LATTICE CONSTANTS
P= .042
LOOP DIAMETER=31.00 ATOMS
DISTANCE FROM SURFACE = .047
KO=14, LO=1062, MO= 528
a
b
VACANCY LOOP WITH MIRROR IMAGE
110 PLANE IN 110 PROJECTION
TIP RADIUS=374.42 LATTICE CONSTANTS
P= .042
LOOP DIAMETER=31.00 ATOMS
DISTANCE FROM SURFACE = .027
KO=14, LO=1062, MO= 528
VACANCY LOOP WITH MIRROR IMAGE
110 PLANE IN 110 PROJECTION
TIP RADIUS=374.53 LATTICE CONSTANTS
P= .042
LOOP DIAMETER=31.00 ATOMS
DISTANCE FROM SURFACE = .013
KO=14, LO=1062, MO= 528
c
d
XBL 739-1216

Fig. 26

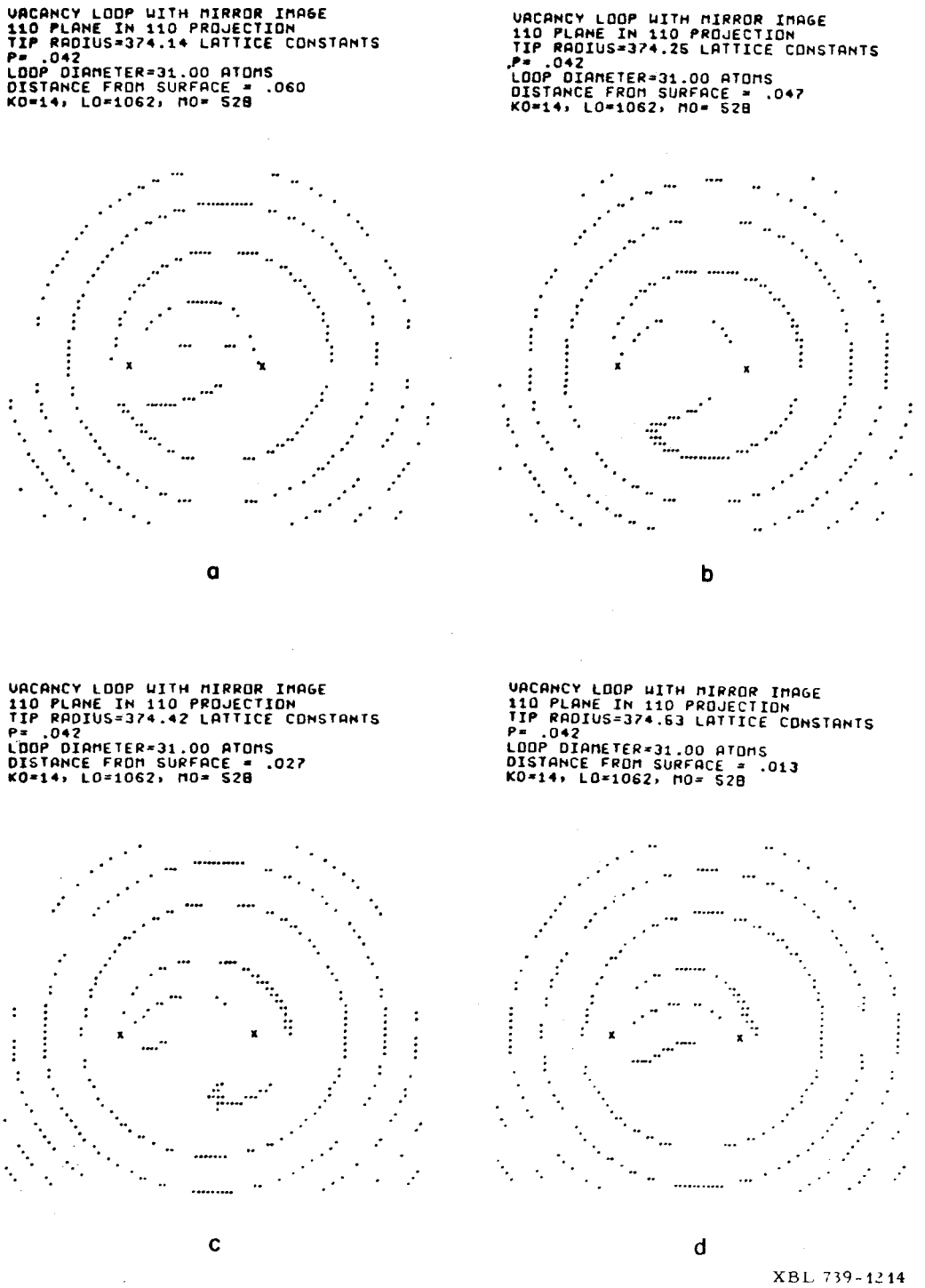

VACANCY LOOP WITH MIRROR IMAGE
110 PLANE IN 110 PROJECTION
TIP RADIUS=374.14 LATTICE CONSTANTS
P= .042
LOOP DIAMETER=31.00 ATOMS
DISTANCE FROM SURFACE = .060
KO=14, LO=1062, MO= 528
VACANCY LOOP WITH MIRROR IMAGE
110 PLANE IN 110 PROJECTION
TIP RADIUS=374.25 LATTICE CONSTANTS
P= .042
LOOP DIAMETER=31.00 ATOMS
DISTANCE FROM SURFACE = .047
KO=14, LO=1062, MO= 528
a
b
VACANCY LOOP WITH MIRROR IMAGE
110 PLANE IN 110 PROJECTION
TIP RADIUS=374.42 LATTICE CONSTANTS
P= .042
LOOP DIAMETER=31.00 ATOMS
DISTANCE FROM SURFACE = .027
KO=14, LO=1062, MO= 528
VACANCY LOOP WITH MIRROR IMAGE
110 PLANE IN 110 PROJECTION
TIP RADIUS=374.63 LATTICE CONSTANTS
P= .042
LOOP DIAMETER=31.00 ATOMS
DISTANCE FROM SURFACE = .013
KO=14, LO=1062, MO= 528
c
d
XBL 739-1214

Fig. 27

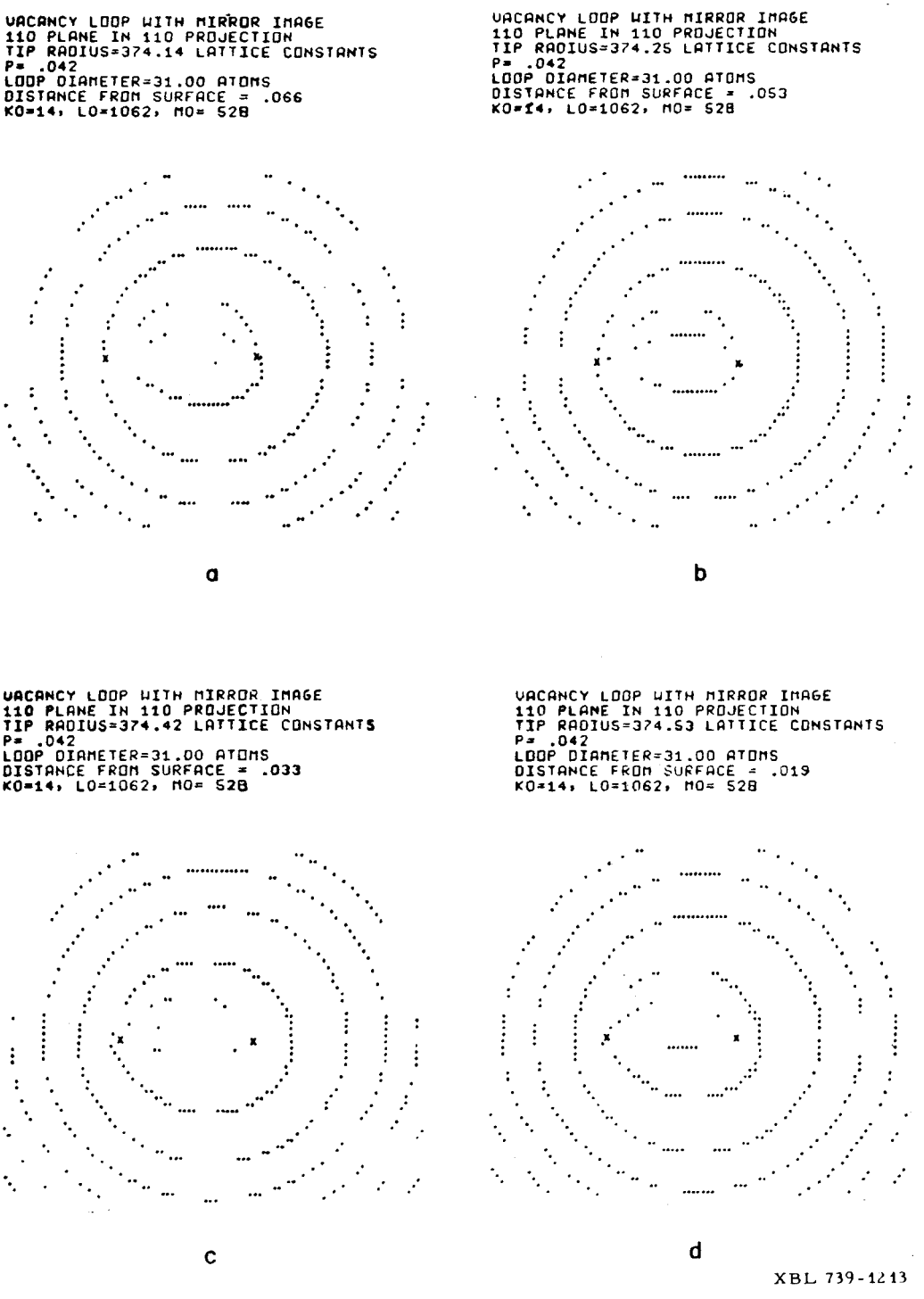

VACANCY LOOP WITH MIRROR IMAGE
110 PLANE IN 110 PROJECTION
TIP RADIUS=374.14 LATTICE CONSTANTS
P= .042
LOOP DIAMETER=31.00 ATOMS
DISTANCE FROM SURFACE = .066
KO=14, LO=1062, MO= 528
VACANCY LOOP WITH MIRROR IMAGE
110 PLANE IN 110 PROJECTION
TIP RADIUS=374.25 LATTICE CONSTANTS
P= .042
LOOP DIAMETER=31.00 ATOMS
DISTANCE FROM SURFACE = .053
KO=14, LO=1062, MO= 528
a
b
VACANCY LOOP WITH MIRROR IMAGE
110 PLANE IN 110 PROJECTION
TIP RADIUS=374.42 LATTICE CONSTANTS
P= .042
LOOP DIAMETER=31.00 ATOMS
DISTANCE FROM SURFACE = .033
KO=14, LO=1062, MO= 528
VACANCY LOOP WITH MIRROR IMAGE
110 PLANE IN 110 PROJECTION
TIP RADIUS=374.53 LATTICE CONSTANTS
P= .042
LOOP DIAMETER=31.00 ATOMS
DISTANCE FROM SURFACE = .019
KO=14, LO=1062, MO= 528
c
d
XBL 739-1213

Fig. 28

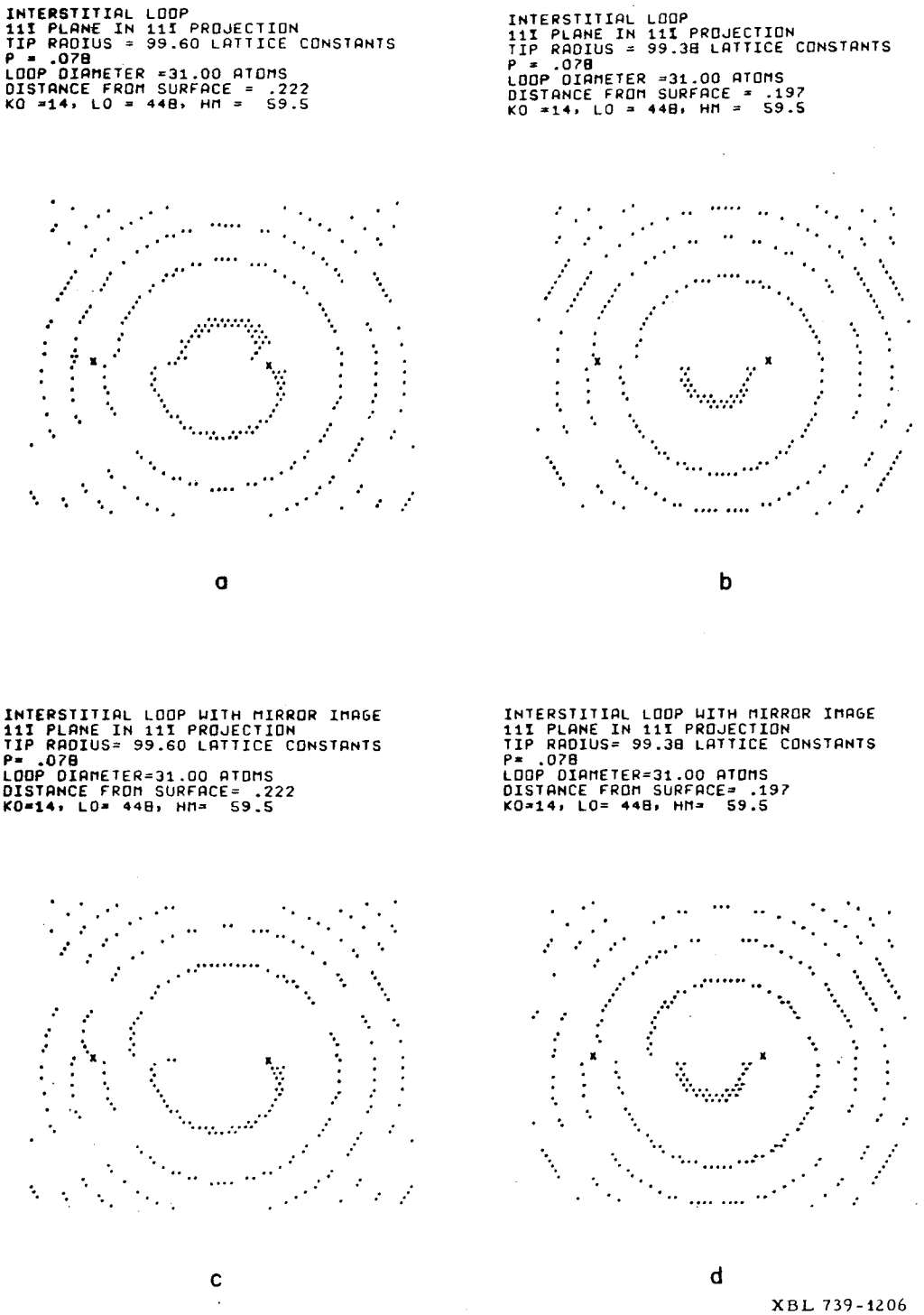
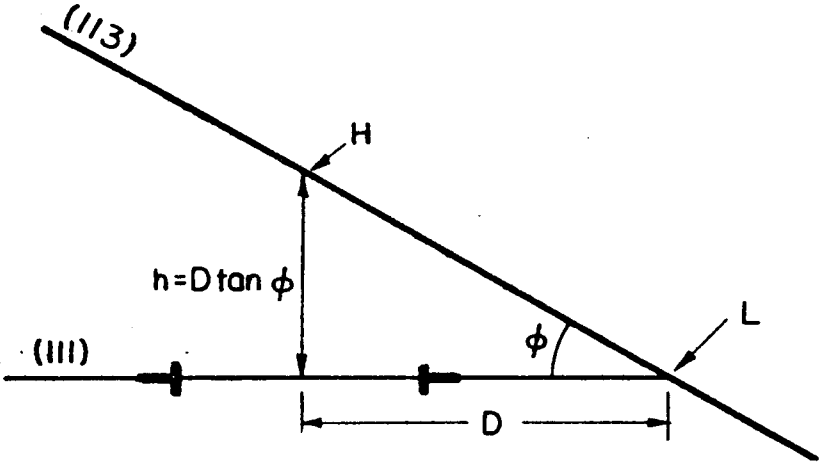

INTERSTITIAL LOOP
111 PLANE IN 111 PROJECTION
TIP RADIUS = 99.60 LATTICE CONSTANTS
P = .078
LOOP DIAMETER =31.00 ATOMS
DISTANCE FROM SURFACE = .222
KO =14, LO = 448, HM = 59.5
INTERSTITIAL LOOP
111 PLANE IN 111 PROJECTION
TIP RADIUS = 99.38 LATTICE CONSTANTS
P = .078
LOOP DIAMETER =31.00 ATOMS
DISTANCE FROM SURFACE = .197
KO =14, LO = 448, HM = 59.5
a
b
INTERSTITIAL LOOP WITH MIRROR IMAGE
111 PLANE IN 111 PROJECTION
TIP RADIUS= 99.60 LATTICE CONSTANTS
P= .078
LOOP DIAMETER=31.00 ATOMS
DISTANCE FROM SURFACE= .222
KO=14, LO= 448, HM= 59.5
INTERSTITIAL LOOP WITH MIRROR IMAGE
111 PLANE IN 111 PROJECTION
TIP RADIUS= 99.38 LATTICE CONSTANTS
P= .078
LOOP DIAMETER=31.00 ATOMS
DISTANCE FROM SURFACE= .197
KO=14, LO= 448, HM= 59.5
c
d
XBL 739-1206

Fig. 29



XBL739-1833

Fig. 30

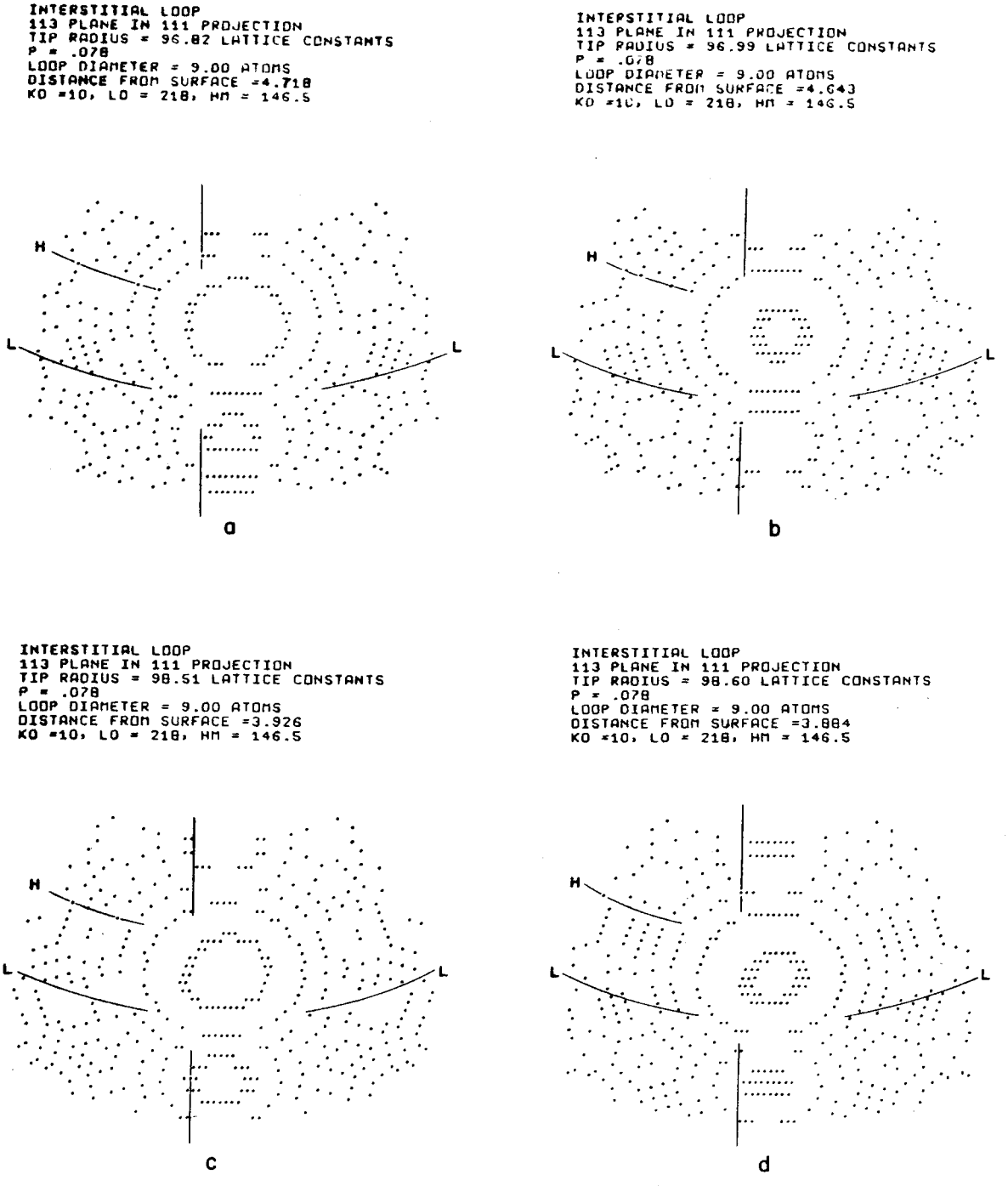

INTERSTITIAL LOOP
113 PLANE IN 111 PROJECTION
TIP RADIUS = 96.82 LATTICE CONSTANTS
P = .078
LOOP DIAMETER = 9.00 ATOMS
DISTANCE FROM SURFACE =4.718
KO =10, LO = 218, HM = 146.5
H
L
L
a
INTERSTITIAL LOOP
113 PLANE IN 111 PROJECTION
TIP RADIUS = 96.99 LATTICE CONSTANTS
P = .078
LOOP DIAMETER = 9.00 ATOMS
DISTANCE FROM SURFACE =4.643
KO =10, LO = 218, HM = 146.5
H
L
L
b
INTERSTITIAL LOOP
113 PLANE IN 111 PROJECTION
TIP RADIUS = 98.51 LATTICE CONSTANTS
P = .078
LOOP DIAMETER = 9.00 ATOMS
DISTANCE FROM SURFACE =3.926
KO =10, LO = 218, HM = 146.5
H
L
L
c
INTERSTITIAL LOOP
113 PLANE IN 111 PROJECTION
TIP RADIUS = 98.60 LATTICE CONSTANTS
P = .078
LOOP DIAMETER = 9.00 ATOMS
DISTANCE FROM SURFACE =3.884
KO =10, LO = 218, HM = 146.5
H
L
L
d
XBL 739-1215

Fig. 31

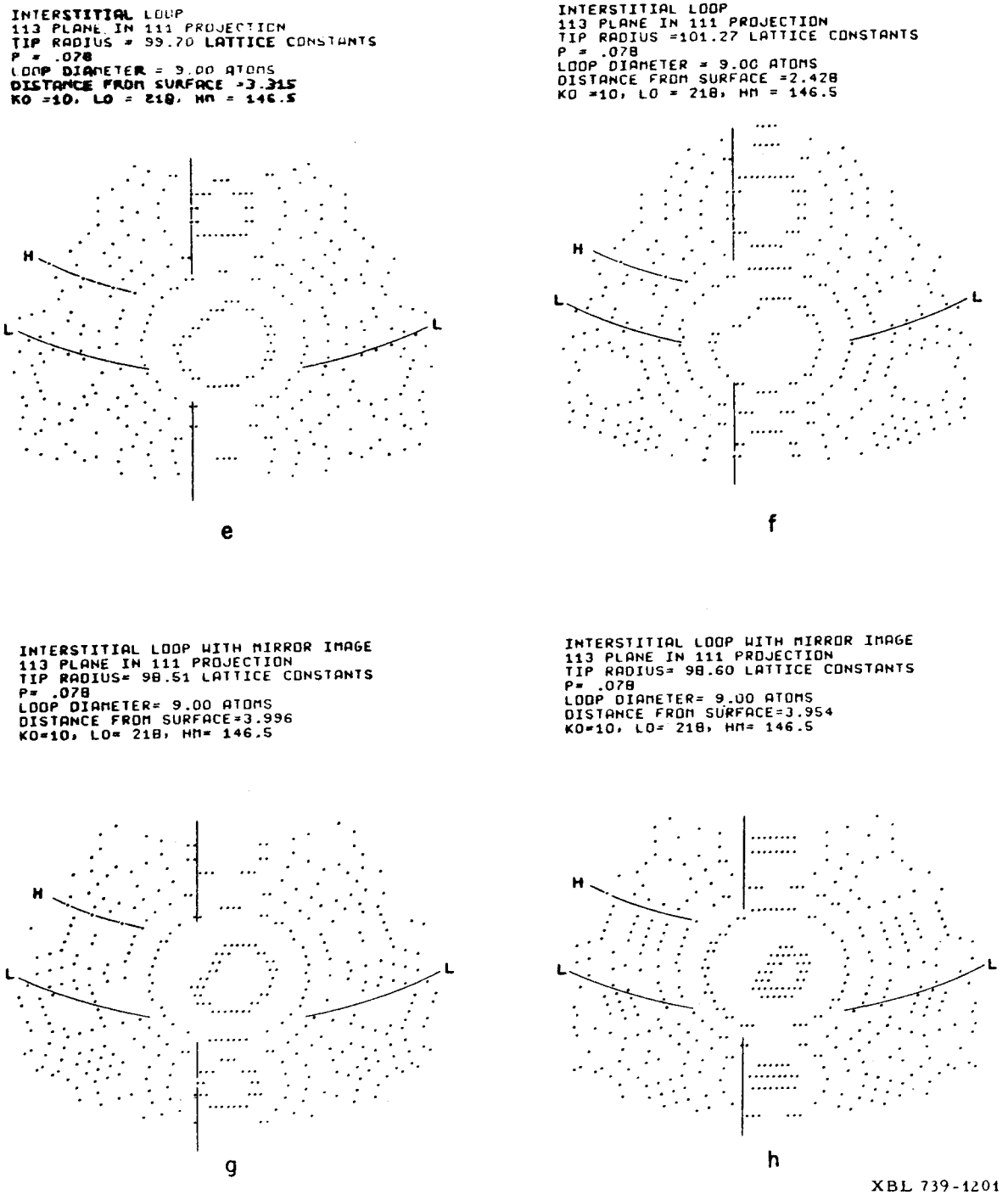

INTERSTITIAL LOOP
113 PLANE IN 111 PROJECTION
TIP RADIUS = 99.70 LATTICE CONSTANTS
P = .078
LOOP DIAMETER = 9.00 ATOMS
DISTANCE FROM SURFACE =3.315
KO =10, LO = 218, HH = 146.5
H
L
L
e
INTERSTITIAL LOOP
113 PLANE IN 111 PROJECTION
TIP RADIUS =101.27 LATTICE CONSTANTS
P = .078
LOOP DIAMETER = 9.00 ATOMS
DISTANCE FROM SURFACE =2.428
KO =10, LO = 218, HH = 146.5
H
L
L
f
INTERSTITIAL LOOP WITH MIRROR IMAGE
113 PLANE IN 111 PROJECTION
TIP RADIUS= 98.51 LATTICE CONSTANTS
P= .078
LOOP DIAMETER= 9.00 ATOMS
DISTANCE FROM SURFACE=3.996
KO=10, LO= 218, HH= 146.5
H
L
L
g
INTERSTITIAL LOOP WITH MIRROR IMAGE
113 PLANE IN 111 PROJECTION
TIP RADIUS= 98.60 LATTICE CONSTANTS
P= .078
LOOP DIAMETER= 9.00 ATOMS
DISTANCE FROM SURFACE=3.954
KO=10, LO= 218, HH= 146.5
H
L
L
h
XBL 739-1201

Fig. 31 (cont.)

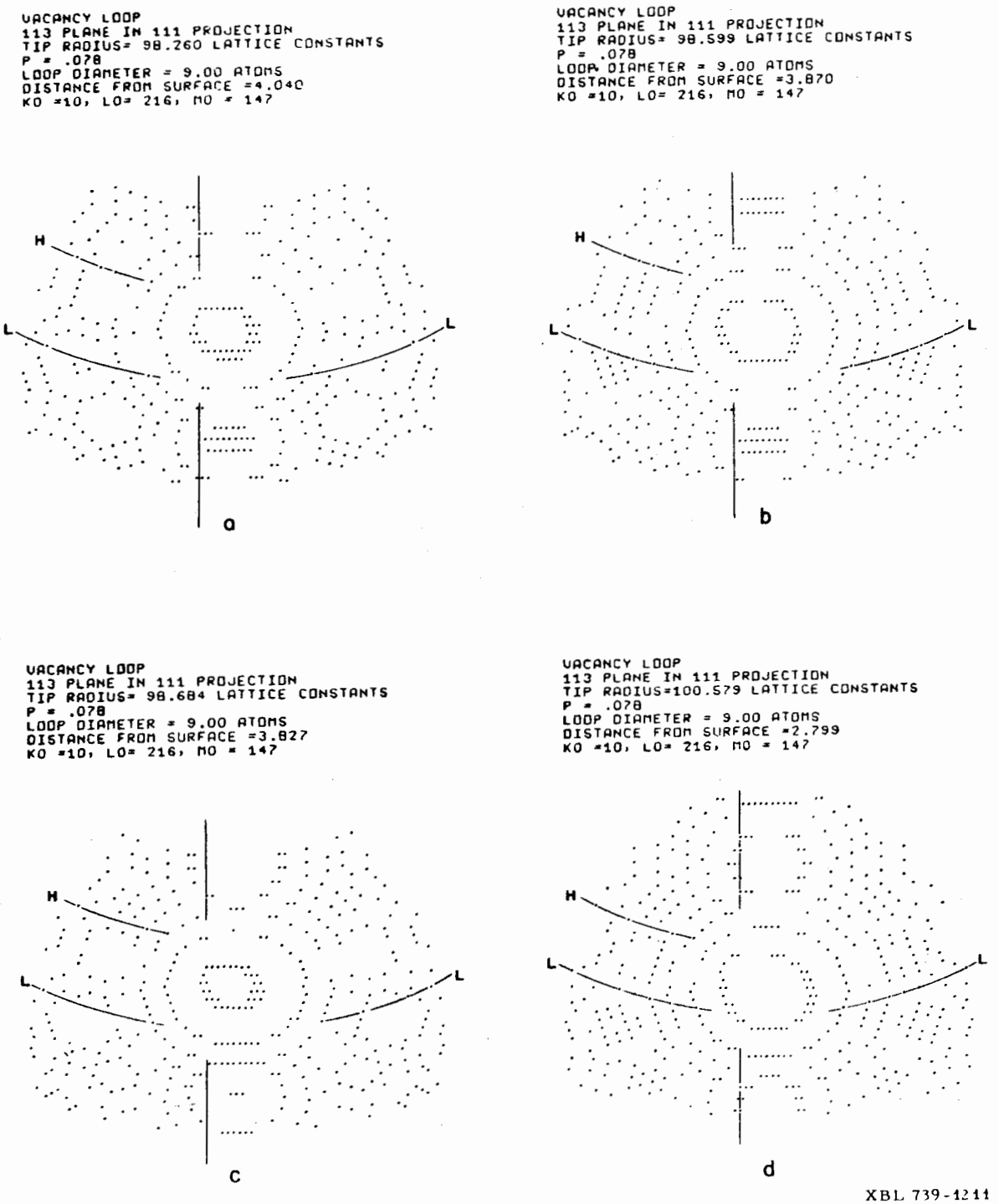

VACANCY LOOP
113 PLANE IN 111 PROJECTION
TIP RADIUS= 98.260 LATTICE CONSTANTS
P = .078
LOOP DIAMETER = 9.00 ATOMS
DISTANCE FROM SURFACE =4.040
KO =10, LO= 216, MO = 147
H
L
L
a
VACANCY LOOP
113 PLANE IN 111 PROJECTION
TIP RADIUS= 98.599 LATTICE CONSTANTS
P = .078
LOOP DIAMETER = 9.00 ATOMS
DISTANCE FROM SURFACE =3.870
KO =10, LO= 216, MO = 147
H
L
L
b
VACANCY LOOP
113 PLANE IN 111 PROJECTION
TIP RADIUS= 98.684 LATTICE CONSTANTS
P = .078
LOOP DIAMETER = 9.00 ATOMS
DISTANCE FROM SURFACE =3.827
KO =10, LO= 216, MO = 147
H
L
L
c
VACANCY LOOP
113 PLANE IN 111 PROJECTION
TIP RADIUS=100.579 LATTICE CONSTANTS
P = .078
LOOP DIAMETER = 9.00 ATOMS
DISTANCE FROM SURFACE =2.799
KO =10, LO= 216, MO = 147
H
L
L
d
XBL 739-1211

Fig. 32

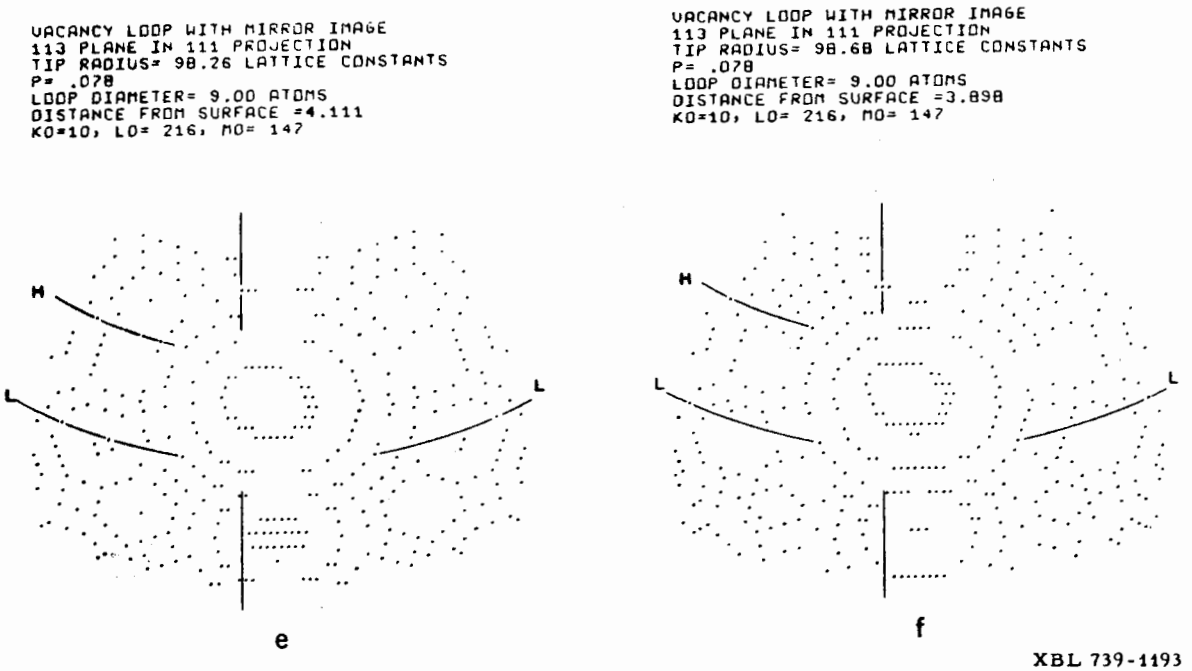

VACANCY LOOP WITH MIRROR IMAGE
113 PLANE IN 111 PROJECTION
TIP RADIUS= 98.26 LATTICE CONSTANTS
P= .078
LOOP DIAMETER= 9.00 ATOMS
DISTANCE FROM SURFACE =4.111
KO=10, LO= 216, MO= 147
H
L
L
e
VACANCY LOOP WITH MIRROR IMAGE
113 PLANE IN 111 PROJECTION
TIP RADIUS= 98.68 LATTICE CONSTANTS
P= .078
LOOP DIAMETER= 9.00 ATOMS
DISTANCE FROM SURFACE =3.898
KO=10, LO= 216, MO= 147
H
L
L
f
XBL 739-1193

Fig. 32 (cont.)

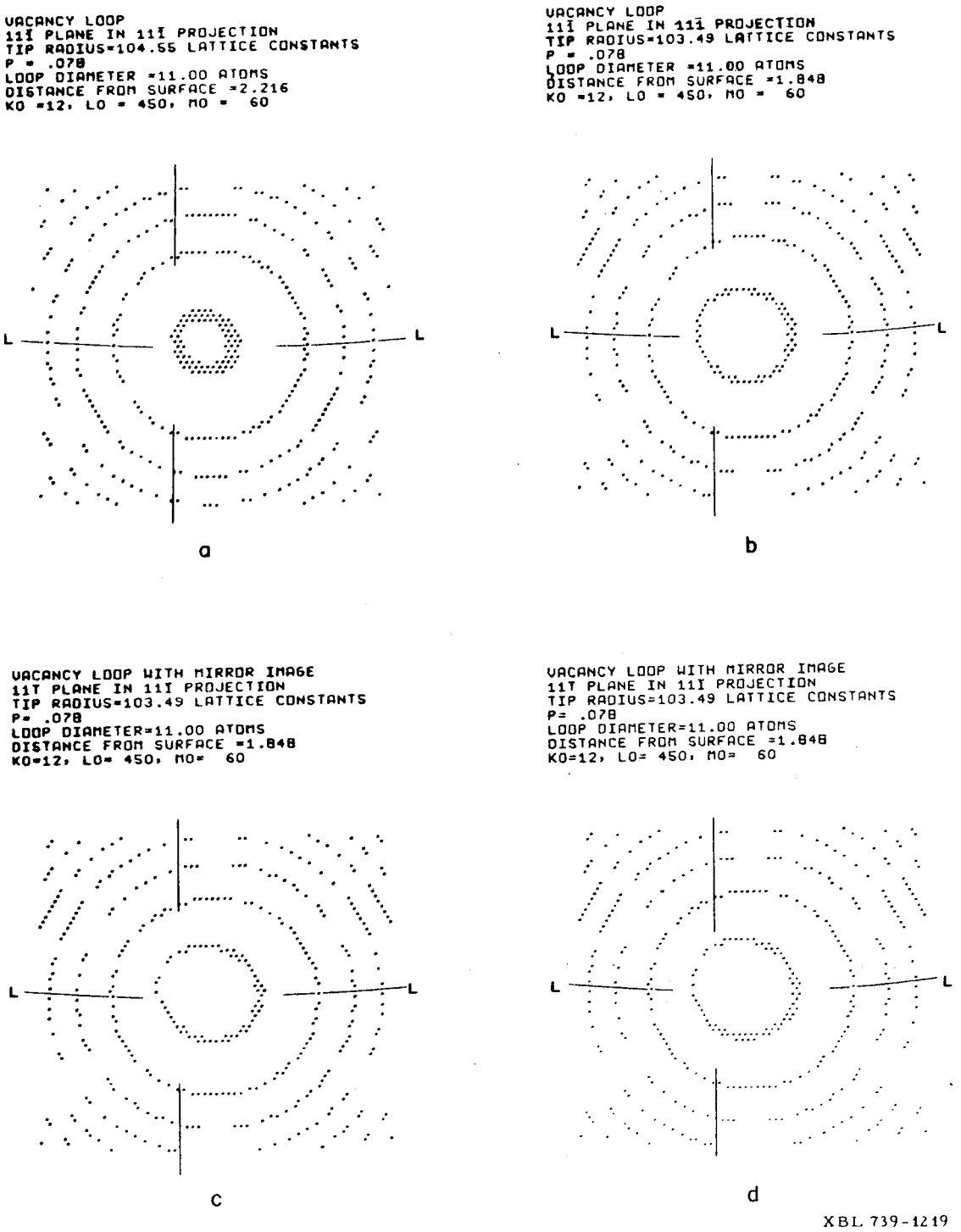
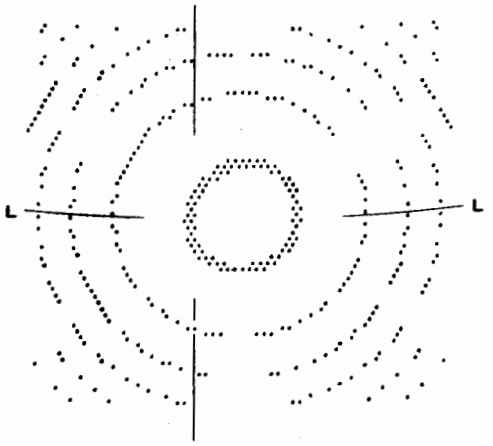

VACANCY LOOP
11Ī PLANE IN 11I PROJECTION
TIP RADIUS=104.55 LATTICE CONSTANTS
P = .078
LOOP DIAMETER =11.00 ATOMS
DISTANCE FROM SURFACE =2.216
KO =12, LO = 450, MO = 60
L
L
a
VACANCY LOOP
11Ī PLANE IN 11Ī PROJECTION
TIP RADIUS=103.49 LATTICE CONSTANTS
P = .078
LOOP DIAMETER =11.00 ATOMS
DISTANCE FROM SURFACE =1.848
KO =12, LO = 450, MO = 60
L
L
b
VACANCY LOOP WITH MIRROR IMAGE
11T PLANE IN 11I PROJECTION
TIP RADIUS=103.49 LATTICE CONSTANTS
P= .078
LOOP DIAMETER=11.00 ATOMS
DISTANCE FROM SURFACE =1.848
KO=12, LO= 450, MO= 60
L
L
c
VACANCY LOOP WITH MIRROR IMAGE
11T PLANE IN 11I PROJECTION
TIP RADIUS=103.49 LATTICE CONSTANTS
P= .078
LOOP DIAMETER=11.00 ATOMS
DISTANCE FROM SURFACE =1.848
KO=12, LO= 450, MO= 60
L
L
d
XBL 739-1219

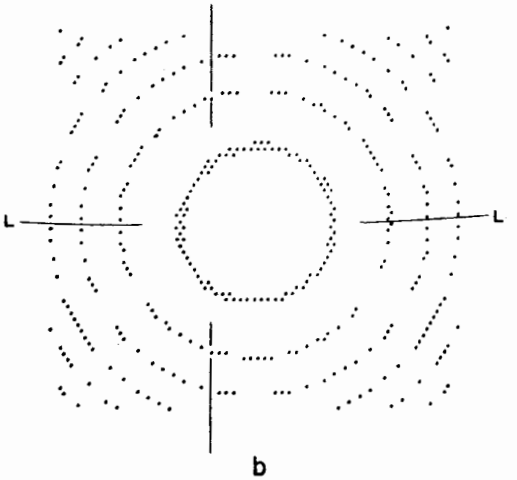
Fig. 33

INTERSTITIAL LOOP
11T PLANE IN 11T PROJECTION
TIP RADIUS =104.12 LATTICE CONSTANTS
P = .078
LOOP DIAMETER =11.00 ATOMS
DISTANCE FROM SURFACE =2.235
KO =12, LO = 448, HM = S9.S



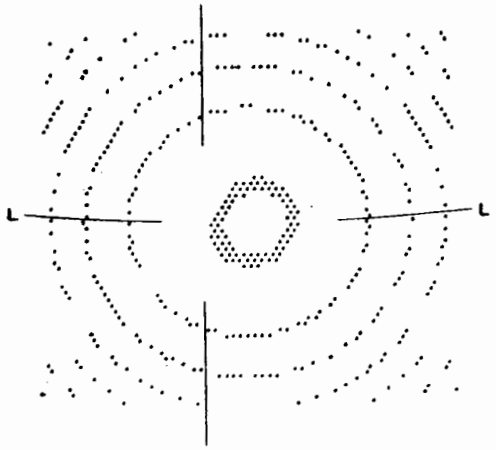
a

INTERSTITIAL LOOP
11T PLANE IN 11T PROJECTION
TIP RADIUS =103.70 LATTICE CONSTANTS
P = .078
LOOP DIAMETER =11.00 ATOMS
DISTANCE FROM SURFACE =2.088
KO =12, LO = 448, HM = S9.S



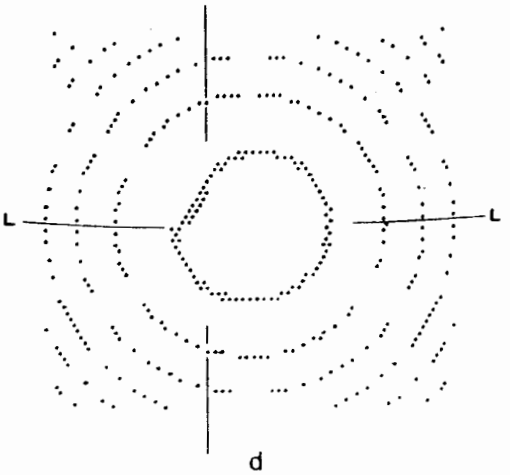
b

INTERSTITIAL LOOP
11T PLANE IN 11T PROJECTION
TIP RADIUS =103.49 LATTICE CONSTANTS
P = .078
LOOP DIAMETER =11.00 ATOMS
DISTANCE FROM SURFACE =2.015
KO =12, LO = 448, HM = S9.S



c

INTERSTITIAL LOOP WITH MIRROR IMAGE
11T PLANE IN 11T PROJECTION
TIP RADIUS=103.70 LATTICE CONSTANTS
P= .078
LOOP DIAMETER=11.00 ATOMS
DISTANCE FROM SURFACE=2.088
KO=12, LO= 448, HM= S9.S



d

XBL 739-1200

Fig. 34

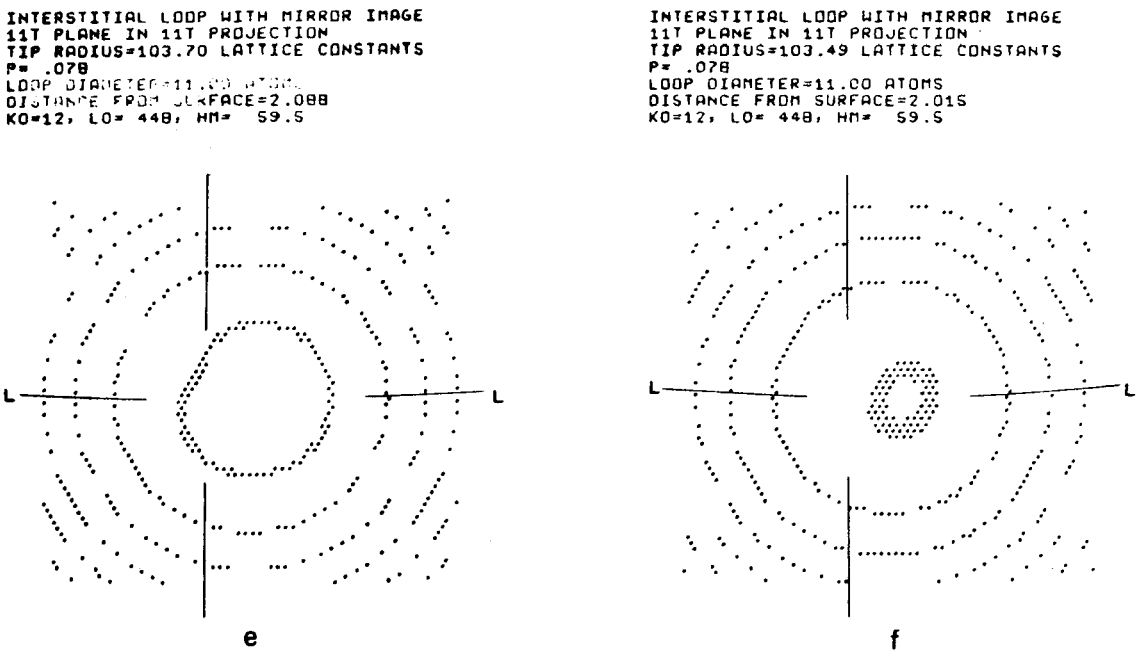
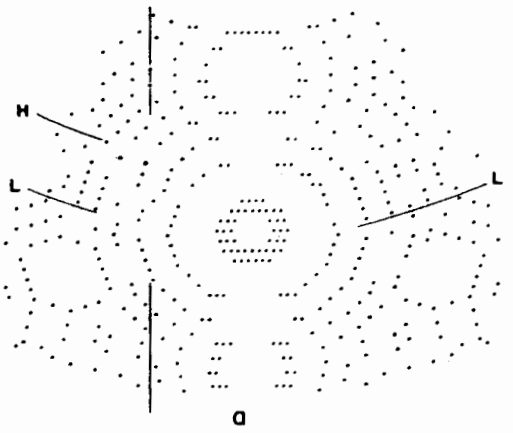

INTERSTITIAL LOOP WITH MIRROR IMAGE
11T PLANE IN 11T PROJECTION
TIP RADIUS=103.70 LATTICE CONSTANTS
P= .078
DISTANCE FROM SURFACE=2.088
KO=12, LO= 448, HM= 59.5
L
L
e
INTERSTITIAL LOOP WITH MIRROR IMAGE
11T PLANE IN 11T PROJECTION
TIP RADIUS=103.49 LATTICE CONSTANTS
P= .078
LOOP DIAMETER=11.00 ATOMS
DISTANCE FROM SURFACE=2.015
KO=12, LO= 448, HM= 59.5
L
L
f
XBL 739-1195

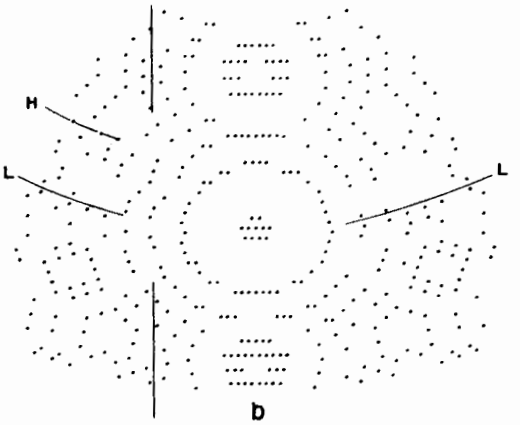
Fig. 34 (cont.)

INTERSTITIAL LOOP
113 PLANE IN 111 PROJECTION
TIP RADIUS = 99.87 LATTICE CONSTANTS
P = .078
LOOP DIAMETER = 9.00 ATOMS
DISTANCE FROM SURFACE =2.543
KO =28, LO = 206, MM = 149.5



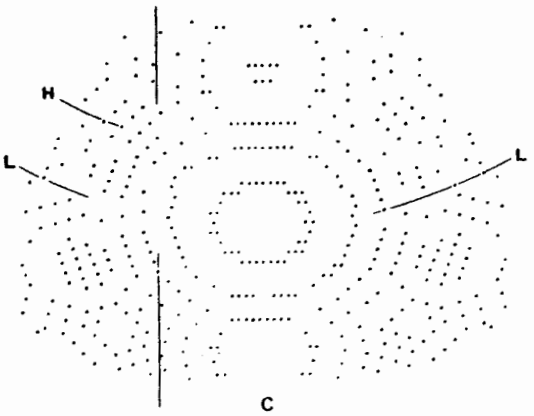
a

INTERSTITIAL LOOP
113 PLANE IN 111 PROJECTION
TIP RADIUS = 99.96 LATTICE CONSTANTS
P = .078
LOOP DIAMETER = 9.00 ATOMS
DISTANCE FROM SURFACE =2.493
KO =28, LO = 206, MM = 149.5



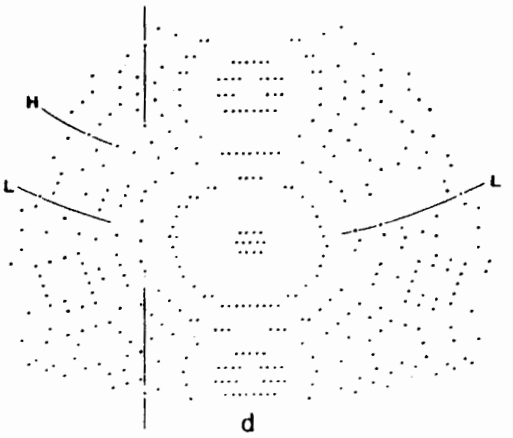
b

VACANCY LOOP
113 PLANE IN 111 PROJECTION
TIP RADIUS= 99.787 LATTICE CONSTANTS
P = .078
LOOP DIAMETER = 9.00 ATOMS
DISTANCE FROM SURFACE =2.392
KO =28, LO= 206, MO = 150



c

VACANCY LOOP
113 PLANE IN 111 PROJECTION
TIP RADIUS= 99.957 LATTICE CONSTANTS
P = .078
LOOP DIAMETER = 9.00 ATOMS
DISTANCE FROM SURFACE =2.291
KO =28, LO= 206, MO = 150



d

XBL 739-1220

Fig. 35

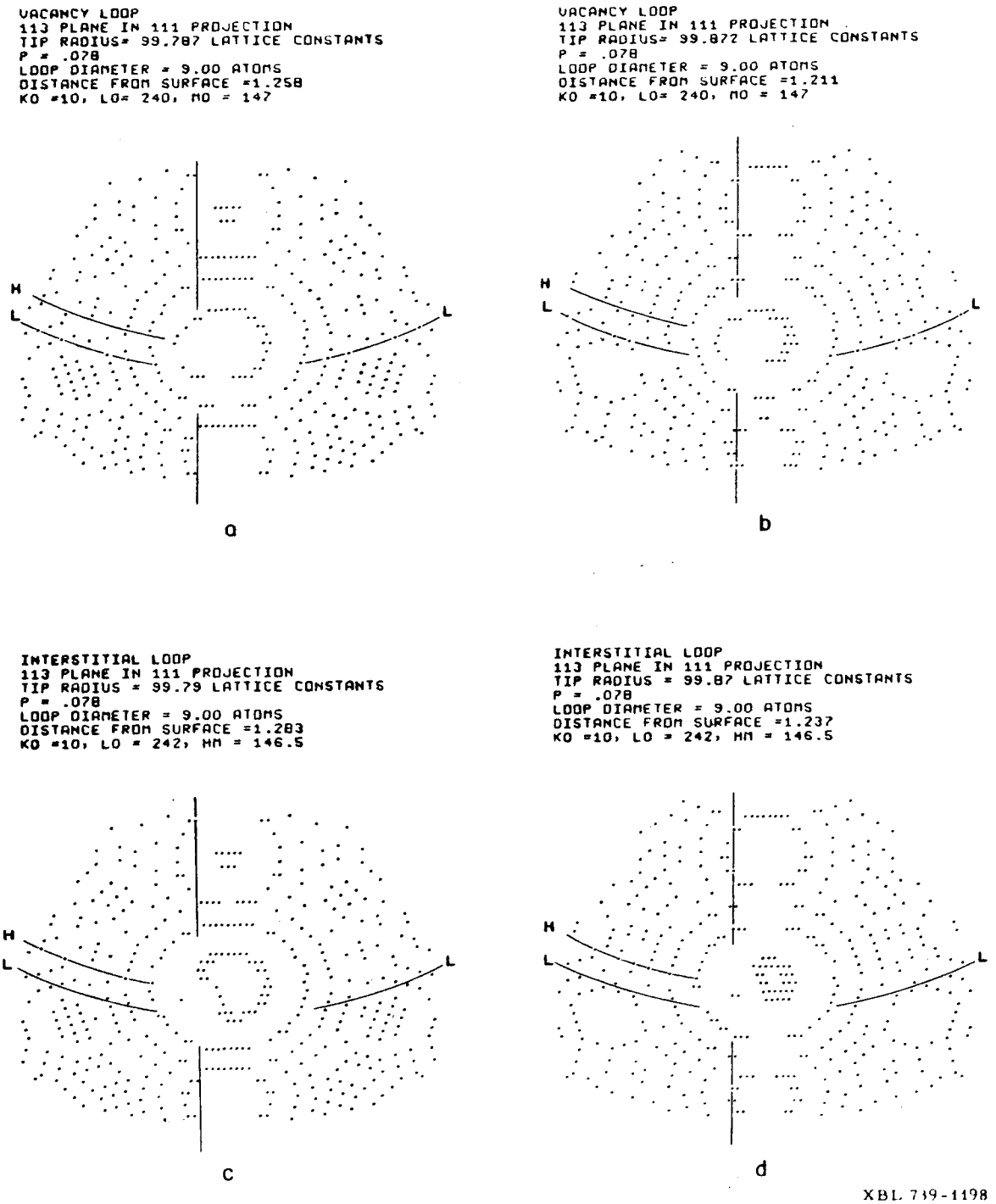

VACANCY LOOP
113 PLANE IN 111 PROJECTION
TIP RADIUS= 99.787 LATTICE CONSTANTS
P = .078
LOOP DIAMETER = 9.00 ATOMS
DISTANCE FROM SURFACE =1.258
KO =10, LO= 240, NO = 147
H
L
L
a
VACANCY LOOP
113 PLANE IN 111 PROJECTION
TIP RADIUS= 99.872 LATTICE CONSTANTS
P = .078
LOOP DIAMETER = 9.00 ATOMS
DISTANCE FROM SURFACE =1.211
KO =10, LO= 240, NO = 147
H
L
L
b
INTERSTITIAL LOOP
113 PLANE IN 111 PROJECTION
TIP RADIUS = 99.79 LATTICE CONSTANTS
P = .078
LOOP DIAMETER = 9.00 ATOMS
DISTANCE FROM SURFACE =1.283
KO =10, LO = 242, NN = 146.5
H
L
L
c
INTERSTITIAL LOOP
113 PLANE IN 111 PROJECTION
TIP RADIUS = 99.87 LATTICE CONSTANTS
P = .078
LOOP DIAMETER = 9.00 ATOMS
DISTANCE FROM SURFACE =1.237
KO =10, LO = 242, NN = 146.5
H
L
L
d
XBL 739-1198

Fig. 36

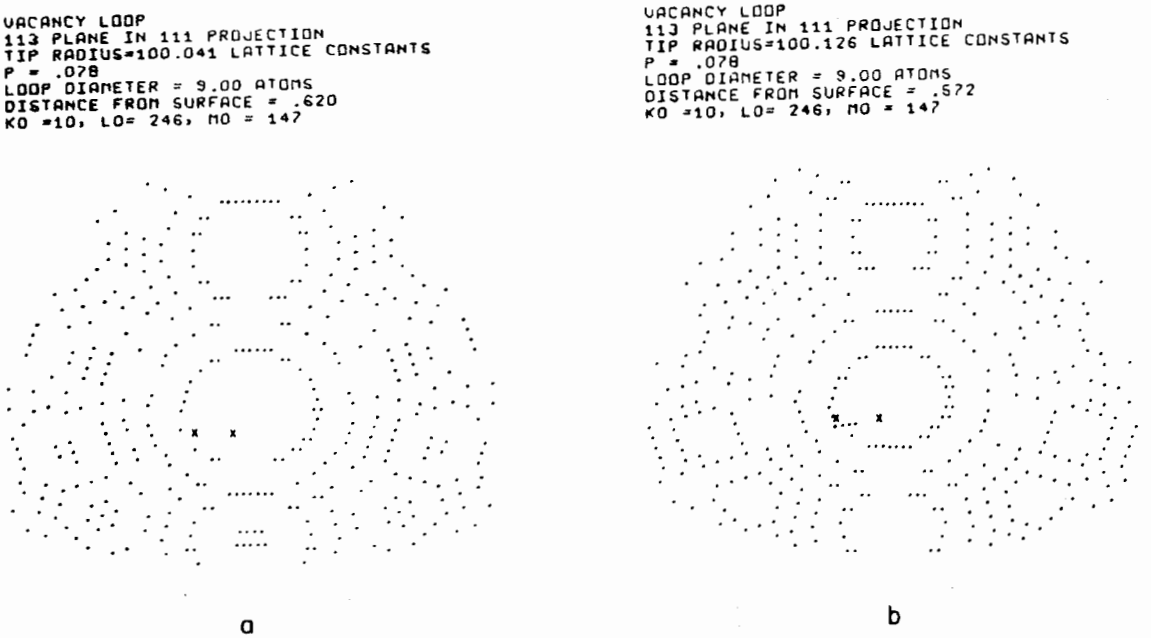

VACANCY LOOP
113 PLANE IN 111 PROJECTION
TIP RADIUS=100.041 LATTICE CONSTANTS
P = .078
LOOP DIAMETER = 9.00 ATOMS
DISTANCE FROM SURFACE = .620
KO =10, LO= 246, MO = 147
a
VACANCY LOOP
113 PLANE IN 111 PROJECTION
TIP RADIUS=100.126 LATTICE CONSTANTS
P = .078
LOOP DIAMETER = 9.00 ATOMS
DISTANCE FROM SURFACE = .572
KO =10, LO= 246, MO = 147
b
VACANCY LOOP
113 PLANE IN 111 PROJECTION
TIP RADIUS=100.211 LATTICE CONSTANTS
P = .078
LOOP DIAMETER = 9.00 ATOMS
DISTANCE FROM SURFACE = .525
KO =10, LO= 246, MO = 147
c
VACANCY LOOP
113 PLANE IN 111 PROJECTION
TIP RADIUS=100.296 LATTICE CONSTANTS
P = .078
LOOP DIAMETER = 9.00 ATOMS
DISTANCE FROM SURFACE = .477
KO =10, LO= 246, MO = 147
d
XBL 739-1205

Fig. 37

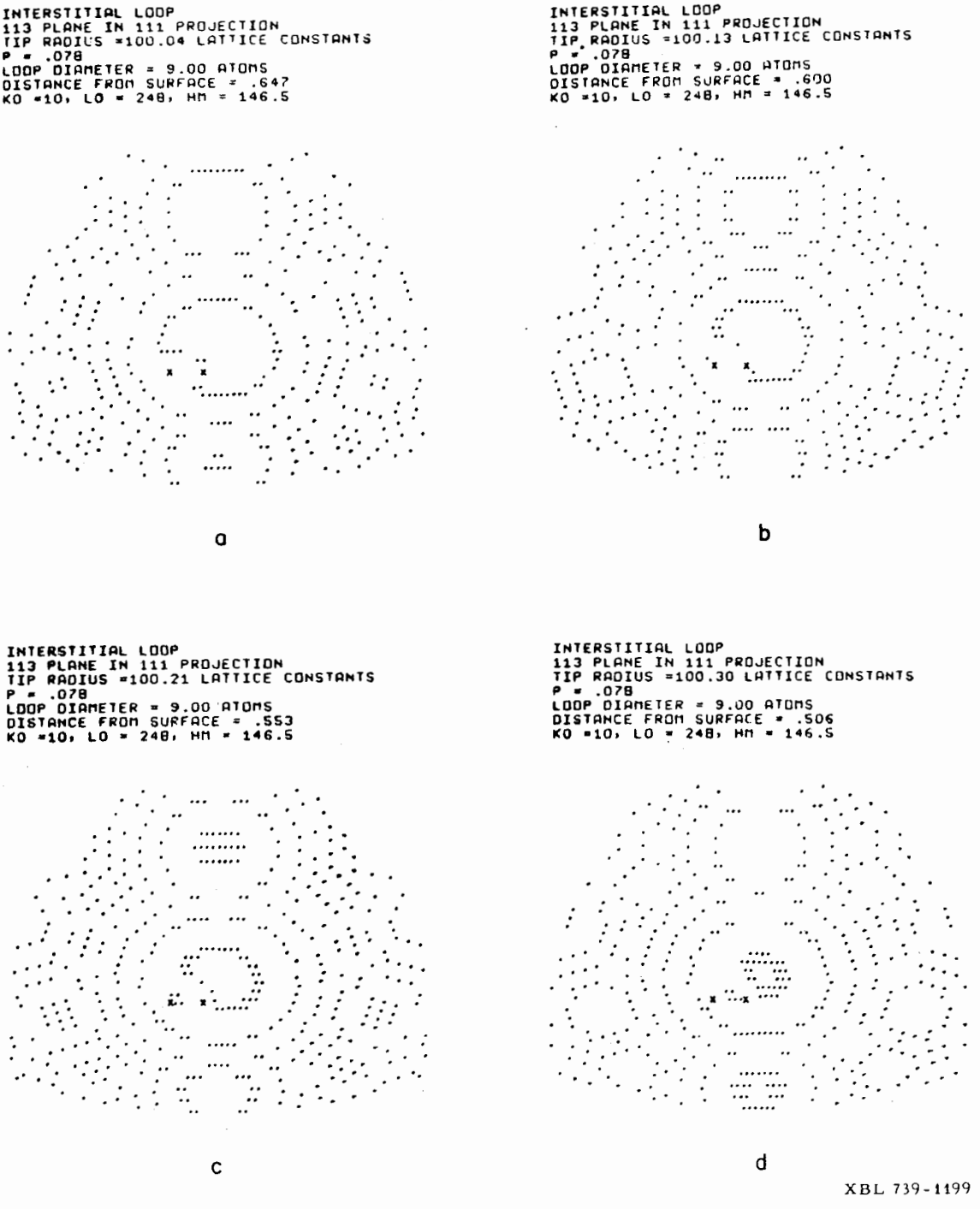

INTERSTITIAL LOOP
113 PLANE IN 111 PROJECTION
TIP RADIUS =100.04 LATTICE CONSTANTS
P = .078
LOOP DIAMETER = 9.00 ATOMS
DISTANCE FROM SURFACE = .647
KO =10, LO = 248, HM = 146.5
a
INTERSTITIAL LOOP
113 PLANE IN 111 PROJECTION
TIP RADIUS =100.13 LATTICE CONSTANTS
P = .078
LOOP DIAMETER = 9.00 ATOMS
DISTANCE FROM SURFACE = .600
KO =10, LO = 248, HM = 146.5
b
INTERSTITIAL LOOP
113 PLANE IN 111 PROJECTION
TIP RADIUS =100.21 LATTICE CONSTANTS
P = .078
LOOP DIAMETER = 9.00 ATOMS
DISTANCE FROM SURFACE = .553
KO =10, LO = 248, HM = 146.5
c
INTERSTITIAL LOOP
113 PLANE IN 111 PROJECTION
TIP RADIUS =100.30 LATTICE CONSTANTS
P = .078
LOOP DIAMETER = 9.00 ATOMS
DISTANCE FROM SURFACE = .506
KO =10, LO = 248, HM = 146.5
d
XBL 739-1199

Fig. 38

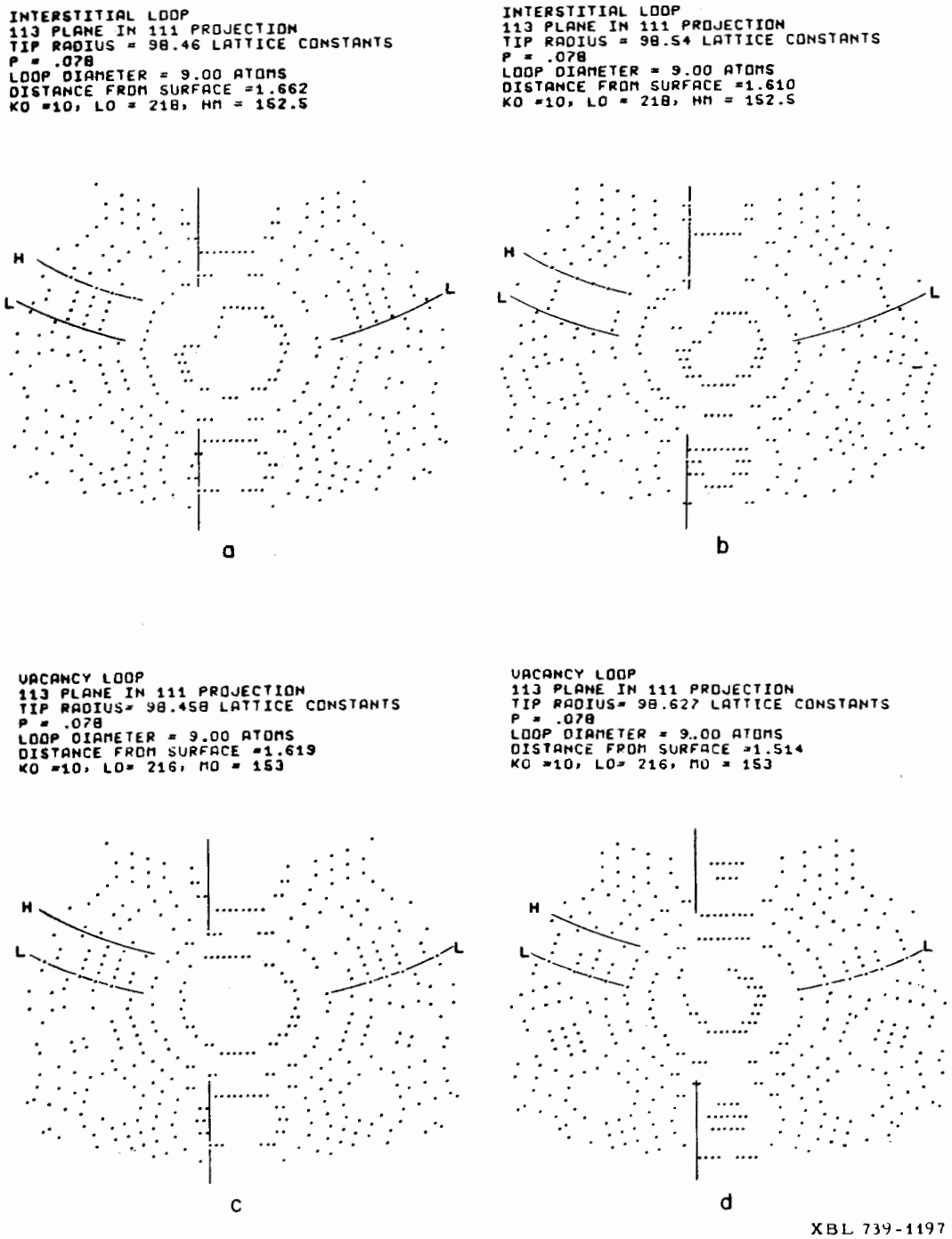

INTERSTITIAL LOOP
113 PLANE IN 111 PROJECTION
TIP RADIUS = 98.46 LATTICE CONSTANTS
P = .078
LOOP DIAMETER = 9.00 ATOMS
DISTANCE FROM SURFACE =1.662
KO =10, LO = 218, MM = 152.5
INTERSTITIAL LOOP
113 PLANE IN 111 PROJECTION
TIP RADIUS = 98.54 LATTICE CONSTANTS
P = .078
LOOP DIAMETER = 9.00 ATOMS
DISTANCE FROM SURFACE =1.610
KO =10, LO = 218, MM = 152.5
H
L
L
a
H
L
L
b
VACANCY LOOP
113 PLANE IN 111 PROJECTION
TIP RADIUS= 98.458 LATTICE CONSTANTS
P = .078
LOOP DIAMETER = 9.00 ATOMS
DISTANCE FROM SURFACE =1.619
KO =10, LO= 216, MO = 153
VACANCY LOOP
113 PLANE IN 111 PROJECTION
TIP RADIUS= 98.627 LATTICE CONSTANTS
P = .078
LOOP DIAMETER = 9.00 ATOMS
DISTANCE FROM SURFACE =1.514
KO =10, LO= 216, MO = 153
H
L
L
c
H
L
L
d
XBL 739-1197

Fig. 39

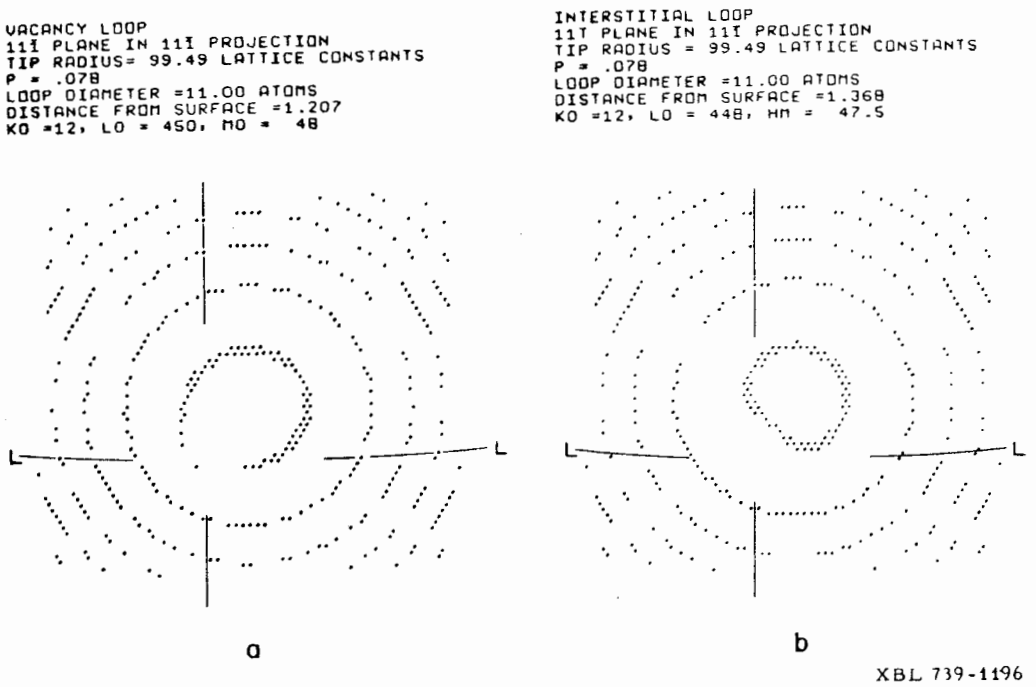

VACANCY LOOP
11Ī PLANE IN 11Ī PROJECTION
TIP RADIUS= 99.49 LATTICE CONSTANTS
P = .078
LOOP DIAMETER =11.00 ATOMS
DISTANCE FROM SURFACE =1.207
KO =12, LO = 450, MO = 48
INTERSTITIAL LOOP
11T PLANE IN 11Ī PROJECTION
TIP RADIUS = 99.49 LATTICE CONSTANTS
P = .078
LOOP DIAMETER =11.00 ATOMS
DISTANCE FROM SURFACE =1.368
KO =12, LO = 448, MM = 47.5
a
b
XBL 739-1196

Fig. 43

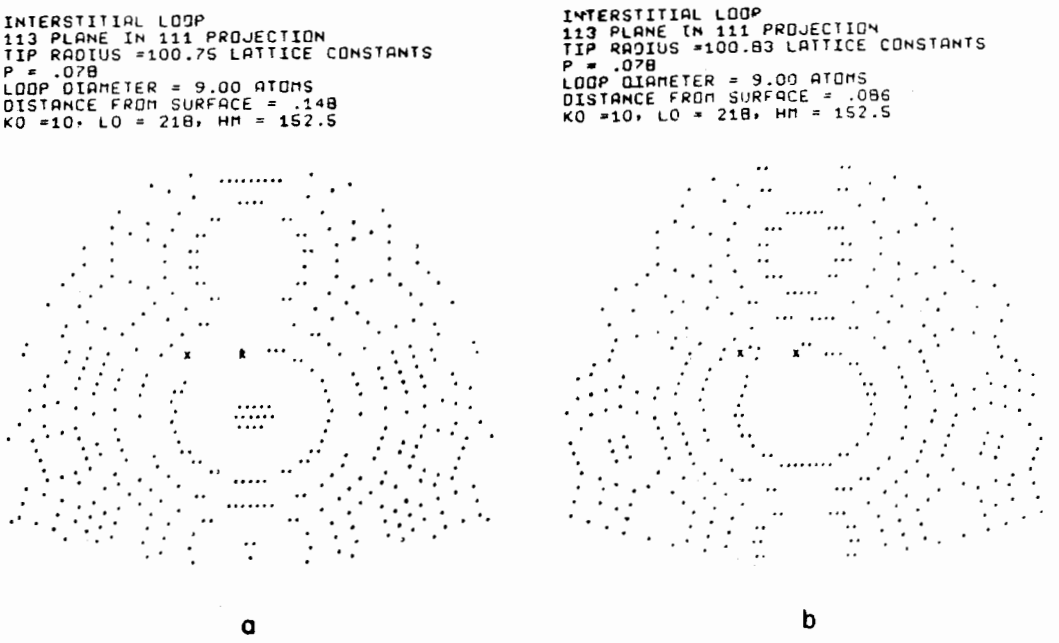

INTERSTITIAL LOOP
113 PLANE IN 111 PROJECTION
TIP RADIUS =100.75 LATTICE CONSTANTS
P = .078
LOOP DIAMETER = 9.00 ATOMS
DISTANCE FROM SURFACE = .148
KO =10, LO = 218, HM = 152.5
a
INTERSTITIAL LOOP
113 PLANE IN 111 PROJECTION
TIP RADIUS =100.83 LATTICE CONSTANTS
P = .078
LOOP DIAMETER = 9.00 ATOMS
DISTANCE FROM SURFACE = .086
KO =10, LO = 218, HM = 152.5
b
VACANCY LOOP
113 PLANE IN 111 PROJECTION
TIP RADIUS=100.749 LATTICE CONSTANTS
P = .078
LOOP DIAMETER = 9.00 ATOMS
DISTANCE FROM SURFACE = .076
KO =10, LO= 216, MO = 153
c
VACANCY LOOP
113 PLANE IN 111 PROJECTION
TIP RADIUS=100.833 LATTICE CONSTANTS
P = .078
LOOP DIAMETER = 9.00 ATOMS
DISTANCE FROM SURFACE = .014
KO =10, LO= 216, MO = 153
d
XBL 739-1209

Fig. 44

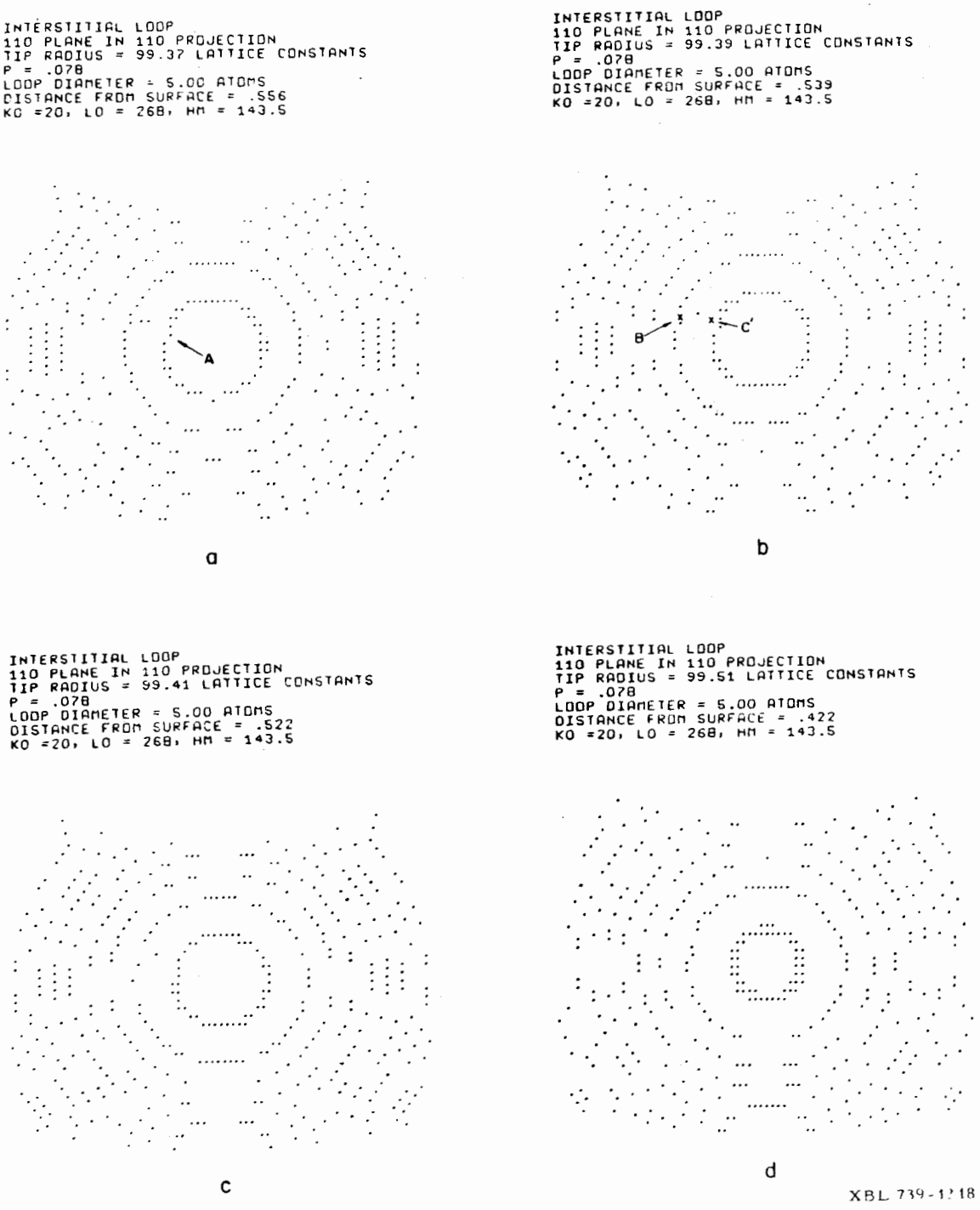

INTERSTITIAL LOOP
110 PLANE IN 110 PROJECTION
TIP RADIUS = 99.37 LATTICE CONSTANTS
P = .078
LOOP DIAMETER = 5.00 ATOMS
DISTANCE FROM SURFACE = .556
KO =20, LO = 268, HM = 143.5
A
a
INTERSTITIAL LOOP
110 PLANE IN 110 PROJECTION
TIP RADIUS = 99.39 LATTICE CONSTANTS
P = .078
LOOP DIAMETER = 5.00 ATOMS
DISTANCE FROM SURFACE = .539
KO =20, LO = 268, HM = 143.5
B
C'
b
INTERSTITIAL LOOP
110 PLANE IN 110 PROJECTION
TIP RADIUS = 99.41 LATTICE CONSTANTS
P = .078
LOOP DIAMETER = 5.00 ATOMS
DISTANCE FROM SURFACE = .522
KO =20, LO = 268, HM = 143.5
c
INTERSTITIAL LOOP
110 PLANE IN 110 PROJECTION
TIP RADIUS = 99.51 LATTICE CONSTANTS
P = .078
LOOP DIAMETER = 5.00 ATOMS
DISTANCE FROM SURFACE = .422
KO =20, LO = 268, HM = 143.5
d
XBL 739-1218

Fig. 46

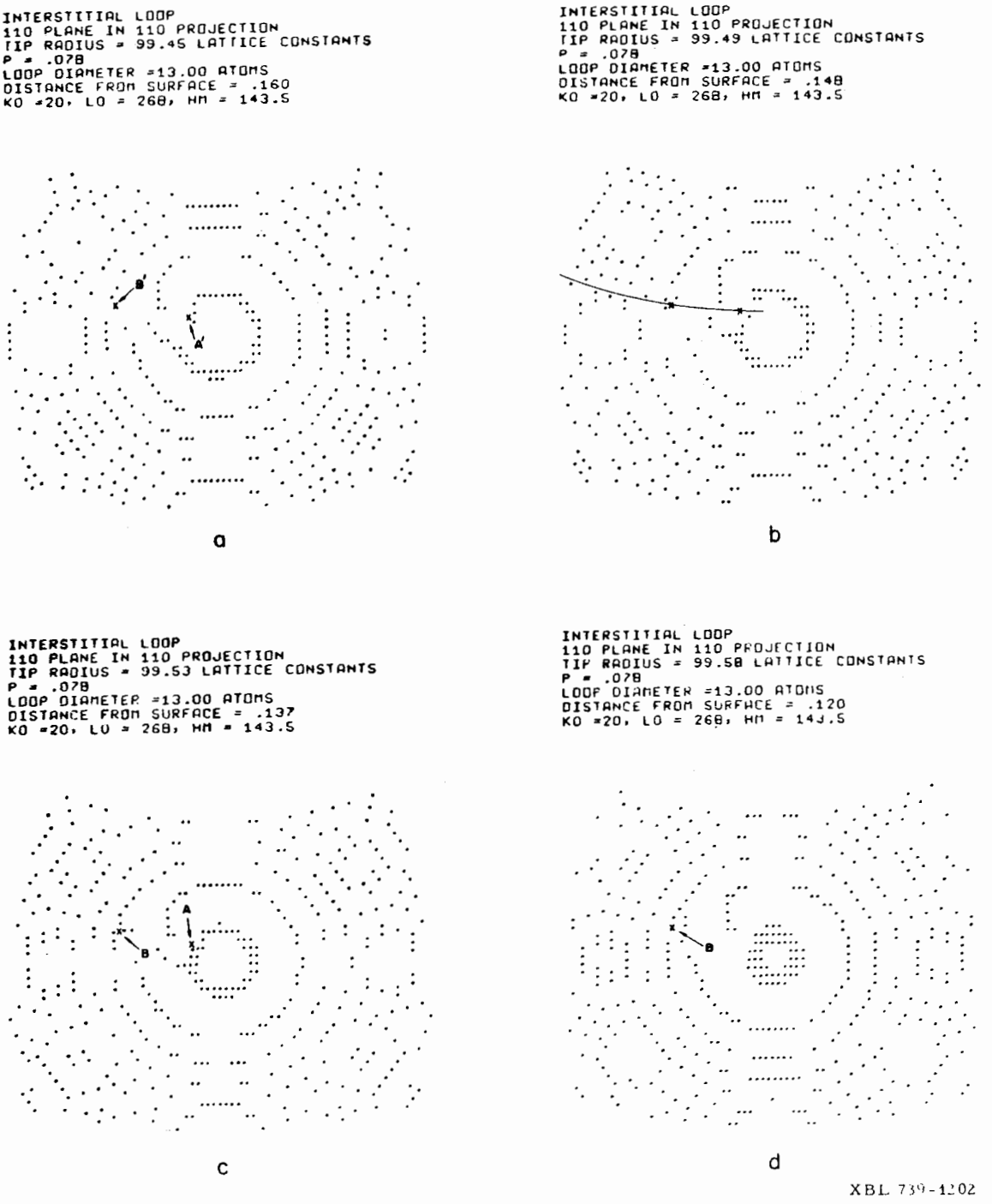

INTERSTITIAL LOOP
110 PLANE IN 110 PROJECTION
TIP RADIUS = 99.45 LATTICE CONSTANTS
P = .078
LOOP DIAMETER =13.00 ATOMS
DISTANCE FROM SURFACE = .160
KO =20, LO = 268, HM = 143.5
B
A
a
INTERSTITIAL LOOP
110 PLANE IN 110 PROJECTION
TIP RADIUS = 99.49 LATTICE CONSTANTS
P = .078
LOOP DIAMETER =13.00 ATOMS
DISTANCE FROM SURFACE = .148
KO =20, LO = 268, HM = 143.5
b
INTERSTITIAL LOOP
110 PLANE IN 110 PROJECTION
TIP RADIUS = 99.53 LATTICE CONSTANTS
P = .078
LOOP DIAMETER =13.00 ATOMS
DISTANCE FROM SURFACE = .137
KO =20, LO = 268, HM = 143.5
A
B
c
INTERSTITIAL LOOP
110 PLANE IN 110 PROJECTION
TIP RADIUS = 99.58 LATTICE CONSTANTS
P = .078
LOOP DIAMETER =13.00 ATOMS
DISTANCE FROM SURFACE = .120
KO =20, LO = 268, HM = 143.5
B
d
XBL 739-1202

Fig. 45

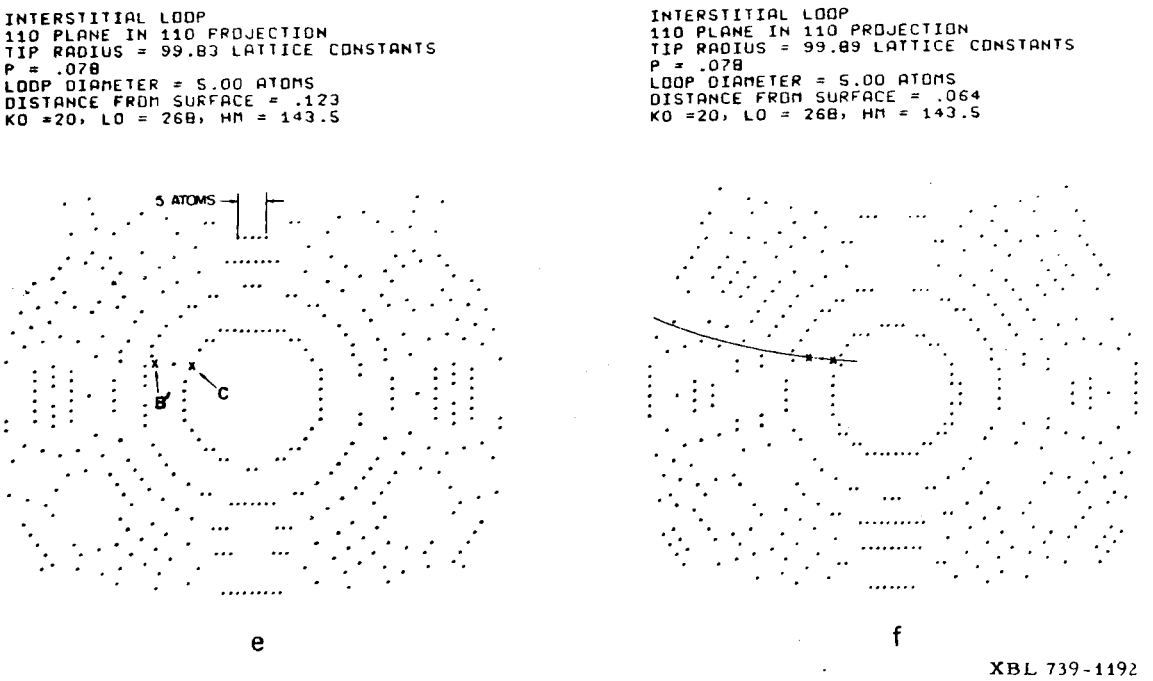

INTERSTITIAL LOOP
110 PLANE IN 110 PROJECTION
TIP RADIUS = 99.83 LATTICE CONSTANTS
P = .078
LOOP DIAMETER = 5.00 ATOMS
DISTANCE FROM SURFACE = .123
KO =20, LO = 268, HM = 143.5
5 ATOMS
B
C
e
INTERSTITIAL LOOP
110 PLANE IN 110 PROJECTION
TIP RADIUS = 99.89 LATTICE CONSTANTS
P = .078
LOOP DIAMETER = 5.00 ATOMS
DISTANCE FROM SURFACE = .064
KO =20, LO = 268, HM = 143.5
f
XBL 739-1192

Fig. 46 (cont.)

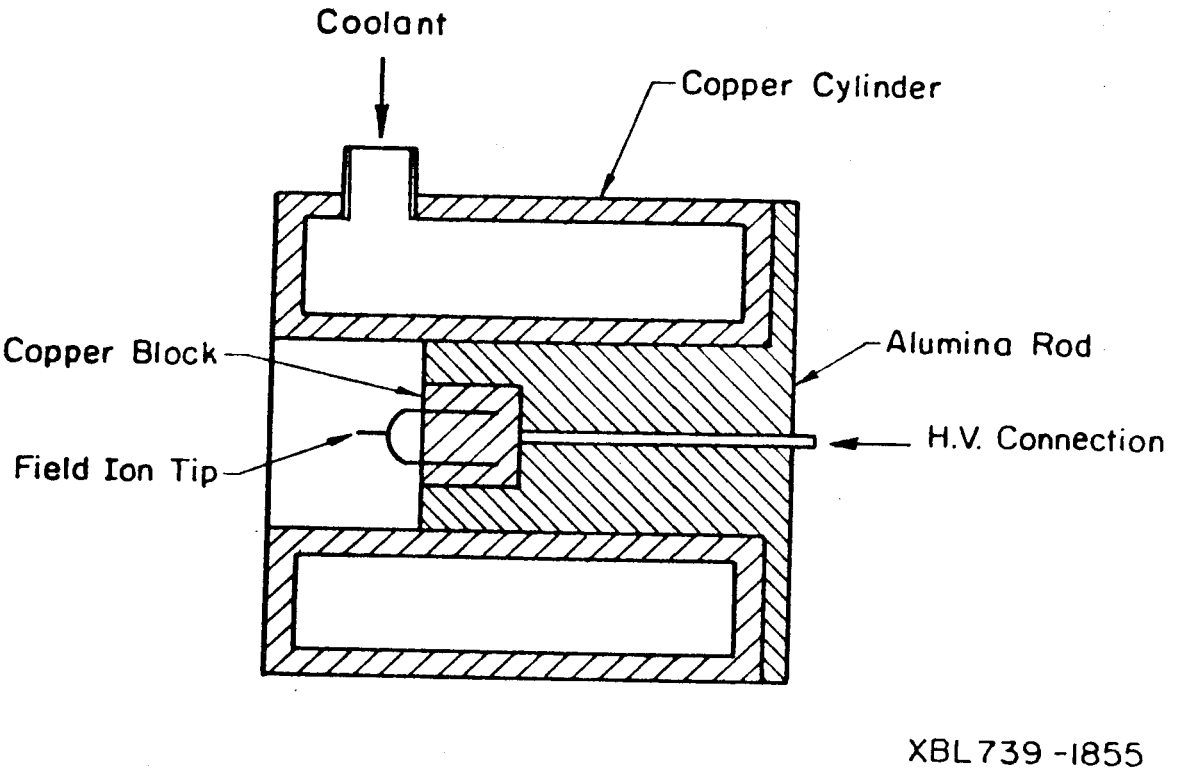
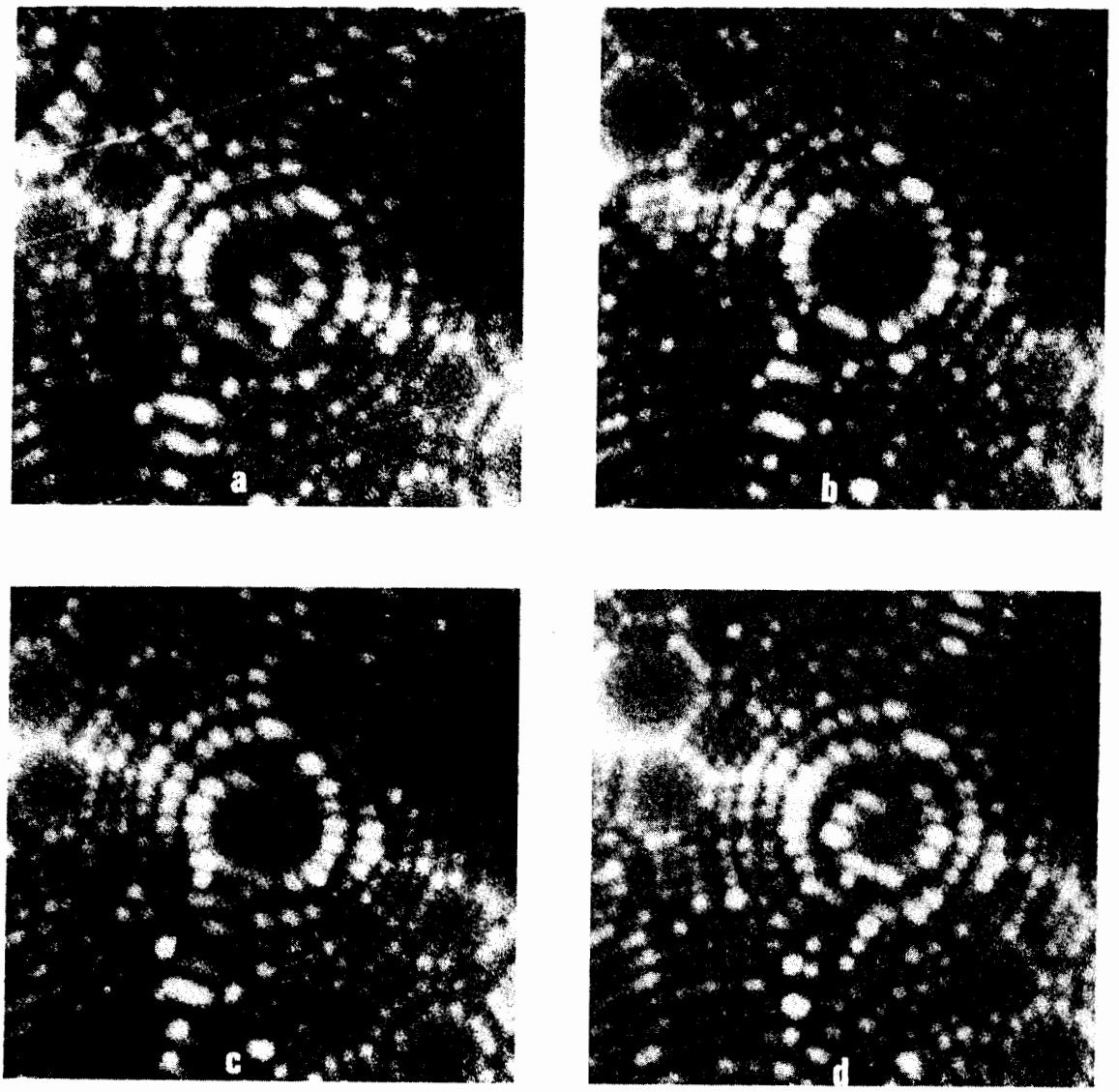
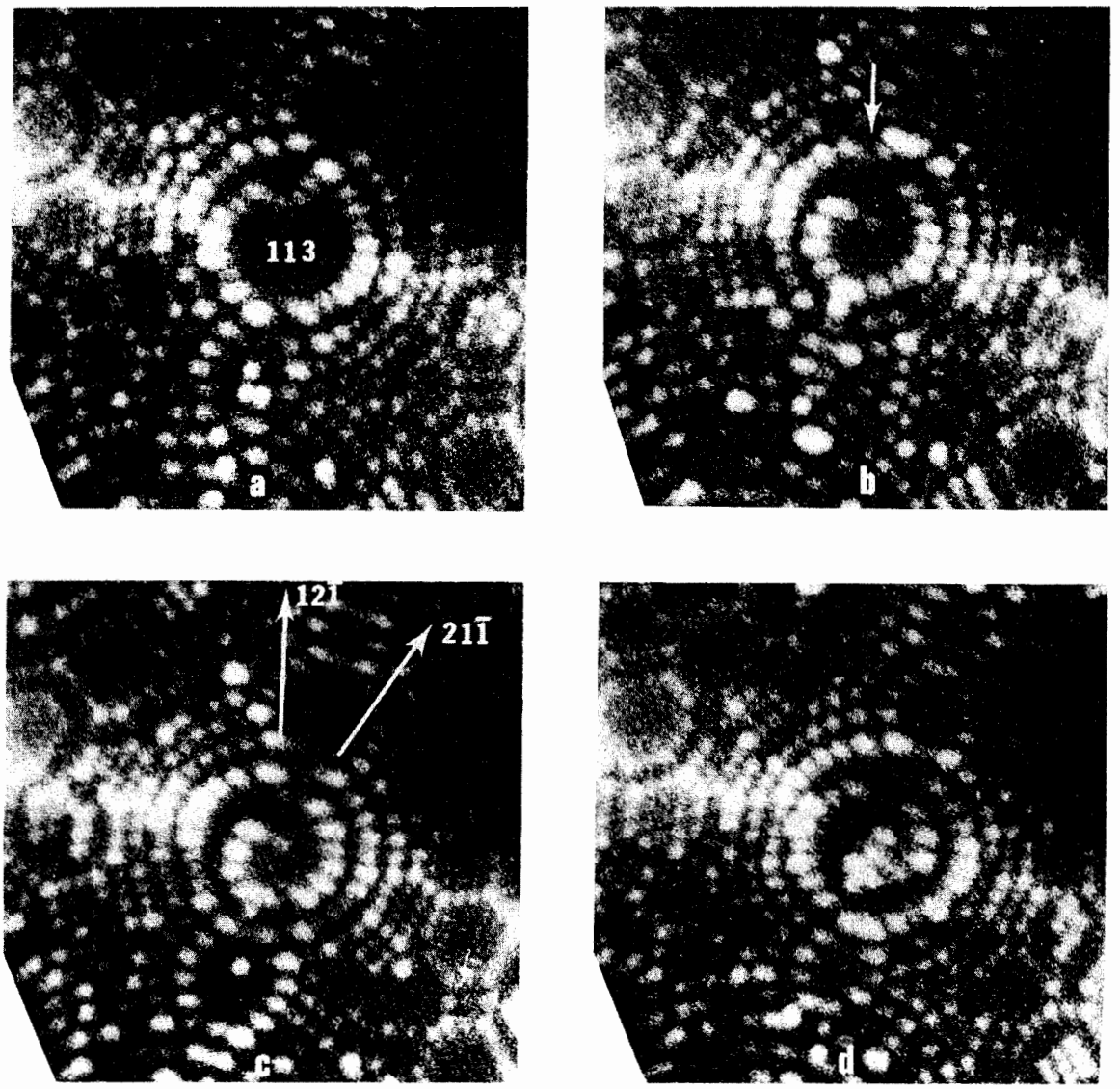

Coolant
Copper Cylinder
Copper Block
Alumina Rod
H.V. Connection
Field Ion Tip
XBL739-1855

Fig. 47



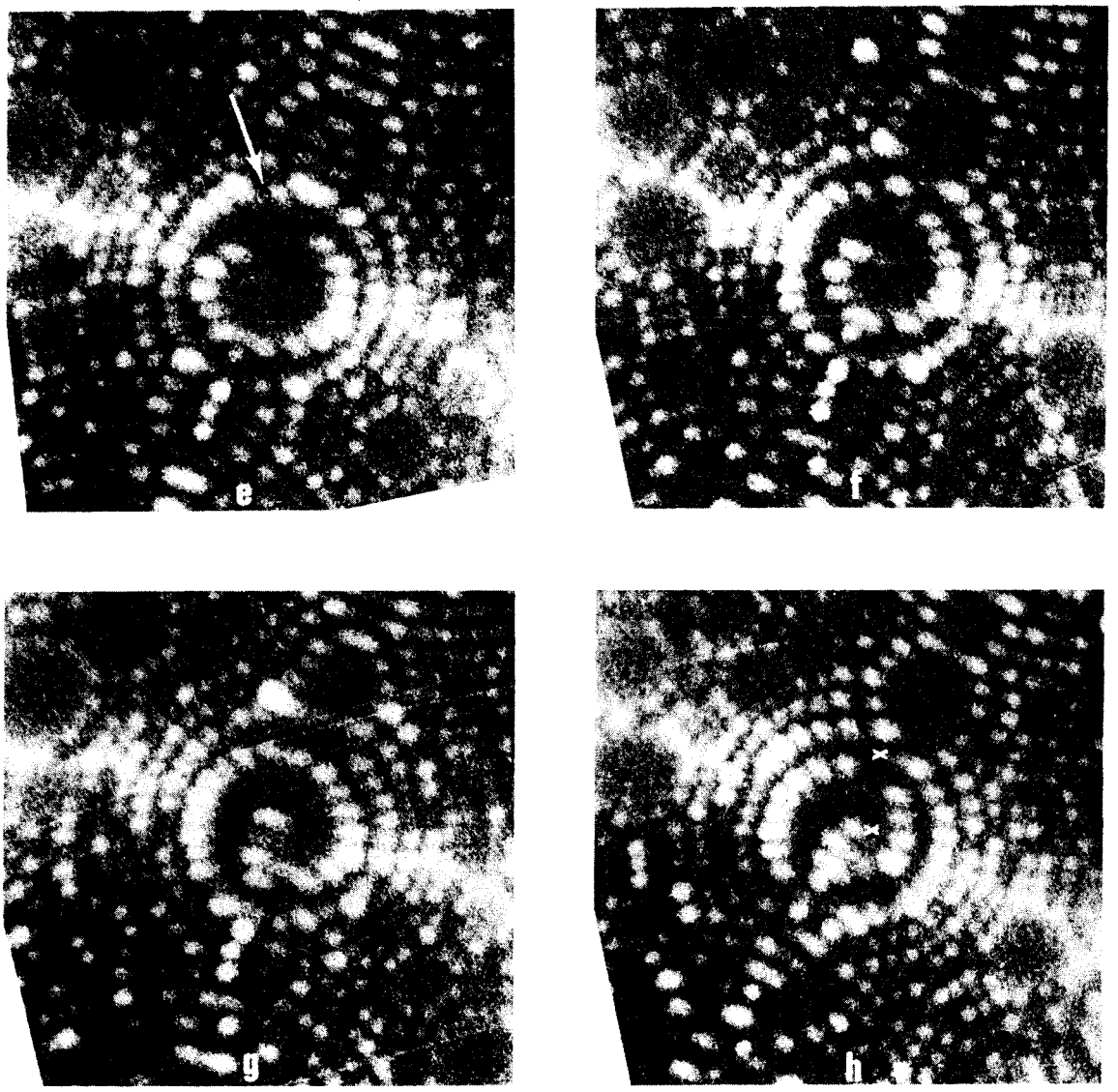
XBB 739-5492

Fig. 48



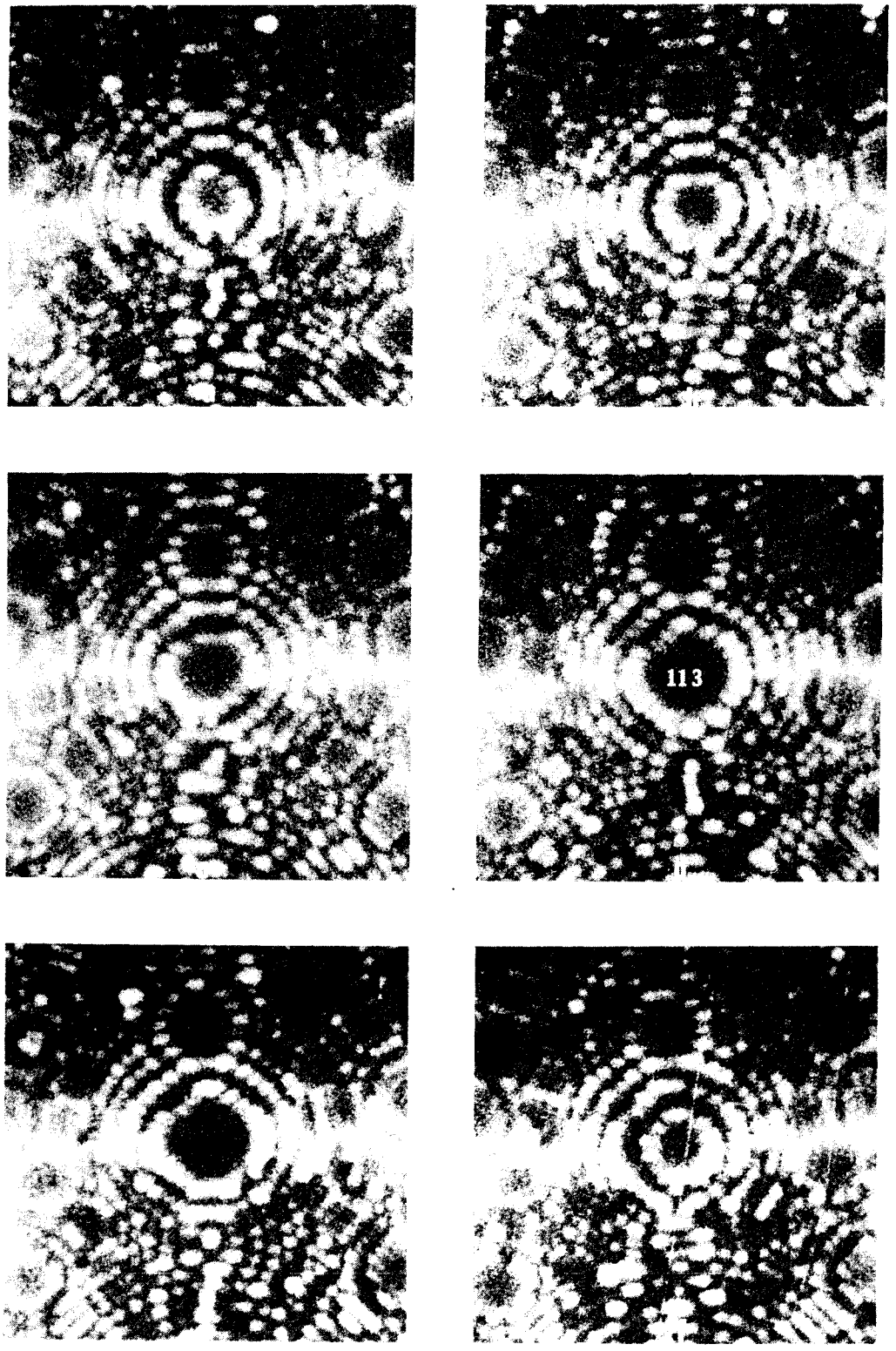
XBB 739-5490

Fig. 49



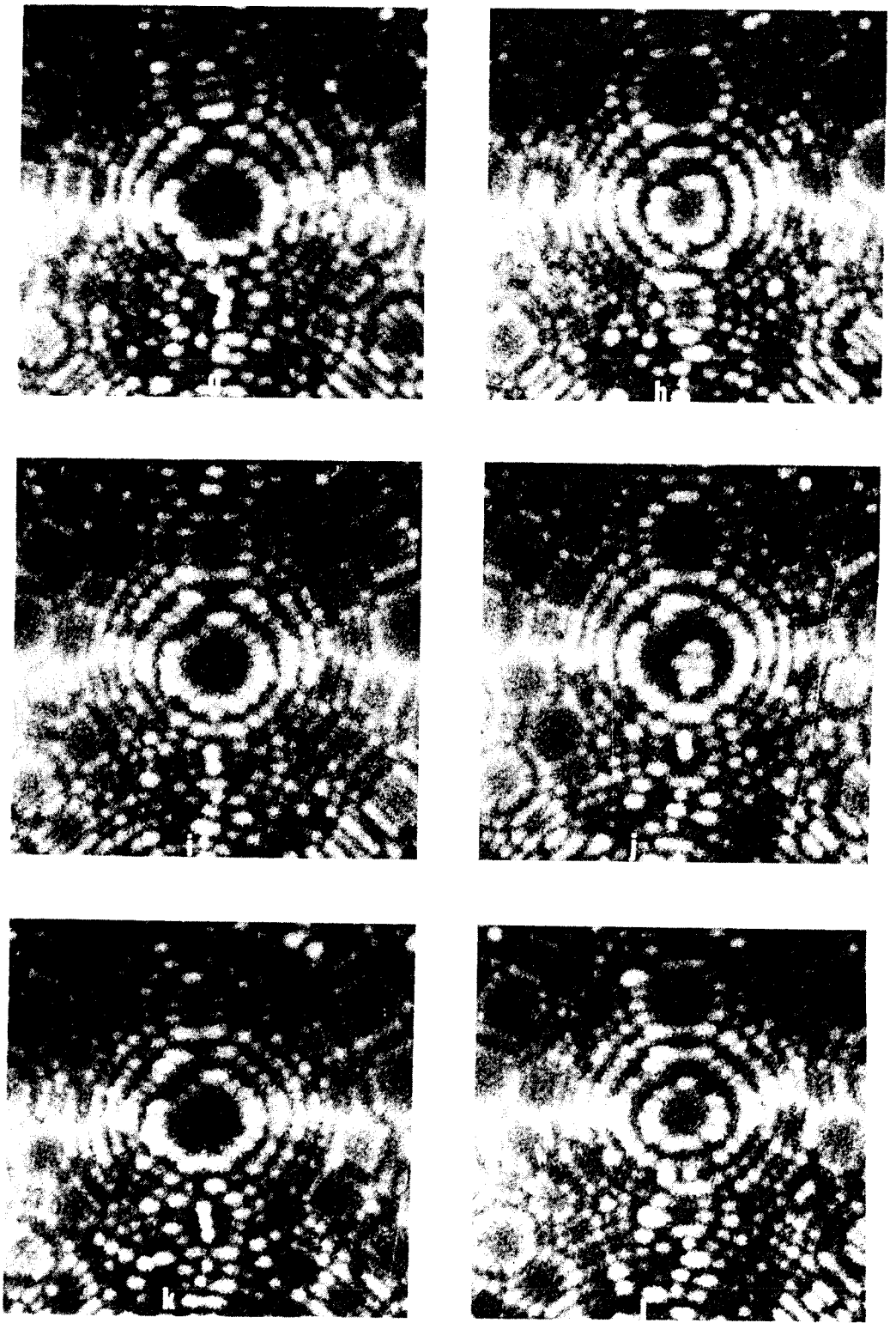
XBB 739-5491

Fig. 49 (cont.)



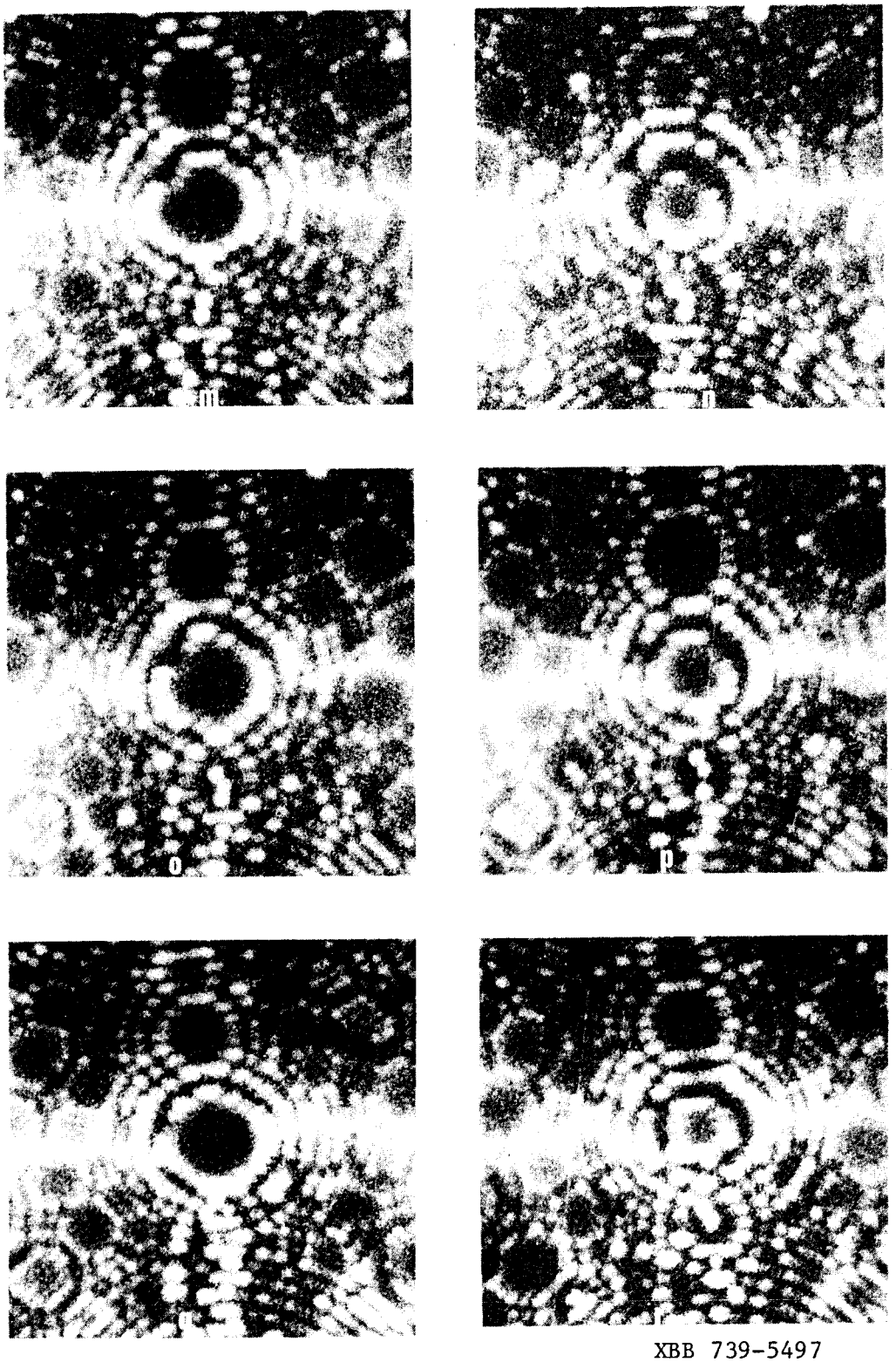
XBB 739-5494

Fig. 50



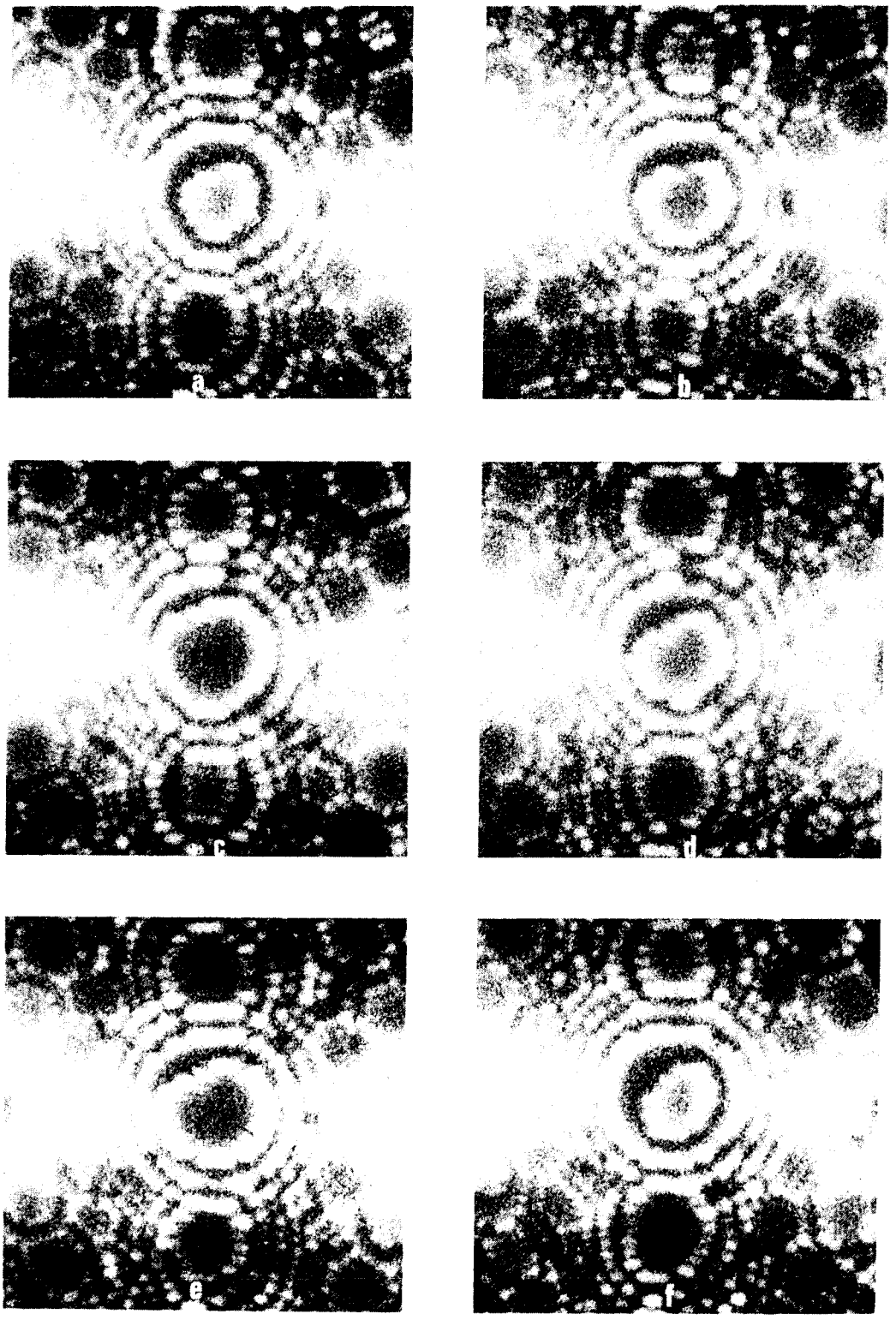
XBB 739-5496

Fig. 50 (cont.)



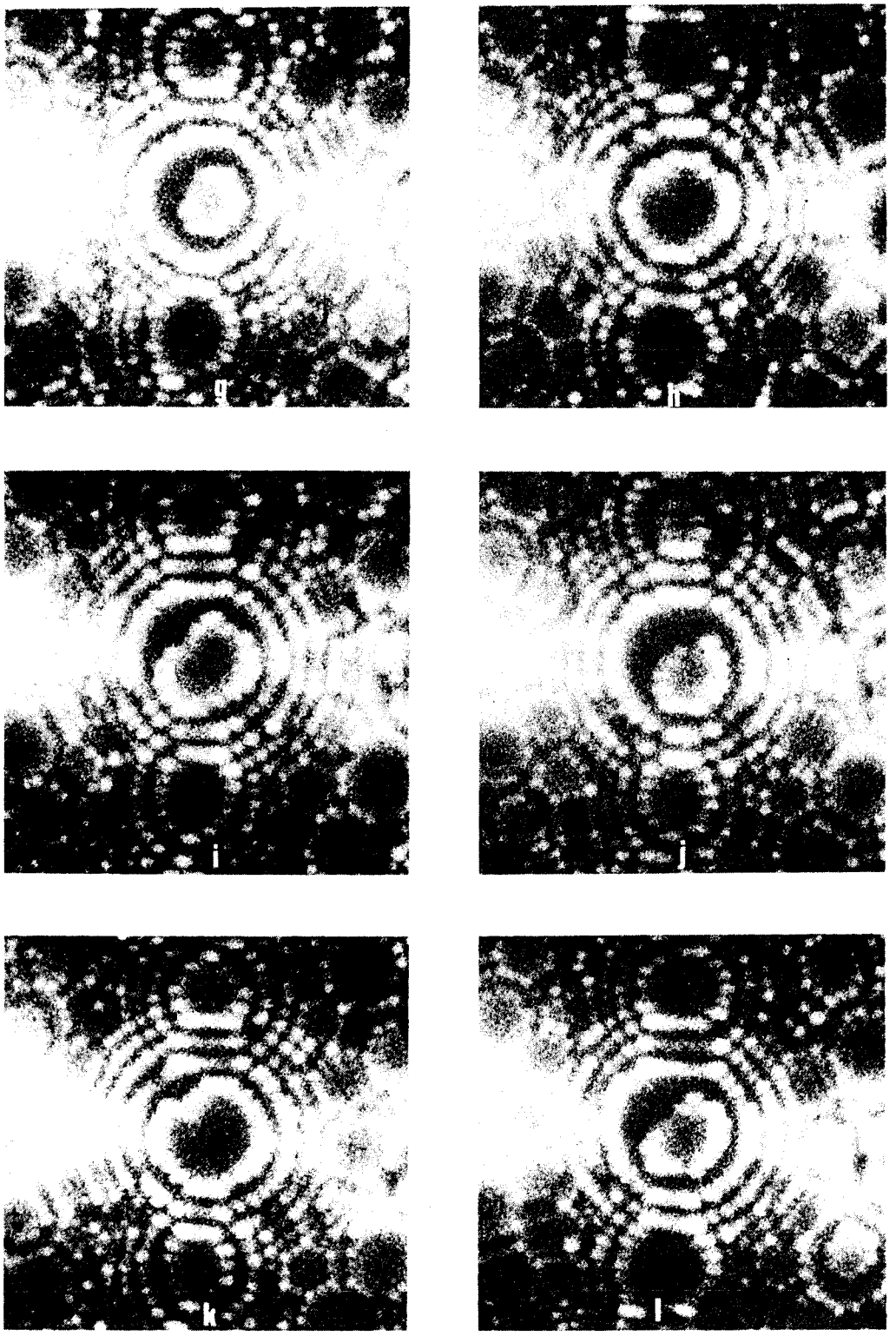
XBB 739-5497

Fig. 50 (cont.)



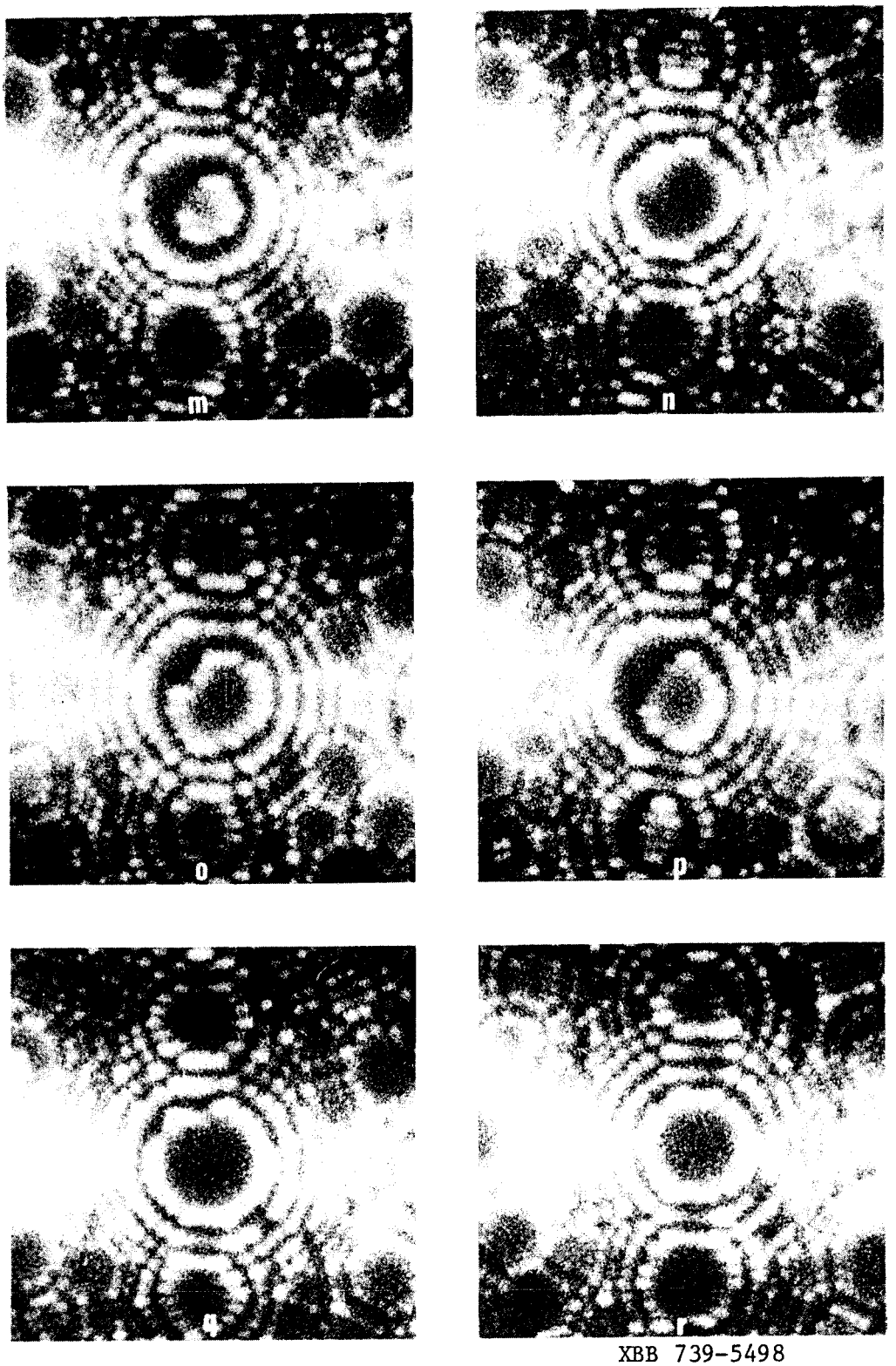
XBB 739-5495

Fig. 51



XBB 739-5493

Fig. 51 (cont.)



XBB 739-5498

Fig. 51 (cont.)